UNIVERSITÉ DE NICE-SOPHIA ANTIPOLIS - UFR SCIENCES
Ecole Doctorale "Sciences fondamentales et appliquées"

e

UNIVERSITÀ DEGLI STUDI DI GENOVA - FACOLTÀ DI SCIENZE M.F.N.
Dipartimento di Fisica

TESI

Presentata per ottenere il titolo di

Dottore di ricerca in FISICA
Settore scientifico-disciplinare FIS 02

da

Agnese Seminara

TRANSPORT AND DIFFUSION IN COMPLEX FLOWS

Discussa il 25 giugno 2007 di fronte alla commissione composta da:

A. Celani	*Direttore*
A. Mazzino	*Co-direttore*
R. Benzi	*Lettore esterno*
G. Falkovich	*Lettore esterno*
D. Bernard	*Commissario*
H. Kellay	*Commissario*
G. Ridolfi	*Commissario*
N. Zanghí	*Commissario*

Institut non linéaire de Nice

UNIVERSITÉ DE NICE-SOPHIA ANTIPOLIS - UFR SCIENCES
Ecole Doctorale "Sciences fondamentales et appliquées"

e

UNIVERSITÀ DEGLI STUDI DI GENOVA - FACOLTÀ DI SCIENZE M.F.N.
Dipartimento di Fisica

TESI

Presentata per ottenere il titolo di

Dottore di ricerca in FISICA
Settore scientifico-disciplinare FIS 02

da

Agnese Seminara

TRANSPORT AND DIFFUSION IN COMPLEX FLOWS

Discussa il 25 giugno 2007 di fronte alla commissione composta da:

A. Celani	*Direttore*
A. Mazzino	*Co-direttore*
R. Benzi	*Lettore esterno*
G. Falkovich	*Lettore esterno*
D. Bernard	*Commissario*
H. Kellay	*Commissario*
G. Ridolfi	*Commissario*
N. Zanghí	*Commissario*

Institut non linéaire de Nice

Abstract

Résumé

Cette thèse porte sur les propriétés statistiques de systèmes hors équilibre. La première partie est dédiée à l'étude de la diffusion vers une côte rocheuse. L'invariance d'échelle, déjà observée pour ce type de côte, est généralisée à l'invariance conforme. Cela permet d'étudier le problème de diffusion en utilisant des résultats de l'analyse harmonique pour le potentiel près d'une ligne invariante conforme. On montre l'intermittence spatiale du flux de polluant qui diffuse vers la ligne de côte.
La deuxième partie porte sur le scalaire passif qui décrit les problèmes de transport réèl comme la dispersion d'un colorant ou de la température en conditions appropriées. La structure de grande échelle du champ ne suit pas la prédiction d'équilibre thermique. Cela est lié à la présence de corrélations de long rayon, et d'une longue mémoire des conditions initiales due au transport turbulent.
La troisième partie est dédiée à la condensation de gouttes dans des écoulement humides turbulents. L'étude de ce problème est d'un grand intérêt pour la compréhension de la formation rapide de la pluie dans les nuages chauds. Il est également d'intérêt pour des problémes technologiques, comme l'optimisation de moteurs à injection directe. Le transport turbulent joue un rôle important de part le fait qu'il engendre de grandes fluctuations des conditions du milieu où les gouttes grandissent. Les théories de champ moyen ne peuvent pas décrire les effets dûs aux corrélations entre les gouttes et le champ de vapeur.

Sintesi

Questo lavoro di tesi tratta le proprietà statistiche di alcuni sistemi fuori dall'equilibrio. La prima parte è dedicata al problema della diffusione verso coste rocciose. L'invarianza di scala, precedentemente osservata per questo tipo di costa, viene generalizzata a invarianza conforme. Questo consente di studiare il problema della diffusione utilizzando risultati dell'analisi armonica per il potenziale in prossimità di una curva invariante conforme. Si mostra intermittenza spaziale del flusso di inquinante che diffonde verso la linea di costa.
La seconda parte è dedicata allo scalare passivo, che descrive problemi reali di trasporto come la dispersione di un colorante o la temperatura in condizioni opportune. La struttura di grande scala di un campo scalare trasportato da un flusso turbolento devia dall'equilibrio termico. La causa per questa aspettativa disattesa risiede in correlazioni a lungo raggio e fenomeni di memoria delle condizioni iniziali.

La terza parte tratta il problema della condensazione e evaporazione di microgocce in ambienti turbolenti umidi. Il tema è di interesse per la comprensione dell'efficace processo di formazione della pioggia nelle nuvole calde. È inoltre importante per la corretta progettazione dei motori a iniezione diretta. Il trasporto turbolento gioca un ruolo essenziale poiché fornisce un ambiente altamente variabile per la crescita delle gocce. A causa della presenza di correlazioni fra le gocce e il campo di vapore teorie di campo medio risultano inadeguate a cogliere aspetti rilevanti del problema.

Abstract

The broad subject of this thesis is the statistical physics of non-equilibrium systems. The first part is dedicated to the problem of diffusion over rocky shorelines. It turns out that the observed fractality of a consistent portion of the world coastline can be promoted to conformal invariance. This allows to investigate the problem of diffusion toward the coastline using results of harmonic analysis for the potential in the vicinity of a conformal invariant curve. The flux of a pollutant diffusing toward the shoreline is shown to display spatial intermittency.
The second part is dedicated to passive scalar transport, which describes real problems like the dispersion of dilute dyes or temperature under appropriate conditions. Thermal equilibrium expectations for the large-scale passive scalar structure are violated. The breakdown of Gibbs equilibrium is traced back to long-range correlations and long-lasting memories of the initial conditions, due to the underlying turbulent velocity field.
The third part is dedicated to the problem of condensation/evaporation of microdroplets in turbulent moist environment. This general issue is relevant for the understanding of rain-initiation efficiency in warm clouds and for technological issues like the optimization of spark-ignition engines. Turbulent transport is found to play a crucial role in that it provides strong fluctuations for droplet growth. Due to correlations between droplets and vapor field, mean-field type arguments are found to be inadequate to capture relevant aspects of the problem.

Publication list

Published or submitted papers related to the thesis

Part I

Part II

Part III

Contents

Introduction

The broad subject of this thesis is the statistical physics of non-equilibrium systems. I began my PhD work by focusing on the paradigmatic examples of systems strongly out of equilibrium: turbulence. Instances of turbulent flows are common experience of everyday life (e.g. coffee in a cup or smoke plumes coming out from a chimney) and span the most diverse systems from soap films to the structure of galaxies. A detailed description of a turbulent flow is hard to be envisioned, since it is non-reproducible and highly fluctuating both in space and time. Again, the only appropriate language seems to be the statistical one. In most cases, non-linear couplings dominate on viscous dissipation, so that a huge range of spatial scales are dynamically coupled and organize themselves in complex spatial structures. Turbulence can be sustained against dissipation only by an external energy pumping and is otherwise bound to decay. Unlike for equilibrium systems, the integrals of motion are insufficient to describe the statistics of a turbulent flow. Indeed, they cannot capture the distinctive features of turbulence emerging from the multi-point statistics. In general, the latter cannot be deduced from the two-point one, at least whenever the spatial structure of a turbulent flow is not self-similar. In the latter case, scale invariance is broken in that strong fluctuations become more probable as the scales become smaller.

The deep differences between turbulence and equilibrium are actually straightforward. However there is an aesthetically appealing analogy between the role of the conservation laws in the two phenomena. From a Lagrangian point of view, one can characterize the multi-point statistics of a turbulent field by focusing on the multi-particle evolution in the flow. It turns out that the symmetry breaking in turbulence origins from functions of the inter particle distance that are *statistically* preserved as the particles evolve in the flow. These functions have been rigorously demonstrated to be responsible for intermittency and anomalous scaling of scalar turbulence, as recognized almost simultaneously by different research groups [2, 5, 12] following a stochastic model proposed by R. H. Kraichnan [6]. In this context the statistical integrals of motion could be analytically obtained as zero-modes of closed partial differential operators.

The concepts of intermittency and the breakdown of scale invariance gathered from turbulence, versus thermal equilibrium and mean field approach are the leitmotifs of my work. The whole thesis focuses on phenomena out of equilibrium. The main concern is to find out whether equilibrium and non-equilibrium features come out consistently with the expectations. Thermal equilibrium is supposed to be restored for scalar turbulence at large scales. Intermittency is not an immediate property of scale-invariant systems. Particles interacting with fields advected by turbulent flows, might be expected to qualitatively match mean field type predictions. In this thesis I will show systems where these quite reasonable expectations turn out to be wrong. The large-scale structure of passive scalar turbulence

deviates from Gibbs equilibrium. The flux of a scalar concentration diffusing toward self-similar coasts displays spatial intermittency. Condensing droplets in a turbulent environment are segregated in moist regions. Their history is strongly determined by correlations between fields and particles.

I present the works in inverse chronological order, starting from the most recent ones. The thesis is divided in three parts that can be read as a progressive addition of ingredients. I start with diffusion of a scalar concentration toward rocky coasts in part I. In part II, with the inclusion of advection, I treat the large-scale structure of passive scalar turbulence. Then I add particles, interacting with the passive scalar field and present condensation in turbulent flows in Part III.

Part I: Diffusion toward rocky coastlines

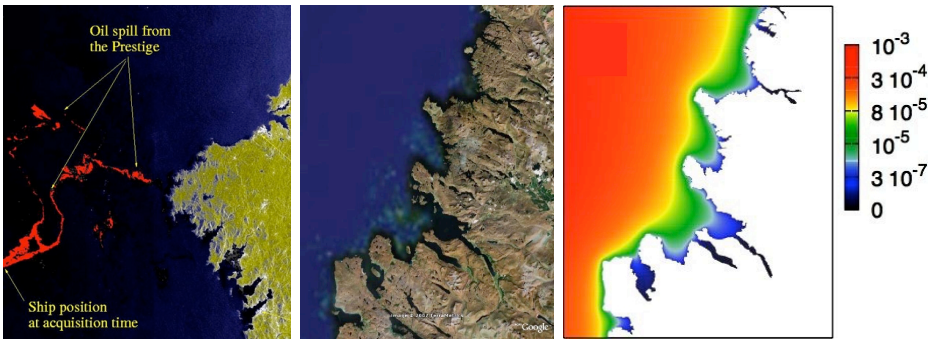

(a) (b) (c)

Figure 1: (a) Image from the sink of the Prestige tanker on 13th November 2002 off the Galician coast. The oil spill, estimated in roughly $64,000$ tons, polluted thousands of kilometers of the Spanish, Portuguese and French coasts. (b) Image of the west coast of Britain, the paradigmatic example of fractal shoreline. (c) Flux of pollutant over the shoreline shown in (b), resulting from the study of diffusion toward rockycoasts, presented in Part I. The spatially intermittent flux of pollutant is indicated by the different colors.

In the first part of the thesis I present a theoretical treatment of the problem of pollutant diffusion toward rocky shorelines. Diffusion is a key ingredient of pollutant dispersion whose paramount importance immediately emerges when listing data of oil spill from tanker sinks (see figure 1(a)).

Since the first conjectures of Richardson and the successive work of Mandelbrot [7], a consistent portion of the world shoreline has been observed to be fractal. This means that there is no statistical difference among subsequent magnified views of the coastline. Fractality is a very common property of physical curves. The cauliflower, the structure of fern and other leaves, the branches of a bolt of lightning are all examples of fractals. Mathematically a fractal is a scale-invariant object, i.e. an object whose properties do not change under contractions or dilatations.

In a recent work [11], a stochastic model for the erosion of rocky coasts by wave quarrying has been proposed. Starting from a flat line, the dynamics of erosion build step by step an increasingly complex coastline. The self-stabilization of the dynamics results in a fractal

stationary state. The simple model proposed for rocky coasts erosion strongly reminds of percolation, a well-known statistical model that applies to the flow of a fluid through a porous material, such as honey seeping through beeswax.
The observed fractal structure of rocky coasts, along with the percolation-like simple model mentioned above, call for conformal invariance, an interesting upgrade of scale invariance. A conformal invariant object does not change its properties under any angle-preserving (conformal) transformation. Conformal transformations have been widely used in cartography since Mercator's 16-th century map. While conformality turns out to be a strong constraint when the space dimension d is higher or equal to 3, something special happens for $d = 2$: the group of two-dimensional conformal transformations is infinite dimensional. Therefore a conformal invariant object in two dimensions enjoys a rich degree of symmetry. In turn, conformal field theories in two dimensions turn out to be extremely powerful in producing analytical results.

The work I performed in this framework is divided in two steps. The first one is the numerical proof that rocky shorelines are not only mere fractals but can be promoted to conformal invariant curves. To prove that I first analyzed the real world coastline by means of high resolution satellite data. I selected the portions of the coasts good candidates for conformal invariance that are the rocky coasts, characterized by fractal dimension $D = 4/3$ (like the one shown in figure 1(b)). I analyzed the statistics of these curves and proved that this is consistent with the results holding for conformal invariant curves [3]. To further sustain this idea I analyzed the artificial shorelines obtained by simulating the stochastic model mentioned above. The results confirm consistency with conformal invariance.
As a second step I could apply to rocky coasts the results of harmonic analysis for the potential in the vicinity of a conformal invariant line. Indeed, the electrostatic potential generated by a conductor with the shape of the rocky coast is formally equivalent to a scalar concentration (e.g. a pollutant) diffusing toward the coast. The results of this analysis show that in the vicinity of the rocky coast, the flux of pollutant is spatially intermittent, as shown in figure 1(c), a property already observed for real pollutant dispersion in [9]. Intermittency is here quite surprising, since it results from diffusion and self-similarity, two ingredients that would not call for intermittency at first sight.

Part II: large-scale structure of passive scalar transport

The second part of the thesis is devoted to the problem of the passive scalar at large scales. It is of general physical interest to study the large scale properties of a field generated at much smaller scales. For instance, the properties of the actual universe have originated during a fast event, concerning a tiny volume and have then propagated in time and space (see figure 2(a)). The large scale properties of the propagation of seismic signals have been traced back to the microscopic structure of crystals in mantle rocks.
A passive scalar is a quantity that is transported by the flow but does not back react on it. This scheme can be used to describe real scalar transport in the case where the back reaction of the scalar on the velocity field is negligible. Examples of passive scalars are dilute dyes, pollutants (see figure 2(b)) or temperature in the case where buoyancy is negligible. Scalar structures are bound to decay in the absence of any external source of fluctuations. If an external pumping is considered, at scales smaller than the injection lenghtscale, a flux of scalar fluctuations develops. The presence of the flux indicates that these spatial scales

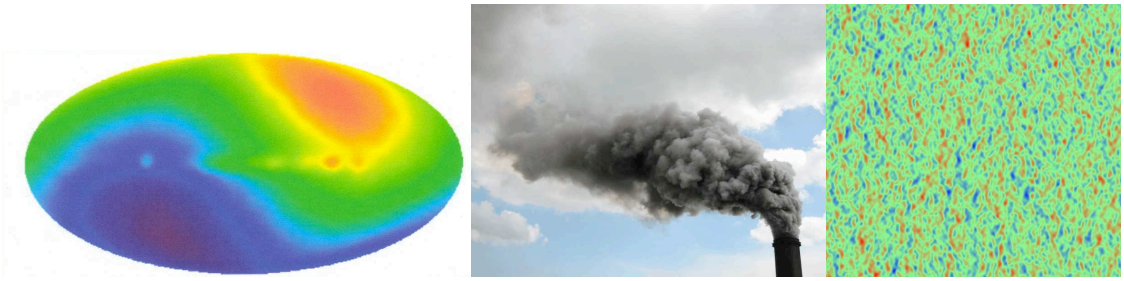

(a) (b) (c)

Figure 2: (a) Large scale anisotropy of the cosmic microwave background radiation is supposed to trace back to the origin of the universe. (b) Instance of real scalar turbulence. (c) Scalar snapshot obtained by the direct numerical simulations described in part II, chapter 2. Notice the elongated structure, preferentially aligned in the vertical direction.

cannot be in equilibrium. In this range of scales the passive scalar phenomenology strongly resembles that of hydrodynamic turbulence, hence the meaning of the expression "scalar turbulence". On the contrary, thermal equilibrium is expected at scales larger than the injection scale, where no upscale flux is present. Surprisingly enough, this is not the general case, as I will show in part II.

Part II is devoted to describe two sets of results obtained for the large-scale structure of passive scalar turbulence. In the isotropic case, the violation of equilibrium occurs at the level of the multipoint statistics. This has been firstly obtained in the Kraichnan model for passive scalar advection in [4]. I generalized this result to realistic flows through direct numerical simulations of a passive scalar advected by a two-dimensional turbulent flow in the inverse cascade. The breakdown of Gibbs equilibrium is here related to the presence of long-range correlations between two evolving scalar blobs within the turbulent flow.
The violation of equilibrium expectation is even more dramatic for the anisotropic case, since it occurs already at the level of the two-point statistics. I obtained the result first analytically in the framework of Kraichnan model. The Lagrangian interpretation of the result suggested that the same result may hold for realistic flows as well. I performed a numerical analysis of the problem that showed consistency with the theoretical results. From a single scalar snapshot one can detect elongated structures much larger than the scalar injection scale (see figure 2(c)). This means that a small degree of anisotropy introduced at small scales propagates toward large scales where it eventually dominates the structure of the concentration field.

Part III: turbulent transport of condensing droplets

The third part is dedicated to the theoretical problem of droplet condensation/evaporation in a turbulent moist environment. Applications of this general issue cover the most diverse fields from cloud physics [10] to meteorology, engineering [13] and health care [8] (see figure 3). For instance, medicines assumed by inhalation undergo dramatic size changes by

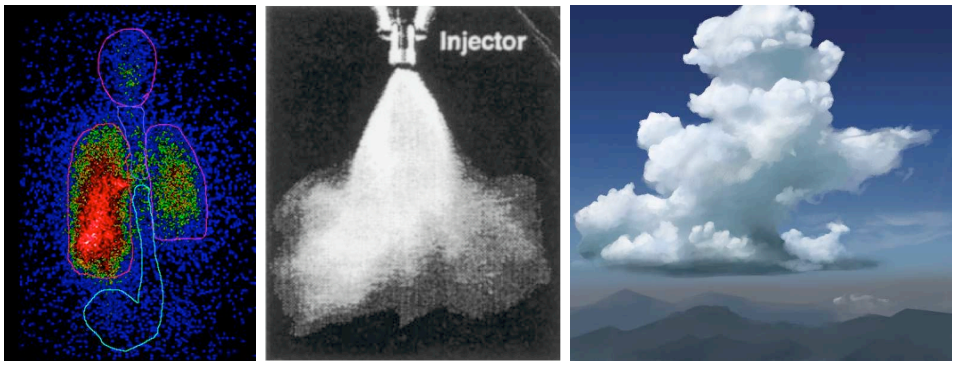

Figure 3: Turbulent condensation/evaporation in different physical systems. From left to right: aerosol drug (cyclosporine) deposition in the lungs; engine injector of fuel droplets; water droplets in warm clouds.

condensation/evaporation. This modifies the fraction of particles depositing on the walls of the respiratory tract. Therefore, their correct dose assessment requires a detailed description of transport and size dependent deposition in human airways. Additionally, exposure to atmospheric particulate and pollution may lead to inhalation of toxic particles. The local pattern depositions of inhaled particles are considered crucial in the formation of lung cancer [1]. Note that turbulence may locally develop inside human airways according to the rhythm of breathing and this can deeply affect the process of particle change in size.
As another instance, the evaluation of evaporation in turbulent flows is crucial for engineering. A correct design of spark ignition engines requires to account for turbulence [13]. Indeed this is essential to enhance the fuel-air mixing and the rate of fuel vaporization inside the combustion chamber.
Though in a completely different framework, the same ingredients are relevant to cloud physics as well. In particular, the rapidity of the rain initiation process still eludes a full theoretical understanding. In order to become raindrops, droplets must grow from $1\,\mu m$ till few mm in size. Although collisions can be a very effective growth mechanism, their initiation requires sufficiently large and different droplets. Before the collision stage, droplets grow by condensation. Mean field type arguments, applied to the condensational growth, lead to a fast narrowing of the droplet size distribution. On the basis of this wrong expectation, condensation would produce a population of almost identical droplets, that would hardly collide and would be eventually unable to produce rain. My suggestion is that a spreading of droplet size distribution can be ascribed to turbulence. However, due to the hard in situ measurements, to the lack of analytical description of turbulence and to the huge number of degrees of freedom that prevents a detailed numerical analysis, the evaluation of turbulent effects on cloud droplet condensation has been only partial until now.

In order to evaluate the strong couplings typical of turbulent transport, I chose a numerical approach. I considered a simple model of condensation accounting for small water droplets and a vapor field advected by a turbulent flow. The vapor field is considered as a passive scalar. Despite the simple setting, I could obtain non-trivial effects that are direct consequences of turbulent transport. The first observation is that droplets are segregated in moist regions. To justify this mechanism, I simply supposed that droplets dwelling in dry regions evaporated completely, leaving dry regions void of particles. This argument implicitly requires the presence of correlations: droplets persist for long enough time in dry regions, so

that they disappear. I quantitatively verified the presence of correlations tracing back their origin to the underlying velocity field. The consequence of these correlations are twofold: *(i)* despite the presence of a vapor field with zero average, the population of droplets can grow on average; *(ii)* droplets inside moist regions grow much faster than droplets inside dry regions, thus broadening the size spectrum.
By enlightening correlations mechanisms providing a fast growth and broadening of the size distribution I showed that mean field arguments cannot capture, here, crucial features of condensation/evaporation in turbulent flows.

Bibliography

[1] I. BALASHAZY, W. HOFMANN and T. HEISTRACHER. Local particle deposition patterns may play a key role in the development of lung cancer. *J. Appl. Physiol.*, **94** 1719-1725, (2003).

[2] M. CHERTKOV, G. FALKOVICH, I. KOLOKOLOV and V. LEBEDEV. Normal and anomalous scaling of the fourth-order correlation function of a randomly advected passive scalar. *Phys. Rev. E*, **52** 4924-4941, (1995).

[3] B. DUPLANTIER and H. SALEUR. Winding-angle of two-dimensional self-avoiding walks from conformal invariance. *Phys. Rev. Lett.*, **60** 2343-2346, (1988).

[4] G. FALKOVICH and A. FOUXON. Anomalous scaling of passive scalar in turbulence and in equilibrium. *Phys. Rev. Lett.*, **94** 214502, (2005).

[5] K. GAWEDZKI and A. KUPIAINEN. Anomalous scaling of the passive scalar. *Phys. Rev. Lett.*, **75** 3834-3837, (1995).

[6] R. H. KRAICHNAN. Anomalous scaling of a randomly advected passive scalar. *Phys. Rev. Lett.*, **72** 1016-1019, (1994).

[7] B. MANDELBROT. How long is the coast of britain? statistical self-similarity and fractional dimension. *Science*, **156** 636-638, (1967).

[8] T. B. MARTONEN. *Medical applications of computer modeling*. WIT Press, UK, (2001).

[9] C. H. PETERSON, S. D. RICE, J. W. SHORT, D. ESLER, J. L. BODKIN, B. E. BALLACHEY and D. B. IRONS. Long-term ecosystem response to the exxon valdez oil spill. *Science*, **302** 2082-2086, (2003).

[10] H. R. PRUPPACHER and J. D. KLETT. *Microphysics of Clouds and Precipitation*. Kluwer Academic Publishers, Boston, (1997).

[11] B. SAPOVAL, A. BALDASSARRI and A. GABRIELLI. Self-stabilised fractality of seacoasts through damped erosion. *Phys. Rev. Lett.*, **93** 098501, (2004).

[12] B. I. SHRAIMAN and E. D. SIGGIA. Anomalous scaling of a passive scalar in turbulent flow. *C. R. Acad. Sci. Série II*, **321** 279-284, (1995).

[13] F. ZHAO, M. C. LAI and D. L. HARRINGTON. Automotive spark-ignited direct-injection gasoline engines. *Prog. in Ener. and Comb. Sci.*, **25** 437-562, (1999).

Part I

Diffusion toward rocky coastlines

Introduction

This part of the thesis is devoted to the issue of diffusion toward rocky coasts, view as a problem of theoretical physics. The dispersion of pollutants in the environment is an issue of great importance for life on Earth. Pollution in the oceans has a great impact on marine life, as demonstrated by many examples of disasters occurred all over the world. The famous *Prestige* tanker began to leak large amounts of oil off the Galician coast on 13 November 2002. The spill polluted thousands of kilometers of coastline and more than one thousand beaches on the Spanish, Portuguese and French coasts, causing great damage to the local fishing industry. The amount of oil spill was estimated in roughly $64,000$ tons, and the ecological and economic consequences are still far from over [6]. Newspapers were flooded of pictures of dead birds, of fishermen trying to hold back the waves of oil with their hands, of huge black slicks along one of Europe's most beautiful coastlines, and of thousands of volunteers struggling with the clean up.

(a) (b) (c)

Figure 4: (a) Images of the oil spill originating from the stricken Prestige tanker, lying 100 km off the North-Western Spanish coast. (b) Volunteers cleaning a beach in Galicia in the aftermath of the catastrophe. (c) Oil spills are also responsible for the death of fish and sea birds.

Diffusion is one of the mechanisms that contribute to the dispersion of pollutant and is of crucial importance for the understanding and prediction of this problem. The well-known equation of diffusion relates this phenomenon to apparently unconnected physical processes like heat transfer, electrostatics and wave propagation. This long-studied equation has trivial solutions when the domain of interest has some special geometry. However, it remains a challenging problem when the geometry of the system becomes complex, which is definitely the case for coastlines. The same equation in an abstract context defines a class of functions

of special interest in complex analysis, which are called harmonic functions. The branch of mathematics dealing with this kind of problems has developed a theory of what is called *harmonic measure* of a fractal curve, providing a set of useful results for our problem.
Rocky coasts possess a special nature, whose importance has been recognized long ago, by Mandelbrot [19], following some empirical observations by Richardson [22]. They are fractals, i.e. each portion can be considered as a reduced-scale image of the whole. In other words, the level of complexity of the spatial structure of the coastline is invariant under scale transformations (corresponding to zooms of the coastlines showing more and more details). There is a number of different examples showing how the understanding of problems in physics can greatly benefit from the concept of symmetry. The key-idea guiding my work is that rocky coasts might enjoy a much richer degree of symmetry than mere scale invariance i.e. *conformal invariance*. Conformal invariance is the symmetry with respect to the class of transformations that preserve angles. Since this is a strong constraint for a transformation, typically the group of conformal transformation is finite. In two dimensions something special happens: the angle-preserving condition reduces to the Cauchy-Riemann relations, so that the whole class of analytic functions in the complex plane fulfills the requirement, thus providing an infinite-dimensional group of conformal transformations. In turn, the set of conformal invariant objects enjoys a consistently high degree of symmetry and conformal field theories in two dimensions are extremely powerful in providing analytical results (see [4, 7, 9, 20] and references therein).
The fractal nature of rocky shorelines has been studied in a recent paper [24], where a stochastic model for the erosion dynamics has been proposed, whose strong connection with *percolation* is a further hint at conformal invariance. Indeed, in mathematics percolation theory describes the behavior of connected clusters in a random graph, which have been proved to be conformally invariant objects [25].
I proved that the above picture is correct: rocky shorelines display a conformally invariant statistics. I obtained the result by analyzing real satellite data of the world coastlines and synthetic data we obtained by direct numerical simulations of a model of erosion adapted from [24]. The conformal invariance of rocky shorelines not only represents a theoretical advancement, but also allows to apply the powerful theory of conformal invariant curves in two dimensions to characterize the diffusion process toward rocky coasts.

In this part of the thesis I will first describe some background results concerning conformal invariance (chapter 1) and diffusion to random curves (chapter 2). Diffusion and conformal invariance are the two ingredients at the basis of the results I obtained for diffusion toward rocky shorelines, that are presented in chapter 3. These have been collected in the paper presented at the end of this part which is now under revision.

Chapter 1

Conformal invariant curves

One of the most common properties of natural curves is scale invariance, i.e. fractality. Fractal curves like those shown in figure 1.1 are widespread in nature. Conformal invariance is an interesting "upgrade" of scale-invariance, especially in two dimensions (2D). A conformal map is a transformation that locally preserves angles between lines and pure scale transformations are only a subset of the whole group of conformal maps. Therefore a conformal invariant curve enjoys a much richer degree of symmetry than a simple fractal. In particular in 2D the group of conformal transformations is infinite dimensional and conformal invariance allows for substantial analytic advancements. This is the case for many systems in two-dimensional physics spanning from quantum gravity to string theory, statistical mechanics and two-dimensional turbulence [5]. In this chapter I review some background concepts related to conformal invariance. I first define the group of conformal transformations and describe them in two dimensions. Then I introduce conformally invariant curves and briefly sketch the contexts where they were originally considered and exhaustively characterized. I finally show hallmarks of these curves that can disclose their conformal invariant nature.

(a) (b) (c)

Figure 1.1: Examples of natural fractal curves and surfaces: (a) a cauliflower (b) a bolt of lightening (c) frost on the branches of a tree.

1.1 Conformal mappings

Let $\mathcal{D}$ be a generic manifold and let f be a mapping from $\mathcal{D}$ to another manifold $\mathcal{D}'$. The transformation f is a conformal mapping *if it locally preserves relative angles between vectors* in the tangent space. Note that this is a useful concept in a well-known ancient application like cartography. A map projection faithfully reproducing all features of the globe would have the property that distances between every two points would keep the same ratio on both map and sphere. Therefore, all shapes would also be preserved. On a flat map this property is simply not possible (as proved by points at the map's edges). For many mapping applications - like navigation, where it is more important to aim in the right direction than to know the exact distance left - a lesser constraint may be required. Namely, the angle between any two lines on the sphere may be required to be the same as the angle between their projected counterparts on the map. Such map would be a conformal map. If we ask for a conformal map, we cannot put any other constraint on the surfaces. Therefore in different conformal projections of the globe continents possess different surfaces (compare e.g. the surface of Greenland and Africa in figure 1.2)

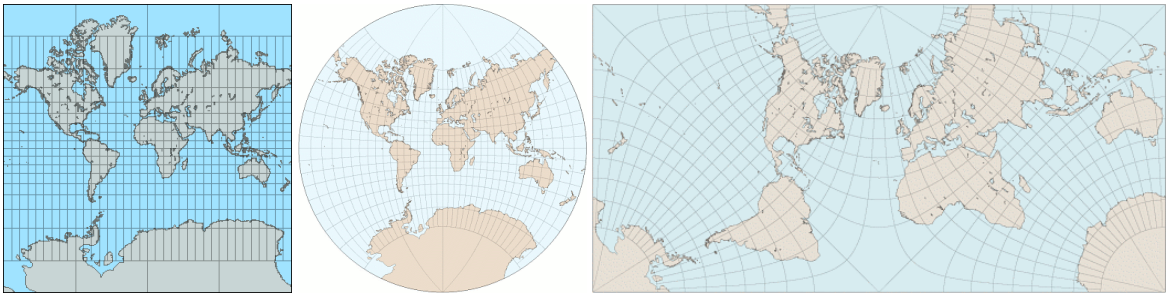

(a) (b) (c)

Figure 1.2: Examples of conformal projections of the globe into a planar map. (a) Mercator map - 1569 (b)"Lagrange" projection, due to Lambert - 1772; (c) Oblique Guyou map - 1925.

For our purposes it is sufficient to imagine $\mathcal{D}$ and $\mathcal{D}'$ as subsets of a d-dimensional Euclidean space with metric tensor $g^{\mu\nu}$. Let f be an infinitesimal transformation defined in coordinates by:

$$x^\mu \rightarrow x'^\mu = x^\mu - \alpha^\mu(x) \tag{1.1}$$

Here we shall always assume that (1.1) is sufficiently differentiable and that the determinant does not vanish so that, at least locally, the mapping is one to one. Under these assumptions we can use the x^μ as coordinates in $\mathcal{D}'$ also, corresponding points on the two manifolds will thus have the same coordinates. We define the matrix of derivatives $J^\mu_\nu = \partial\alpha^\mu/\partial x^\nu$. Its components $J_{\mu\nu}$ can be written as a sum of three terms:

- a diagonal part $\frac{1}{d}J^\lambda_\lambda g_{\mu\nu}$ which corresponds to a dilatation or to a contraction;
- an antisymmetric part $\frac{1}{2}(J_{\mu\nu} - J_{\nu\mu})$ corresponding to a local rotation;

- a traceless symmetric part $\frac{1}{2}(J_{\mu\nu} + J_{\nu\mu} - \frac{2}{d}\, J^{\lambda}_{\lambda} g_{\mu\nu})$.

The last part may be thought of as the components of a local shear and therefore this must vanish in order to preserve the angles. From this argument, we conclude that, in order for f to be a conformal map, it should satisfy the condition:

$$\frac{\partial \alpha_\mu}{\partial x^\nu} + \frac{\partial \alpha_\nu}{\partial x^\mu} - \frac{2}{d}\frac{\partial \alpha^\lambda}{\partial x^\lambda} g_{\mu\nu} = 0. \tag{1.2}$$

A mapping by equal coordinates between two Riemannian spaces can also be given another interpretation: the inverse mapping from $\mathcal{D}'$ to $\mathcal{D}$ can be used to produce a second metric $g'^{\mu\nu}$ in $\mathcal{D}$. In this way we can consider, instead of a mapping between two spaces, a single manifold with coordinates x^μ, equipped with two alternative metrics g and g'. In this framework, it is easy to show that, in order for a given f to preserve angles between vectors, the metric tensor should transform under f as:

$$g'^{\mu\nu}(x) = \Omega(x) g^{\mu\nu}(x). \tag{1.3}$$

Since $\Omega(x)$ is a (positive) scalar quantity, although the transformation changes the vectors' length, it does not change the relative angles. Indeed the angle θ between vectors u and v is defined by

$$\cos\theta = \frac{g_{\mu\nu} u^\mu v^\nu}{\sqrt{|g_{\mu\nu} u^\mu u^\nu||g_{\mu\nu} v^\mu v^\nu|}}$$

The same angle, measured with the alternative metrics g' is simply:

$$\cos\theta' = \frac{g'_{\mu\nu} u^\mu v^\nu}{\sqrt{|g'_{\mu\nu} u^\mu u^\nu||g'_{\mu\nu} v^\mu v^\nu|}} = \frac{\Omega(x) g_{\mu\nu} u^\mu v^\nu}{\sqrt{|\Omega(x) g_{\mu\nu} u^\mu u^\nu||\Omega(x) g_{\mu\nu} v^\mu v^\nu|}} = \cos\theta \tag{1.4}$$

Therefore, if f satisfies equation (1.3), then it is a conformal map. It is easy to show that when the metric tensor transforms as in (1.3), we have:

$$\frac{\partial x'^\mu}{\partial x^\gamma}\frac{\partial x'^\nu}{\partial x^\lambda} = \Omega(x)^{-1}\delta^\mu_\gamma \delta^\nu_\lambda \tag{1.5}$$

Note that, after saturation of index μ with index γ and index ν with index λ, equation (1.5) tells us how Ω depends on the transformation:

$$\Omega^{-1} = \left(\frac{\partial x'^\mu}{\partial x^\mu}\right)^2 \frac{1}{d^2} \quad \Rightarrow \Omega \approx (1 - \frac{2}{d}\frac{\partial \alpha^\mu}{\partial x^\mu}) \text{ for infinitesimal } \alpha^\mu \text{ given by (1.1).} \tag{1.6}$$

By focusing on an infinitesimal transformation, it is easy to show that (1.3) is equivalent to the no-shear condition (1.2). Indeed given the map (1.1) and considering α^μ infinitesimally small, we can explicitly write the increment of the metric tensor:

$$g'_{\mu\nu} = \frac{\partial x^\gamma}{\partial x'^\mu}\frac{\partial x^\lambda}{\partial x'^\nu} g_{\gamma\lambda} = (\delta^\gamma_\mu - \frac{\partial \alpha^\gamma}{\partial x'^\mu})(\delta^\lambda_\nu - \frac{\partial \alpha^\lambda}{\partial x'^\nu}) g_{\gamma\lambda} = g_{\mu\nu} - (\frac{\partial \alpha^\gamma}{\partial x'^\mu}\delta^\lambda_\nu + \delta^\gamma_\mu \frac{\partial \alpha^\lambda}{\partial x'^\nu}) g_{\gamma\lambda} + O(\alpha^2).$$

Hence the increment of the metric tensor is:

$$\delta g_{\mu\nu} = g'_{\mu\nu} - g_{\mu\nu} = -(\frac{\partial \alpha_\nu}{\partial x'^\mu} + \frac{\partial \alpha_\mu}{\partial x'^\nu}) = -\frac{2}{d}\frac{\partial \alpha^\lambda}{\partial x^\lambda} g_{\mu\nu}$$

where in the last passage we have used the condition (1.3) with the expression (1.6) for the constant Ω in the limit of infinitesimal transformation. This equation is exactly the no-shear condition (1.2).

By direct calculation, it is easy to show that solutions of equation (1.2) are:

- translations: α_μ constant
- rotations: $\alpha_\mu = \omega_{\mu\nu} x^\nu$, with ω antisymmetric
- scale transformations: $\alpha_\mu = \Lambda x_\mu$
- special transformations: $\alpha_\mu = x_\mu / (g_{\gamma\lambda} x^\gamma x^\lambda)$

One can show that these are generators of a *finite*-dimensional group if $d > 2$. Indeed, conditions (1.2) are very restrictive in high dimensions. This is not the case for $d = 2$, where a special simplification of conditions (1.2) occurs. By writing explicitly the $d \times d$ conditions (1.2) for $d = 2$, we note that there are only two independent pieces of information, one for $\mu = \nu$ and one for $\mu \neq \nu$:

$$\frac{\partial \alpha_1}{\partial x^1} = \frac{\partial \alpha_2}{\partial x^2} \tag{1.7}$$

$$\frac{\partial \alpha_1}{\partial x^2} = -\frac{\partial \alpha_2}{\partial x^1} \tag{1.8}$$

If we define a complex function $f(z) = \alpha_1(x+iy) + i\alpha_2(x+iy)$, relations (1.7)-(1.8) correspond to the Cauchy-Riemann equations. Therefore *every analytic function in the complex plane represents a conformal mapping in 2D*. Hence the peculiar character of conformal invariance in two dimensions.

1.2 Conformally invariant random curves

A conformally invariant curve is defined as a curve whose measure does not vary after a conformal transformation. More precisely, let γ be a curve in a subset D of $\Re^2$ and γ' the image of γ under a conformal map f. Let μ be a measure on $\Re^2$ with restrictions μ_D and $\mu_{D'}$ in D and D' respectively. The transformation f induces a measure of curves in D' - the *image measure*, denoted by $f * \mu_D$, and defined by $(f * \mu_D)(\gamma') = \mu_D(\gamma = f^{-1}(\gamma'))$. γ is a conformally invariant curve if the image measure of γ' is exactly the measure of γ':

$$(f * \mu_D)(\gamma') = \mu_{D'}(\gamma') \tag{1.9}$$

Note that this definition of conformal invariance applies also to random curves, given that a measure μ exists. Note that in two dimensions a non-intersecting curve is the boundary between two domains and can be interpreted as an interface separating two coexisting

phases of a physical system. Prominent examples of conformally invariant random curves are widespread in statistical mechanics of 2D critical systems. We present here a brief description of critical phenomena in order to give an idea of a context where all these ideas can be applied to physical systems.

Critical phenomena occur in statistical systems undergoing higher order phase transitions, e.g. Ising spins, Potts or $O(n)$ models or percolation. Typically one can deal with the problem at hand by dividing the volume of interest in boxes and defining on this discrete lattice all the physical observables (e.g. the spin for the Ising model). The dynamics of the system creates clusters of sites characterized by a certain value of some defined observable. For instance, for the Ising model, clusters are characterized by spin up or spin down. When the system attains its critical point, the correlation length on the lattice tends to diverge and there is a non-zero probability that a single cluster can extend from one side of the volume to the opposite side (see. e.g. [7]). The physical observables in this regime typically display a power-law behavior with respect to some parameter measuring the "distance" from the critical point. One of the most intriguing facts is that the scaling exponents of these power laws enjoy a universal character, whose motivation and quantitative description has been object of intense research.Indeed, in spite of their seemingly unrelated nature, systems with very different constituents and microscopic interactions can exhibit the same critical behavior. This provides a classification of critical phenomena in different *universality classes*.
When the renormalization group ideas were proposed and developed for critical phenomena [29], it turned out that at criticality the microscopical details of the specific dynamics on the lattice may become irrelevant from a macroscopic point of view. In this framework classical critical systems were put in relation with quantum field theories and these ideas opened the doors of a substantial unification of the theoretical basis of statistical mechanics and particle physics. Moreover it was observed that when the lattice spacing tends to zero - i.e. in the *scaling limit* - since the dynamics is not restricted to a lattice, critical phenomena may enjoy a higher degree of symmetry. In particular at criticality, due to the divergence of the correlation length, scale invariance may be promoted to conformal symmetry. This conjecture was rigorously proven for the scaling limit of some critical phenomena (e.g. for percolation in [26]). In this case one can apply a corresponding conformal field theory (CFT) [4] that turns out to be extremely powerful in two dimensions (see [4, 7, 9, 20] and references therein). In particular 2D CFTs are characterized by a single real parameter - the *central charge* - that provides a natural label for the different classes of universality of critical behavior.

The application of CFT to critical phenomena produced an enormous amount of exact results for the properties of conformally invariant critical clusters (see, e.g. [4, 7, 9, 20]). However, the universal properties of critical systems reflect also on the geometry of the interfaces between different clusters and this aspect of conformal symmetry is not apparent from the viewpoint of CFT. Recently, an alternative approach to conformal invariant systems was developed [25], whose focus is exactly on the random curves which form the boundaries of clusters on the lattice (see a schematic of percolation in figure 1.3 for instance). From this viewpoint, the question is what should be the properties of the measure on such curves in the continuum limit. It was shown by Löwner [18] in the 1920s that any conformally invariant curve, conditioned to start at the boundary of the domain and not to cross itself, can be described by a dynamical process called Löwner evolution. This process turns out to

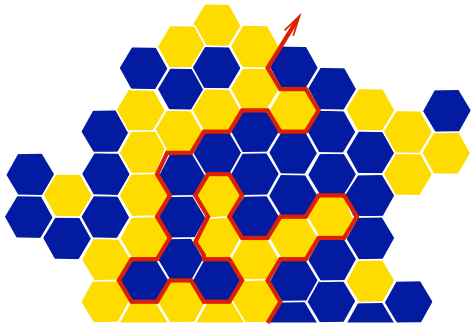

Figure 1.3: Sketch of percolation on hexagonal lattice. The focus of SLE is on the boundaries between dark and light clusters, like the one marked in red.

be completely determined by a real continuous function a_t. For random curves, a_t itself is a random process. Schramm showed that for random curves satisfying a further Markovian condition, if the measure on the curve is conformally invariant in the sense defined by (1.9), then a_t is a one-dimensional Brownian motion, whose diffusion constant k remains as the only parameter left undetermined, as we shall describe in section 1.3. This extension of the Löwner evolution is known as stochastic-Löwner-evolution (SLE) and the curves defined by this process appear to be[1] essentially the only possible candidates for the scaling limits of interfaces of two-dimensional critical systems (see e.g. [23] for a review). There is a one-parameter family of SLEs, indexed by the positive real number k, that provides a natural classification of the different universality classes of critical phenomena. This yields a connection between the central charge of CFT and the diffusion constant of SLE, which is only one aspect of the intimate relation between these two theories [1, 2].
In the context of critical phenomena, the curves γ and γ' of equation (1.9) are therefore the continuum limit of the random boundaries of clusters on a lattice. Different realizations of the equilibrium state of the system provide an ensemble of realizations of the curves, thus a probability concept for the discrete curves. The measure μ is derived from this same concept in the limit of vanishing lattice spacing. In this context, the meaning of conformally invariant curves (1.9) can be paraphrased as follows: the continuum limit γ of a random boundary is conformally invariant if its measure does not change when we perform the scaling limit on one lattice or on any of the conformal images of that lattice. In order to establish whether a curve is conformally invariant in the sense defined by (1.9), one can greatly benefit from SLE. In particular SLE gives useful information on the statistics of the *winding angle*, as described in the next section.

[1] This statement was proved for some models of critical phenomena. For instance, it was proved in [26] that the continuum limit of 2D critical percolation interfaces - whose conformal invariance was first conjectured by Schramm [25] - are indeed SLE_6. The scaling limit of loop-erased random walks have been proven to be SLE_2 in [17], where they also prove that SLE_8 describes the boundaries of uniform spanning trees.

1.3 Stochastic-Löwner evolution

In the following we will focus on the main ideas of SLE without dwelling on the detailed mathematical proofs that can be found either in the original paper by O. Schramm [25] or in recent reviews with a more physical (e.g. [3,8,12]) or mathematical (e.g. [14,27]) viewpoint.

SLE describes conformally invariant curves in the sense defined by (1.9), with a further Markovian property:

Property. Denoting by γ a curve from r_1 to r_2, and dividing it in two disjoint parts γ_1 from r_1 to τ and γ_2 from τ to r_2, the conditional measures on γ_1 and γ_2 satisfy: $\mu_D(\gamma_2|\gamma_1) = \mu_{D\setminus\gamma_1}(\gamma_2)$.

If the measure on γ satisfies both Markov property and conformal invariance then we can define a process through which γ can be mapped into a Brownian walk. Because of conformal invariance it suffices to describe this in a standard domain, e.g. the upper half plane $\mathbf{H}$.

1.3.1 Löwner's equation

Let us consider a curve $\gamma \subset \mathcal{D}$ connecting two points r_1 and r_2 on the boundary $\partial\mathcal{D}$. The conformal image of this curve in the upper half plane will connect a point r_1 on the real axis with the point at infinity. Let us consider the parametric description of the curve and let us indicate with $\gamma(t) \subset \mathbf{H}$ the portion of the curve that is defined by the values of the parameter from 0 until t. We indicate with τ_t the tip of the curve γ_t. When $t \to \infty$, the tip tends to the point at infinity. We do not assume the simplicity of γ, so in general it can touch itself as in figure 1.4 but still we assume that it cannot cross itself[2]. The *hull* of γ is defined as the set of points that cannot be reached from infinity without hitting the curve plus the curve itself (see 1.4 for a schematic representation).

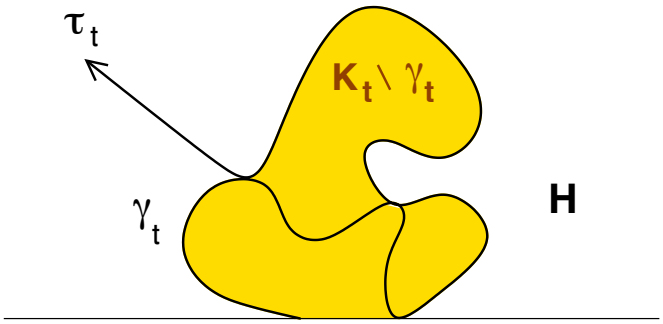

Figure 1.4: Schematic of a curve γ touching itself in the upper half plane $\mathbf{H}$. The hull of the curve minus the curve itself is colored.

The upper half plane minus the hull of γ is an open, simply connected domain and can therefore be mapped onto the upper half plane itself by Riemann theorem. The map is unique upon imposing the following behavior as $z \to \infty$:

[2]For critical phenomena this comes from the fact that it represents the continuum limit of an interface, so the minimum distance between two points on the curve is the space lattice. When we take the continuum limit, the curve can touch itself, but still cannot cross itself.

$$g_t(z) \sim z + \frac{2t}{z} + O\left(\frac{1}{z^2}\right).$$

The function $g_t(z)$ maps the whole boundary of K_t onto the real axis, thus in particular the tip τ_t is mapped onto a real number a_t. Löwner's idea was to describe the curve γ_t and its tip in terms of the conformal mapping $g_t(z)$, whose evolution is described by the *Löwner equation*:

$$\frac{dg_t(z)}{dt} = \frac{2}{g_t(z) - a_t}. \tag{1.10}$$

The proof of this equation directly comes by building the conformal map g_t as the composition of a series of infinitesimal conformal maps that grow infinitesimally small slices of the curve. From equation (1.10) it turns out that the map g_t is fully characterized by the *driving function* a_t.

1.3.2 Stochastic-Löwner evolution

When γ is a stochastic curve, the tip τ_t is mapped onto a random variable a_t. The remarkable result obtained by Schramm in [25] is that, if conformal invariance and Markov property hold, the increments of a_t must be independent and identically distributed, i.e. a_t must be a Brownian motion

$$a_t = \sqrt{k} B_t$$

The locality in time of the Brownian motion translates into the local scale invariance of SLE curves, namely conformal invariance. Therefore the variance of a_t is given by $\langle (a_{t_1} - a_{t_2})^2 \rangle = k|t_1 - t_2|$. Given a growing path, one can in principle determine the hull K_t and the map $g_t(z)$. Then one can find the image of the tip a_t and observe its probability distribution and its variance. A discretized version of the map $g_t(z)$ can be computed numerically, thus giving an algorithm to state whether a curve is conformally invariant or not.

There are variants of the *chordal* SLE described above, that apply to different situations. Until now we have characterized curves γ connecting two points of the boundary of a simply connected domain (a point of the real axis and the point at ∞ on the upper half plane $\mathbf{H}$). One can also consider a curve connecting a point r_1 on the boundary of the domain to a given internal point r_2. In this case the most convenient standard domain where we can describe the growing process is a unit disk $\mathbf{U}$, where r_1 is a point on the boundary of the disk and we can take r_2 to be the origin. By Riemann mapping theorem we can now map $\mathbf{U} \setminus K_t$ into the unit disk itself (K_t being the hull). In this case, the growing tip of the curve is mapped onto a point of the unit circle and we can impose $g_t(0) = 0$ and a normalization such that:

$$\frac{dg_t(z)}{dt} = -g_t(z) \frac{g_t(z) + e^{ia_t}}{g_t(z) - e^{ia_t}},$$

which defines a precise parameterization t of what is called *radial* SLE. It can be argued, as before, that given conformal invariance and Markov property a_t must be proportional to the standard Brownian motion. One property of radial SLE, that is not present in chordal SLE, is that the path can *wind* around the origin, as defined in the following.

1.3.3 Winding angle statistics

The *winding angle* $\Theta(t)$ around the origin, starting from point r_1, is defined as $\Theta(t) = \arg(\tau_t) - \arg(\tau_0)$. It turns out (see [25]) that, in the limit of large t, $|\log|\tau_t|| \to t$, and $\Theta(t)/\sqrt{kt}$ tends to a Gaussian with unit variance. Putting together the two informations we have that the variance of the winding angle is:

$$\langle \Theta^2 \rangle \sim kt \sim k|\log R_t|.$$

where $R_t = |\tau_t|$. Going back to the original domain $\mathcal{D}$, the winding angle is now $\Theta = \arg(r_1) - \arg(x)$ (see [11]), where now r_1 is not forcely a point of the unit circle and $x \in \gamma$. One can also define a winding angle around an internal point $x_w \in \gamma$ simply by: $\Theta = \arg(x_w) - \arg(x)$, as schematically represented in figure 1.5. It has been proved in [28] that the winding angle around a point $x_w \in \gamma$ where m strands of the curve come together[3], is again normally distributed, with variance:

$$\langle \Theta^2 \rangle = \frac{k}{m^2} \log R \tag{1.11}$$

where R is the euclidean distance between x_w and x. Equation (1.11) and the Gaussianity of the winding angle are properties of γ that can be useful to prove its conformal invariance. Note that the relation between the linear distance R and the length of the curve L between x_w and x is $L \sim R^D$, where D is the fractal dimension of the curve γ. Also note that the winding angle is defined up to an additive constant which is determined by the orientation of the coordinate system and does not affect the variance of the winding angle.

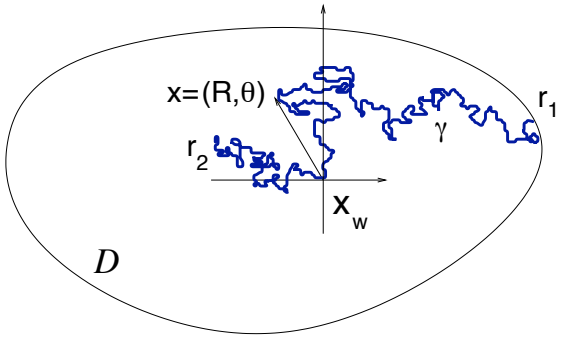

Figure 1.5: Schematic of the winding angle around a generic point x_w of the curve γ.

[3]For $m = 1$ we have that x_w is a boundary point of the curve, for $m = 2$ it is a simple point, for $m > 2$ it is a point where the curve touches itself.

Chapter 2

Diffusion toward random boundaries

The problem of diffusion to a fractal curve has been long studied, yet it still poses great challenges in mathematical physics. This mechanism is at the basis of diffusion-limited aggregation (DLA) where particles undergoing a random walk due to Brownian motion cluster together to form aggregates. DLA clusters are a pervasive feature of the living as well as the non-living world. Examples of spatial structures observed in DLA growing clusters are shown in Figure 2.1.
The problem of diffusion in the stationary state can be mathematically formulated as a Laplace partial differential equation with Dirichlet boundary conditions. The solution is the concentration field undergoing diffusion over the fractal line, but can be equivalently reread as the electrostatic potential generated by a charged conductor with the same fractal curve as boundary. The self-similar structure of the curve is reflected in a multifractal behavior of the potential near the curve. In the context of DLA the potential actually determines the growth process and its scaling properties are intimately related to those of the cluster itself. For the case where the fractal curve is conformally invariant in two dimensions, conformal field theory provides helpful tools to investigate the structure of diffusion in the vicinity of the curve. In this chapter I first pose the problem and establish the connection between electrostatics and diffusion, then I describe the background results for the diffusing field and its flux obtained in the context of CFT.

2.1 Diffusion and electrostatics

The problem of diffusion of the concentration ρ (for instance a pollutant diffusing toward coastlines) is governed by the well-known diffusion equation:

$$\partial_t \rho = k\Delta\rho + f \tag{2.1}$$

where k is the diffusion constant and f is the source/sink of pollutant. We now wish to study the problem in two dimensions, with a constant source of pollutant $f = f_0\delta(R - R_0)$ at a very large distance R_0 from a region C, delimited by a fractal boundary ∂C, where we consider absorbing boundary conditions. The stationary state is reached when the flux coming from the source is entirely absorbed on ∂C. In this case equation (2.1) reduces to:

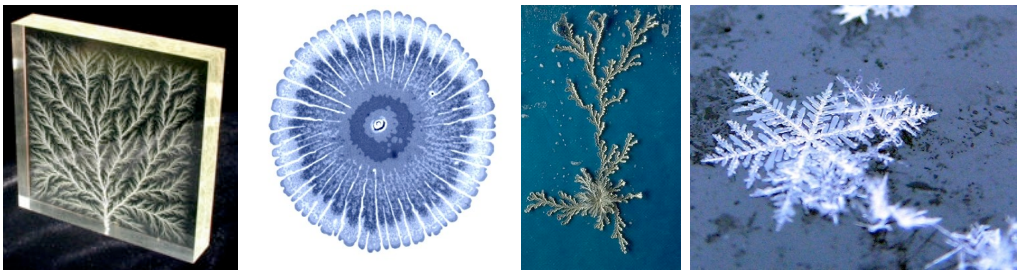

(a) (b) (c) (d)

Figure 2.1: (a) High-voltage dielectric breakdown within a block of plexiglas. (b) Pattern formed by bacteria grown in a Petri dish. (c) Copper aggregate formed from a copper sulfate solution in an electrodeposition cell. (d) Snowflake.

$$\Delta\rho = -\frac{\phi_0}{2\pi R_0}\delta(R - R_0) \tag{2.2}$$

where $\phi_0 = 2\pi R_0 f_0/k$ is the flux coming from the source[1]. Equation (2.2) can then be translated into an equivalent Laplace equation with Neumann boundary conditions at R_0 and Dirichlet boundary conditions on the cluster:

$$\Delta\rho = 0 \quad \text{for } z \in B(R_0) \setminus C \tag{2.3}$$

$$\partial_r\rho|_{R_0} = \frac{\phi_0}{2\pi R_0} \quad \text{for } z \in \partial B(R_0) \tag{2.4}$$

$$\rho = 0 \quad \text{for } z \in \partial C \tag{2.5}$$

where $B(R_0)$ is a circle with radius R_0 and $\partial B(R_0)$ is its boundary i.e. the circumference with radius R_0. We will focus on the field ρ in the vicinity of C, i.e. at a distance R from ∂C such that $R \ll R_0$.
As mentioned above, equations (2.3)-(2.5) are equivalent to the electrostatic problem of finding the potential generated by a perfect conductor with surface C, where in this case ϕ_0 has the meaning of the total charge of the conductor C. Indeed, the electrostatic potential $\mathcal{H}$, by Maxwell equations, satisfies the Laplace equation in every point out of C, where no electric charge is present. The electric field $\mathbf{E} = \boldsymbol{\nabla}\mathcal{H}$ in the circumference of radius R_0 is $\phi_0/(2\pi R_0)$ by Gauss theorem. Finally the condition at the boundary of the conductor gives a constant potential, that can be chosed to vanish yielding the problem (2.3)-(2.5).

[1]This is the total flux coming from infinity, as one can easily see by simply integrating equation (2.2) over a circle of radius R_0: $\int \boldsymbol{\nabla}\cdot\boldsymbol{\nabla}\rho R\, dR\, d\theta = \phi_0$. The first member can be written by divergence theorem as an integral over the circumference: $\int_0^{2\pi} R_0 d\theta \partial_r\rho$. This finally provides $2\pi R_0\partial_r\rho|_{R_0} = \phi_0$: ϕ_0 has the meaning of the flux of pollutant emitted by the source, and entering the volume of interest from far.

2.2 Theory of the potential for conformally invariant curves

In the context of conformal field theory, a whole class of fractal structures arise. Indeed, in two dimensions, statistical systems at their critical point are expected to produce conformally invariant fractal clusters whose prominent examples are the continuum limit of random walks, critical percolation, Ising or Potts clusters, as discussed in chapter 1. Inquiries into the stochastic geometry of these structures are relatively recent and make use of both traditional CFT [9, 10] and SLE [15, 16]. In this framework, C represents a critical random cluster produced by a statistical system and ∂C is its fractal boundary. Classical potential theory of electrostatic and diffusion fields near these random fractal boundaries represents in this context a refined way of accessing their random geometry. Indeed the self-similarity of the latter is reflected in a multifractal spectrum of the potential. The electrostatic potential $\mathcal{H}$ generated by a unit charge distributed along the boundary ∂C of a conductor occupying the region C satisfies the Laplace equation in each point out of the cluster, and Dirichlet boundary conditions $\mathcal{H}|_{\partial C} = 0$. Let us define $\mathcal{H}$ with a further[2] boundary condition on a circle of radius $R_0 \gg 1$: $\mathcal{H}|_{|z-w|=R_0} = 1$. The concentration ρ of the diffusion problem is therefore proportional to $\mathcal{H}$

$$\rho = \phi_0 \mathcal{H} \tag{2.6}$$

As is well known [13], in each point the potential is the probability that a Brownian walk starting from that point escapes to infinity without hitting the curve ∂C. One can also consider the *harmonic measure* $H(w, r)$ which is the integral of the Laplacian of $\mathcal{H}$ in a disk of radius r centered at $w \in \partial C$. In the analogy with electrostatics, the harmonic measure corresponds to the total charge contained in the portion of ∂C delimited by the circle of radius r centered at $w \in \partial C$ (see figure 2.2(a)). The potential and the harmonic measure in the vicinity of ∂C have the same scaling properties. With the help of the multifractal formalism, these scaling properties in the vicinity of the cluster define a local Hölder exponent α such that:

$$\mathcal{H}(z \to w \in \partial C_\alpha) \approx \frac{|z-w|^\alpha}{R_0^\alpha} \tag{2.7}$$

The analysis of a simplified shape of the boundary ∂C allows for a simple geometrical interpretation of α. Let us focus on a wedge of opening angle θ, centered in w. The complex potential $\psi(z)$ is defined so as to satisfy $\mathcal{H} = \Im\psi$ and $|\boldsymbol{\nabla}\mathcal{H}| = |\psi'(z)|$. Note that $\boldsymbol{\nabla}\mathcal{H}$ corresponds to the local flux vector for diffusion and to the electric field for electrostatics. Inside the wedge the complex potential is $\psi = (z-w)^{(\pi/\theta)}$, so that in polar coordinates as in Figure 2.2(b):

$$\mathcal{H}(r, \beta) = r^{\pi/\theta} \sin(\beta\pi/\theta) \tag{2.8}$$

Comparing equation (2.8) with equation (2.7) we can conclude that the Hölder exponent α locally defines an angle $\theta = \pi/\alpha$, and the curve ∂C can be considered as a superposition of wedges of different openings. In this sense the study of the potential $\mathcal{H}$ in the vicinity of the cluster captures the local geometrical properties of the curve ∂C.
Let $f(\alpha)$ be the Hausdorff dimension of the subset of ∂C characterized by Hölder exponent α - that we indicate with ∂C_α. By assuming conformal invariance of ∂C, one can relate the

[2] In the limit for large R_0 the solution of this problem coincides with the solution of the problem (2.3)-(2.5) with $\phi_0 = 1$.

Hausdorff dimension $f(\alpha)$ to the central charge c of the underlying conformal field theory (or equivalently to the parameter k of the corresponding Stochastic Löwner Evolution). This result has been first obtained in [9]:

$$f(\alpha) = \alpha + b(1 - \frac{\alpha^2}{2\alpha - 1}) \tag{2.9}$$

where $b = (25 - c)/12$ and c is the central charge.
We can equivalently express b as a function of the fractal dimension D of the boundary ∂C remembering that $c = (3D - 4)(7 - 4D)/(D - 1)$, so that $b = (2D - 1)^2/[4(D - 1)]$. In this way we end up with an expression which does not appeal to the physics of the statistical process generating the cluster, but only to the geometrical properties of the conformally invariant random curve ∂C.

2.3 Flux over conformal invariant curves

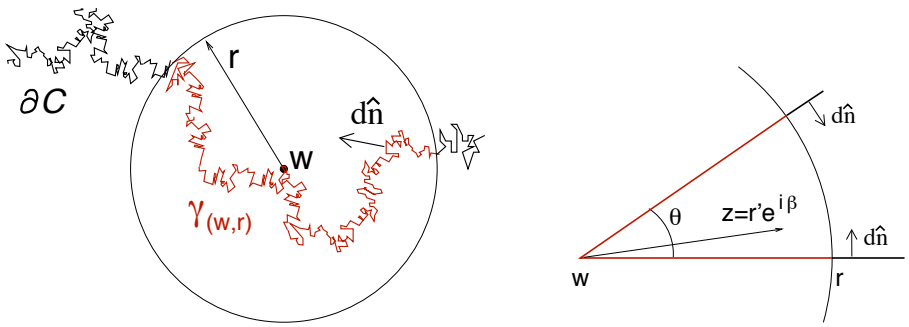

Figure 2.2: (a) Scheme of the meaning of symbols in equation (2.10). (b) Schematic picture of the particular case where the curve $\gamma_{w,R}$ is a wedge.

Let us now focus on the flux ϕ_r of the electric field $\mathbf{E} = \boldsymbol{\nabla}\mathcal{H}$ over the portion of the curve $\gamma_{w,r} \in \partial C$ delimited by a circle of radius $r \ll 1$, centered in $w \in \partial C$ (see Figure 2.2(a)):

$$\phi_r = \int_{\gamma(w,r)} \mathbf{E} \cdot d\hat{n} \tag{2.10}$$

Note that by equation (2.6) the flux of the diffusing field ρ is proportional to ϕ_r by $\boldsymbol{\nabla}\phi = \phi_0\mathbf{E}$. Let us first examine the case when ∂C is a wedge of opening angle θ. In this case, $\gamma(w, r)$ is composed by the two sides of the wedge (see Figure 2.2(b)), the potential is given by equation (2.8) and we easily end up with:

$$\phi_r = \int_{\gamma(w,r)} \mathbf{E} \cdot d\mathbf{n} = \int_0^r (\partial_\beta \mathcal{H}|_{\beta=0} - \partial_\beta \mathcal{H}|_{\beta=\theta}) \frac{dr'}{r'} = \frac{\pi}{\theta} \cos\frac{\pi\beta}{\theta}\Big|_{\beta=\theta}^{\beta=0} \frac{r'^{\pi/\theta}}{\pi/\theta}\Big|_0^r = 2r^{\pi/\theta} \tag{2.11}$$

Therefore, in the simple case where a single angle θ is sufficient to characterize the curve, the flux over the wedge scales exactly as the length where we are computing the flux to the power π/θ. This is the well known *point effect* of electrostatics: the electric field generated by a conductor is much higher in the vicinity of a tip. Indeed, for $r \ll 1$ equation (2.11) tells us that $\theta = 2\pi$ i.e., in the presence of a tip, the flux attains its maximum value. On the opposite side, when θ approaches 0, the flux tends to 0 as well.
The flux of the diffusing field (2.6) inside the wedge is therefore:

$$\phi_r = \int_{\gamma(w,r)} \boldsymbol{\nabla}\rho \cdot d\hat{n} = \phi_0 \left(\frac{R}{R_0}\right)^{\pi/\theta} \tag{2.12}$$

where r of (2.10) is replaced by R/R_0. This tells us that the flux of the diffusing field ρ is weak inside deep fjords corresponding to small values of θ. On the other side the flux is much more intense over needle-like capes, corresponding to values of α approaching 2π.

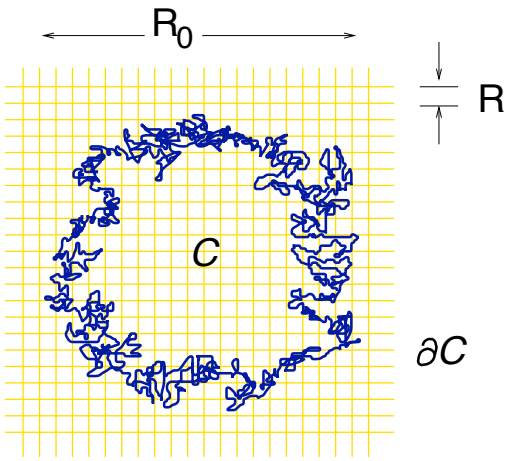

Figure 2.3: Visualization of a square cover of the cluster C.

In the general case, the curve ∂C is not a single wedge, but can be thought of as a superposition of wedges with opening angles $\theta = \pi/\alpha$. The total length of the portion of ∂C characterized by Hölder exponent α – or opening angle π/α – scales as the size of the cluster R_0 to the power $f(\alpha)$. Now let us cover the entire surface with elements (disks, squares) of size $R \ll R_0$ (in figure 2.3 a possible square cover of the region C is visualized). How many of these boxes are characterized by a Hölder exponent α? Since each disk can contribute to the total length of ∂C_α with a fraction $R^{f(\alpha)}$, the number of disks where the Hölder exponent takes this value will be on average $(R_0/R)^{f(\alpha)}$. When we cover the surface with sufficiently small disks, the normalized number of occurrence of this event tends to its probability. This enables us to generalize equation (2.12) in a probabilistic sense by stating that the probability of observing a flux $\phi_0(R/R_0)^\alpha$ is:

$$\begin{aligned} P(\alpha) &\sim (R/R_0)^{-f(\alpha)} \\ f(\alpha) &= \alpha + b\left(1 - \frac{\alpha^2}{2\alpha - 1}\right) \end{aligned} \tag{2.13}$$

This result with the explicit form of $f(\alpha)$ was rigorously proven in [9] by focusing on the moments of the potential averaged over all realizations of C. The constant b was originally expressed as a function of the central charge c in [9] where conformal field theory was used: $b = (25 - c)/12$. We can equivalently express it as a function of the diffusion constant k of SLE by the already mentioned identification: $c = (6 - k)(3k - 8)/(2k)$. Note that the constant k is related to the dimension of the fractal boundary $D = 1 + k/8$ so that after trivial algebra we end up with the expression of b as a function of D:

$$b = \frac{(2D-1)^2}{4(D-1)} \tag{2.14}$$

By a simple change of variables one can obtain the PDF of $\phi = \phi_0(R/R_0)^\alpha$ from equation (2.13):

$$\alpha(\phi) = \log\frac{\phi}{\phi_0}\left(\log\frac{R}{R_0}\right)^{-1}$$
$$P(\phi) = P(\alpha(\phi))\frac{d\alpha}{d\phi} \sim \frac{1}{\phi}\left(\frac{R}{R_0}\right)^{-f(\alpha(\phi))}$$

Beside the exact form of the PDF, it is interesting to consider its expansion for small values of the flux. In this case, $\phi \ll 1 \rightarrow \alpha \gg 1 \rightarrow f(\alpha) \sim (1 - b/2)\alpha$, thus:

$$P(\phi) \sim \phi^{-2+\frac{b}{2}} \tag{2.15}$$

Equation (2.15) is an interesting result based on conformal invariance of the fractal boundary ∂C. As I will show in the next chapter, this holds for rocky shorelines and allows to obtain the strongly intermittent nature of the flux of pollutants toward these real boundaries.

Chapter 3

Diffusion toward rocky coastlines

This chapter is devoted to present the results I have obtained in the framework of diffusion toward rocky shorelines. The results here presented have been collected in the paper at the end of the chapter which is now under revision. The work starts with two observations: *(i)* a consistent portion of shorelines have been observed to be fractal since Mandelbrot [19] and *(ii)* their fractal dimension has been recently explained by means of a simple statistical model, intimately related to critical percolation [24]. These two observations together suggest that the fractal nature of these shorelines may be promoted to conformal invariance. This would allow for substantial advancements in the study of diffusion of a pollutant to these shorelines, relying on what described in chapter 2.

3.1 Conformal invariance of rocky shorelines

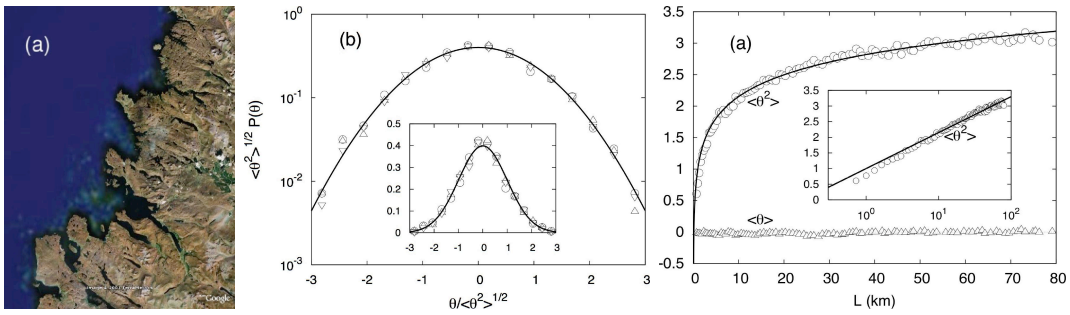

Figure 3.1: Winding angle statistics of real rocky shorelines from the GSHHS database. (a) Portion of the global shoreline (west coast of Britain). This is an example of the 1146 segments of the world shoreline that turned out to be conformally invariant. (b) Winding angle statistics probability distribution. The solid line corresponds to the Gaussian expectation for conformal invariant curves. (c) Mean and variance of the winding angle as a function of the distance L measured on the curve. The solid lines are the expectations for conformal invariant curves: $\langle\theta^2\rangle = 2(D-1)/D \log R$; $\langle\theta\rangle = 0$ (no chirality of the coast).

In the following I present the arguments I developed to support the general picture drawn above. I first analyzed satellite data of real shorelines from a high-resolution database of the world coastlines and identify the portions that could be good candidates for conformal

invariance. It turned out that these are the rocky shorelines, whose fractal dimension is remarkably close to $D = 4/3$. On these polygonal approximations of the real rocky coasts I performed the statistics of the winding angle, which turned out to be Gaussian, with variance in agreement with the SLE expectation for conformal invariant curves (see chapter 1). The result, shown in figure 3.1, allows to conclude that rocky shorelines are indeed conformally invariant curves as discussed in detail in the paper presented below.

In order to corroborate the result I performed direct numerical simulations of a model of rocky coasts erosion adapted from [24]. The model assumes that the erosion mechanism is substantially uncorrelated on distances larger than few hundred meters. The second assumption is that rocks more exposed to the action of sea waves are more apt to be eroded. The intensity of sea erosion can be considered to depend on the length of the coast, to account for the fact that erosion is more effective on a flat line than on a complex fractal. This does not change the fractal properties of the rocky coast. The first assumption allows to divide the domain in discrete squares and to consider each box to evolve independently from the others. Each box is labeled as "land" or "sea" and a random number is assigned to each land site representing the local resistance of the rocks to sea erosion, which depends on the specific lithology. Each land site resistance is compared with the average excitation power of the waves which represents the intensity of erosion. If a land site is weaker than the erosive power, then it is eroded and its label changes from land to sea. In turn, the erosion power can be updated accounting for depletion by the growing length of the coastline. When the coastline is complex enough, erosion is no more effective. This is the stationary state. Then one should consider that the slow weathering processes alter and weaken the rock, so that after a while the dynamics can begin again. Of course, with these two general assumptions, one can exhibit a number of different set of rules to model the erosion power, but it turns out that the qualitative behavior is quite robust with respect to this particular choice. Details on the model adapted from [24] can be found in the paper below. Starting from a flat interface between land and sea, the described dynamics spontaneously produces fractal shorelines. From these steady states I collected an ensemble of artificial shorelines whose winding angle statistics turn out to be consistent with the hypothesis of conformal invariance. The statistical analysis of both real coastlines and synthetic coastlines obtained by this simple model of erosion points to conformal invariance.

Note that the algorithm to decide if a certain site is "land" or "sea" strongly reminds of percolation, where each site is colored dark or bright according to a given constant probability. This is further sustained by the fact that $D = 4/3$ is exactly the fractal dimension of the external boundaries of critical percolation. The only ingredient which marks a difference between the two is that the erosion process may be influenced by the geometry of the rocky coast. This simply moves our problem from random percolation to gradient percolation, where sites are colored with a probability that varies linearly from 0 to 1 along one fixed direction in space. However, the qualitative mechanism leading to the self-stabilization of the dynamics does not rely on this further ingredient and the global feedback of rocky shoreline geometry does not change the fractal dimension of the final steady state (see [24] for a detailed discussion).

3.2 Diffusion over rocky shorelines

Given the conformal invariant nature of rocky coastlines, how does a pollutant emitted from a source far away from the coast diffuse toward the coast itself? Conformal invariance allows to apply the results of potential theory reviewed in chapter 2. I relied on the theoretical results for the flux of pollutant in the vicinity of the rockycoast. In particular it is interesting to consider the expansion of the PDF of the flux ϕ at small values described in section 2.3. I could compare the expectation (2.15) with the results obtained by the following procedure. I performed a conformal transformation so to reduce the domain to a simple geometry, where it is easy to solve the Laplace equation. Then I went back to the original space and displayed the flux of pollutant near the coast. I finally evaluated the PDF of the flux and compared it with the theoretical prediction $\phi^{-2+b/2}$, $b = (2D-1)^2/[4(D-1)]$ and $D = 4/2$. As shown in figure 3.2, the comparison confirms consistency with conformal invariance and provides a spatially intermittent distribution of the flux over the rocky coast. Note that ntermittency has been already observed for real pollutant dispersion [21].

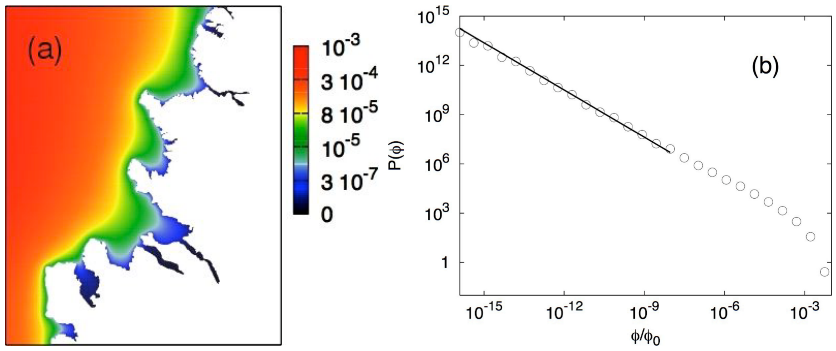

Figure 3.2: (a) Visualization of the flux of pollutant over the rocky shoreline shown in figure 3.1. (b) PDF of the flux in the vicinity of the rocky coast. The solid line $\phi^{-2+b/2}$, $b = (2D-1)^2/[4(D-1)]$ is the theoretical expectation for $\phi \ll 1$ based on conformal invariance of the coast (see equations (2.14) and (2.15)).

Diffusion is of course only one aspect of the dynamics of the real problem of pollutant dispersion. However one can expect that in some cases an effective diffusion can dominate on the transport mechanisms at work on a particular portion of the coast, at least if the focus is on large enough spatial scales. A further interesting development could be to evaluate the real situations where this picture can be applied. In particular, I am interested to study the realistic morphological structure of rocky coasts with a local feedback of the coastline properties on the erosive process. Note that the results above described are valid for the case where the geometry of the coastline back reacts on the erosion power at global level. On the basis of this picture, one is able to perform predictions on the distribution of pollutant and to ideally devise artificial structures to modify it. Finally, the erosion process is not an exclusive feature of rocky coasts and there could be other geophysical systems where advancements could be achieved with the powerful ingredient of conformal invariance.

GEOPHYSICAL RESEARCH LETTERS, VOL. ???, XXXX, DOI:10.1029/,

How winding is the coast of Britain ? Conformal invariance of rocky shorelines

G. Boffetta,[1,3] A. Celani,[2,3] D. Dezzani,[1] and A. Seminara[2,4]

We show that rocky shorelines with fractal dimension 4/3 are conformally invariant curves by measuring the statistics of their winding angles from global high-resolution data. Such coastlines are thus statistically equivalent to the outer boundary of the random walk and of percolation clusters. A simple model of coastal erosion gives an explanation for these results. Conformal invariance allows also to predict the highly intermittent spatial distribution of the flux of pollutant diffusing ashore.

1. Introduction

Forty years after Mandelbrot's seminal paper [*Mandelbrot*, 1967] where the concept of fractional dimension was introduced, there is a compelling evidence of the fractal nature of many geographical phenomena, including the shaping of shorelines [*Goodchild and Mark*, 1987]. Statistically self-similar curves are characterized by their fractal exponent D. If we select two points on the curve and measure their distance L along the curve (e.g. by walking a divider of given width) on average this will be proportional to their Euclidean distance R to the power D, i.e. $L \sim R^D$, where D can take values between 1 and 2. Such curves are widespread in nature, and often enjoy a much richer symmetry than mere global scale invariance. This is the case of conformally invariant curves, whose statistics is covariant with respect to local scale transformations. These are defined as the coordinate changes that preserve the relative angle between two infinitesimal segments. In spite of their seemingly exotic character, conformal transformations are known since the sixteenth century because of their cartographical applications (e.g. Mercator's map). Conformal invariance is a pervasive feature of two-dimensional physics, from string theory and quantum gravity to the statistical mechanics of condensed matter and fluid turbulence [*Polyakov*, 1970; *Belavin et al.*, 1984; *Schramm*, 2006; *Bernard et al.*, 2006, 2007]. A remarkable consequence of conformal invariance is the high degree of symmetry that often allows to make substantial analytical progress. Several statistical indicators can be exactly computed by means of different techniques of theoretical physics [*Cardy*, 2005; *Bauer and Bernard*, 2006]. Among the many characteristic features that make conformally invariant curves peculiar within the class of self-similar ones, the former are also distinguished by the special statistics of the winding angle about a point belonging to the curve itself (see Fig. 1b). The probability distribution of the winding angle is Gaussian, and therefore specified only by its mean (that is zero, i.e. curves do not have a preferred winding direction, or chirality), and its variance, that increases proportionally to the logarithm of the distance from the reference point with a proportionality constant which depends on the fractal dimension. This provides a simple and useful diagnostics for conformal invariance of curves extracted from experimental or numerical data.

Here we analyze the statistics of rocky shorelines, selected on the basis of a fractal dimension $D \simeq 4/3$ from the global, high-resolution, GSHHS database [*Wessel and Smith*, 1996]. These shorelines are found to display a Gaussian statistics of the winding angle with the exact logarithmic dependence of the variance from the length and the correct numerical prefactor $2(D-1)/D$ expected for conformally invariant curves (see Fig. 2). We also illustrate how conformal invariance allows to predict the statistics of the flux of pollutant arising from, e.g., oil spills or the discharge of toxins and pathogens with ballast water. A peculiar characteristic of pollutant diffusion to shorelines is the markedly intermittent spatial distribution of the flux. This can vary dramatically between locations just a few hundred meters apart (see for instance Fig. 1 of *Peterson et al.* [2003] about the Exxon-Valdez oil spill). These wild fluctuations are the quite suprising result of the "marriage" of two tame partners such as diffusion and self-similarity of shoreline profile. Conformal invariance allows to solve analytically the problem of computing the statistics of pollutant flux (see Fig. 4) and to link its local intensity to the local geographical properties of the shoreline [*Duplantier*, 2004].

2. Statistical analysis of rocky shoreline

Since the famous paper of *Mandelbrot* [1967], the west coast of Britain has become the paradigmatical example of fractal shoreline. In Figure 1 we show a satellite image of a portion of the western coast of Scotland along with its digitized shoreline, that is a polygonal approximation to the real coastline. It is also displayed in a double logarithmic plot the fraction of pairs of vertices of the polygon that lie within a ball of diameter R: the slope of this curve is the correlation dimension [*Grassberger and Procaccia*, 1983], that is very close to 4/3 in this case. (Notice that Mandelbrot quotes the value 1.25 for the fractal dimension of the west coast of Britain, an estimate obtained from a fit of *Richardson* [1961] data over the range from 1 to 1000 kilometers. However, if the same data are fitted over the range from 1 to 300 kilometers one obtains a value for D very close to 4/3.)

[1]Dipartimento di Fisica Generale and INFN, Università degli Studi di Torino, Italy.
[2]CNRS INLN, Valbonne, France.
[3]ISAC Sezione di Torino, Italy.
[4]Dipartimento di Fisica and INFN, Università degli Studi di Genova, Italy.

0094-8276/07/$5.00

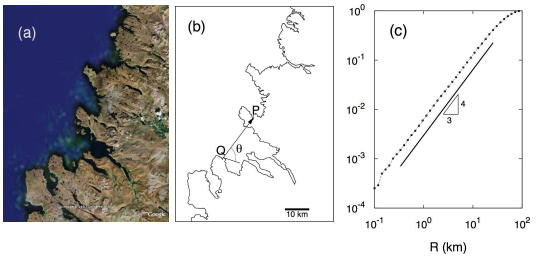

Figure 1. The west coast of Scotland: an example of the 1146 shorelines that have been searched for conformal invariance. Panel (a) shows the satellite image of the geographical area, centered around the point 58°05′N, 5°21′W. In Panel (b) is shown the GSHHS polygonal approximation of the shoreline with resolution $\approx 200\ m$ together with an example of winding angle between points Q and P. Panel (c) shows the fraction of pairs of points of the curve (b) lying at a distance smaller than R. The logarithmic slope of the curve is the fractal correlation dimension. A least-squares fit for the data over the range from 300 m to 20 km gives an exponent 1.30 ± 0.04. Also shown for comparison a straight line of slope 4/3.

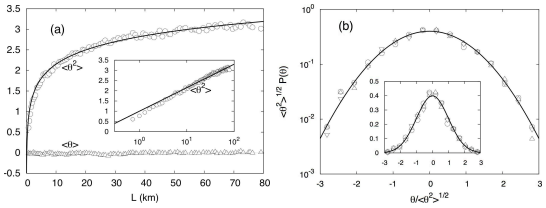

Figure 2. Winding angle statistics. Panel (a) shows the mean and the variance of the winding angle as a function of the length of the shoreline between points P and Q. (see Fig. 1). The line is the law $\langle \theta^2 \rangle = a + \frac{2(D-1)}{D} \ln L$ with $D = 4/3$ and $a = 0.98$. In the inset, the variance in semilogarithmic coordinates. In panel (b) is shown the probability density function of the winding angle at lengths $L = 5, 10, 20\ km$ rescaled by the respective standard deviation and compared to the standard Gaussian density, in semilogarithmic (main frame) and in linear coordinates (inset).

The shoreline shown in Fig. 1 is one example of the curves extracted from the high-resolution, self-consistent GSHHS database. The complete database covers the world shoreline which has been partitioned into 11503 segments of length $\approx 200\ km$ with a resolution of about 200 m. The computation of fractal dimension (as in Fig. 1) for each segment, gives different values of D that depend on the geomorphologicae processes at work in that particular geographical area. We observe a fractal dimension close to 1 for sedimentary shores while for for rocky coasts it is about 1.3 or larger. The overall most probable value is found to be $D \simeq 1.2$. Within this large sample, we have selected the 1146 shorelines which present a correlation dimension close to $D = 4/3$ (with a tolerance of 5%). The capacity dimension for such curves, computed by a box-counting algorithm, yields a value consistent with the correlation dimension, pointing to the conclusion that these are truly fractal curves and not multifractals [*Grassberger and Procaccia*, 1983].

The statistics of winding angles for rocky coaslines is shown in Fig. 2. The winding angle θ is defined as the angle between the line joining two points separated by a lenght L along the curve (defined by means of its polygonal approximation) and the local tangent in the reference point (i.e. the direction of the side of the polygon adjacent to the point), measured counterclockwise in *rad* (see Fig. 1b). Because our curves do not have a preferred direction, the mean winding angle $\langle \theta \rangle$ is very close to zero while the variance is found to grow with L according to the logarithmic law predicted for conformal invariant curves [*Duplantier and Saleur*, 1988; *Duplantier and Binder*, 2002; *Wieland and Wilson*, 2003]

$$\langle \theta^2 \rangle = a + \frac{2(D-1)}{D} \ln L \qquad (1)$$

Here $a \simeq 0.98$ is an additive constant that depends on the details of the definitions (including the curve resolution, or the width of the divider used to compute the length) and whose actual value is thus irrelevant. The numerical evalutation of the coefficient in (1) gives $D \simeq 1.33 \pm ???$, i.e. very close to the direct measure of D. Figure 2b shows that the probability density function (pdf) of θ is very close to a Gaussian distribution for different separations in the logarithmic range. Winding angle statistics have been computed using different reference points located along the curve: we have found no detectable dependence on this choice.

Values of the fractional dimension other than 4/3 (e.g. $D = 1.2$ and $D = 1.5$) fail to give such an impressive agreement with the prediction for conformally invariant curves, in the sense that the prefactor differs significantly from the value predicted by (1). The reason for this special value of D can be understood by means of a simple model, introduced by *Sapoval et al.* [2004], of mechanical erosion of rocky coasts by the action of marine waves. The basic ingredients of this model are two: *(i)* the mechanical resistance of rocks to erosive processes, essentially determined by their structure, composition and by the slow corrosion process due to chemical agents, is assumed to have a typical scale of variation of the order of hundreds of meters and to be essentially uncorrelated on larger distances; *(ii)* rocks that are more exposed to the action of waves have a larger propensity to be fragmented by mechanical erosion: for instance, an isthmus will be eroded more rapidly than the shoreline within a gulf.

This model can be implemented on a two-dimensional lattice where the sites represent regions of land or sea of dimensions about a hundred meters. In the initial state, the land takes the form of a circular island surrounded by the sea. To every point on the land is assigned a number that measures the resistance of the rock to erosion. Then, if the resistance of a land site adjacent to the sea falls below a given threshold, it will be eroded, and thus transform into a sea site. Subsequently, the resistance values for land sites along the shoreline are updated depending on the local conformation of the coast. For example, the value of the resistance parameter is decreased if a land site is flanked by two sea sites and falls to zero for sites surrounded by three or more sites [*Sapoval et al.*, 2004]. Other qualitatively similar choices give the same final statistics. This procedure is iterated until no further updates are necessary and a stationary artificial shoreline is obtained (see Fig. 3a). The similarities of this model with the well-known problem of percolation [*Stauffer and Aharony*, 1991] are evident, as already pointed out in *Sapoval et al.* [2004]. Indeed, in presence of rule *(i)* alone the islands generated by the algorithm would be statistically equivalent to percolation clusters — except for the

inner "lakes" present in the latter case — and thus display a fractal dimension 7/4. However, rule *(ii)* prevents the formation of deep gulfs and peninsulae with narrow isthmi, therefore reducing the shoreline to the outer boundary of percolation clusters that is known to have fractal dimension 4/3 [*Grossman and Aharony*, 1986; *Saleur and Duplantier*, 1987]. Further refinements of the model, including damping of sea-waves and slow erosive processes do not modify the main features described above. As a consequence of the statistical equivalence between the artificial shoreline and the external frontier of percolation clusters, the former inherits the known conformal invariance of the latter. In Figure 3 we show the numerical results for the artificial shorelines generated by the model, which confirm the theoretical expectations.

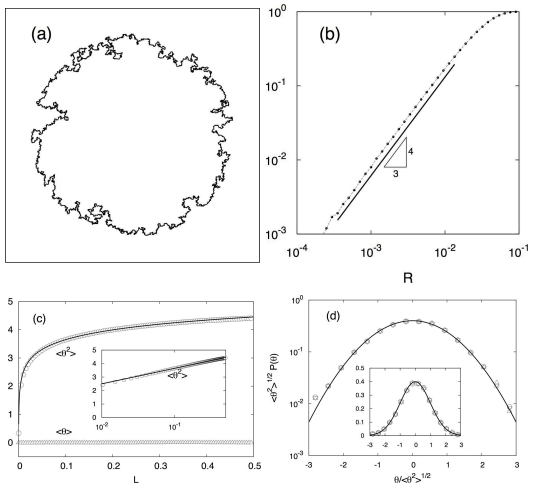

Figure 3. Artificial shorelines. In panel (a) one example of a coast generated by the model of wave erosion described in the text. The simulation has been done on a square grid with 8000^2 collocation points. The number of realizations is 800. Panel (b) shows the correlation dimension. The unit for R and L is the simulation box size. A fit in the range of R between $5 \cdot 10^{-4}$ and 0.1 yields $D = 1.32 \pm 0.02$. Panels (c) and (d) show the winding angle statistics as in Fig. 2 compared to the theoretical expectations.

3. Intermittency of diffusing pollutants

By virtue of the rich symmetry underlying conformal invariance, many interesting results can be obtained analytically. As a remarkable example we consider here the evaluation of the flux of pollutant diffusing ashore from a source located in the sea. Transport and mixing of tracers is a complex issue of paramount importance from microscopic to planetary scales [*Ottino*, 1989]. At the simplest level of description dispersion is modeled as pure diffusion. In the present case, this may be justified by estimates of the horizontal eddy-diffusivity in the ocean that yield a ratio about 0.1 to 1 between mean currents and velocity fluctuations over scales of a hundred kilometers [*Marshall et al.*, 2006].

Pollutant concentration c is therefore assumed to be given by the solution of the Laplace equation $\Delta c = 0$ with absorbing boundary conditions on the coastline ($c = 0$) and a pointwise source in the ocean. This problem can be solved with the aid of conformal transformations by mapping the region of interest (i.e. a region of sea bounded by the shoreline) into an infinite strip, solving the Laplace problem in the new domain (now a trivial task), and mapping the solution back to the initial region. The conformal transformation is done partly numerically, from the given domain to a unit disk, and partly analytically by mapping the unit disk onto the infinite strip.

The upshot of the conformally invariant nature of the shoreline is that techniques borrowed from theoretical physics enable to compute analytically the pollutant flux distribution $\phi = \partial c/\partial n$ at the boundary [*Duplantier*, 2000; *Duplantier and Binder*, 2002; *Bettelheim et al.*, 2005]. The main result is that the probability of observing a flux ϕ of intensity $\phi_0(R/R_0)^\alpha$ — where ϕ_0 is the rate of emission by the source, R the size of the region where the flux is computed, and R_0 the distance of the source from the coast — is proportional to $(R/R_0)^{-f(\alpha)}$ with $f(\alpha) = \alpha + \frac{(2D-1)^2}{4(D-1)}\left[1 - \alpha^2/(2\alpha-1)\right]$, for $R \ll R_0$. Small values of the flux correspond to large values of α, whereas the largest ones take place for $\alpha \searrow 1/2$. This can be understood by means of the geometrical interpretation of the variable α [*Duplantier*, 2000]. Indeed, let us recall that the flux inside a wedge of opening angle θ scales exactly as $R^{\pi/\theta}$. The result above can thus be interpreted as if the shoreline was made of a random collection of wedges or size $\sim R$ and opening angles θ with probability $\sim R^{-f(\pi/\theta)}$. Large α and small fluxes are equivalent to small θ, i.e. deep fjords in the shoreline. On the opposite, as α reaches the minimum value 1/2, the flux attains its maximum value $\sim \phi_0(R/R_0)^{1/2}$ corresponding to $\theta = 2\pi$, that is a needle-like cape. The average flux $\langle\phi\rangle$ is exactly ϕ_0. By means of a variable change from α to ϕ it is possible to derive the exact probability density for the flux. Besides the exact form, it is interesting to notice that for $\phi \ll \phi_0$ the probability of observing a value ϕ of the flux scales as a power law:

$$p(\phi) \sim \phi^{-2+\frac{(2D-1)^2}{8(D-1)}} \tag{2}$$

This power-law dependence is a reflection of the strongly intermittent character of flux fluctuations. In Figure 4 we show the flux of pollutant emitted for a source located 40 km offshore the coastline of Fig 1, together with its probability density. This closely follows the theoretical predictions for small fluxes over a range of several decades.

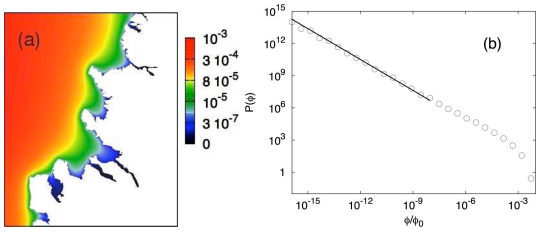

Figure 4. Flux of diffusing pollutant. In panel (a) is shown the contour plot of the pollutant concentration in the domain bounded by the shoreline of Fig. 1. Panel (b) shows the probability density of flux computed along the present shoreline, compared with the theoretical expectation (2) for the left tail.

In conclusion, we have demonstrated that world coastlines with dimension $D \simeq 4/3$ are conformally invariant curves by

measuring their winding angle statistics. The distinguishing feature of such random curves is their high degree of symmetry which enables to compute analytically many statistical properties. We have focused our attention on the flux of pollutant diffusing toward the shoreline, however many other interesting results could be relevant to geophysical applications. For instance, an archipelago of conformally invariant islands (loops) would display a power law distribution A^{-1} of the number of islands of area larger than A with a known prefactor. These would be also characterized by a ratio between the average area and the average squared radius equal to $\pi D/(2D-1)$. All these properties, and many others, are also shared by self-avoiding walks (polygons), i.e. closed random walks that never hit themelves. These have been conjectured to be conformally invariant curves with dimension 4/3 *via* the equivalence with stochastic Loewner evolution curves $\mathrm{SLE}_{8/3}$ (see *Lawler et al.* [2004] for a review). Remarkably enough, self-avoiding walks were introduced by Mandelbrot as well, when he conjectured the (now proven) equivalence between them and the external frontier of two-dimensional Brownian motion. Today, in view of our results, all these curves reveal their unexpected and intimate connection with the brilliant intuition by Richardson and Mandelbrot about the fractal nature of world coastlines.

Acknowledgments. This work has been supported by COFIN 2005 Project No. 2005027808.

References

Bauer, M., and D. Bernard (2006), 2D growth processes: SLE and Loewner chains, *Phys. Rep.*, *432*, 115.

Belavin, A.A., A.M. Polyakov, and A.A. Zamolodchikov (1985), Conformal field theory, *Nucl. Phys. B*, *241*, 333.

Bernard, D., G. Boffetta, A. Celani, and G. Falkovich (2006), Conformal invariance in two-dimensional turbulence, *Nature Physics*, *2*, 124.

Bernard, D., G. Boffetta, A. Celani, and G. Falkovich, Inverse turbulent cascades and conformally invariant curves, *Phys. Rev. Lett.*, *98*, 024501.

Bettelheim, E., I. Rushkin, I.A. Gruzberg, and P. Wiegmann (2005), Harmonic Measure of Critical Curves, *Phys. Rev. Lett.*, *95*, 170602.

Cardy, J. (2005), SLE for theoretical physicists, *Ann. Phys.*, *318*, 81.

Duplantier, B. (2000), Conformally Invariant Fractals and Potential Theory, *Phys. Rev. Lett.*, *84*, 1363.

Duplantier, B. (2004), Conformal fractal geometry & boundary quantum gravity, *Proc. Symposia Pure Math.*, *72*, 365. See also arXiv:math-ph/0303034

Duplantier, B., and I. A. Binder (2002), Harmonic Measure and Winding of Conformally Invariant Curves, *Phys. Rev. Lett.*, *89*, 264101.

Duplantier, B., and H. Saleur (1988), Winding-Angle Distributions of Two-Dimensional Self-Avoiding Walks from Conformal Invariance, *Phys. Rev. Lett.*, *60*, 2343.

Goodchild, M.F., and D.M. Mark (1987), The fractal nature of geographic phenomena, *Annals of the Association of American Geographers*, *77*, 265.

Grassberger, P., and I. Procaccia (1983), Measuring the strangeness of strange attractors, *Physica D*, *9*, 189.

Grossman, T., and A. Aharony (1986), Structure and perimeters of percolation clusters, *J. Phys. A*, *19*, L745.

Lawler, G.F., O. Schramm, and W. Werner (2004), On the scaling limit of planar self-avoiding walk, *Proc. Sympos. Pure Math.*, *72*, 339.

Mandelbrot, B. (1967), How long is the coast of Britain ? Statistical self-similarity and fractional dimension, *Science*, *156*, 636.

Marshall, J., E. Shuckburgh, H. Jones, and C. Hill (2006), Estimates and Implications of Surface Eddy Diffusivity in the Southern Ocean Derived from Tracer Transport, *J. Phys. Oceanog.*, *36*, 1806.

Ottino, J.M. (1989), *The kinematics of mixing: stretching, chaos, and transport*, Cambridge University Press.

Peterson, C.H. *et al* (2003), Long-Term Ecosystem Response to the Exxon Valdez Oil Spill, *Science*, *302*, 2082.

Polyakov, A.M. (1970), Conformal symmetry of critical fluctuations, *JETP Lett.*, *12*, 381.

Richardson, L.F. (1961), The Problem of Contiguity: An Appendix to Statistics of Deadly Quarrels, *General Systems Yearbook*, *6*, 139.

Saleur, H., and B. Duplantier (1987), Exact Determination of the Percolation Hull Exponent in Two Dimensions, *Phys. Rev. Lett.*, *58*, 2325.

Sapoval, B., A. Baldassarri, and A. Gabrielli (2004), Self-Stabilized Fractality of Seacoasts through Damped Erosion *Phys. Rev. Lett.*, *93*, 098501.

Schramm, O. (2006), Conformally invariant scaling limits (an overview and a collection of problems), *math.PR/0602151*.

Stauffer, D., and A. Aharony (1991), *Introduction to Percolation Theory* Taylor and Francis, London.

Wessel, P., and W.H.F. Smith, (1996), A Global Self-consistent, Hierarchical, High-resolution Shoreline Database, *J. Geophys. Res.*, *101*, B4, 8741.

Wieland, B., and D. B. Wilson (2003), Winding angle variance of Fortuin-Kasteleyn contours, *Phys. Rev. E*, *68*, 056101.

G. Boffetta, Dipartimento di Fisica Generale and INFN, Università degli Studi di Torino, via Giuria 1, 10125 Torino, Italy

A. Celani, CNRS INLN, 1361 Route des Lucioles, 06560 Valbonne, France

D. Dezzani, Dipartimento di Fisica Generale and INFN, Università degli Studi di Torino, via P.Giuria 1, 10125 Torino, Italy

A. Seminara, Dipartimento di Fisica and INFN, Università degli Studi di Genova, V. Dodecaneso 33, 16146 Genova, Italy.

Bibliography

[1] M. BAUER and D. BERNARD. Sle growth processes and conformal field theories. *Phys. Lett B*, **543** 135-138, (2002).

[2] M. BAUER and D. BERNARD. Conformal field theories of stochastic löwner evolutions. *Comm. Math. Phys.*, **239** 493-521, (2003).

[3] M. BAUER and D. BERNARD. 2d growth processes: Sle and loewner chains. *Phys. Rep.*, **432** 115-221, (2006).

[4] A. BELAVIN, A. POLYAKOV and A. ZAMOLODCHIKOV. Infinite conformal symmetry in two-dimensional quantum field theory. *Nucl. Phys.*, **241** 333-380, (1984).

[5] D. BERNARD, A. CELANI, K. GAWEDZKI and G. FALKOVICH. Conformal invariance in two-dimensional turbulence. *Nature*, **2** 124-128, (2006).

[6] X. BOSCH. Spain's prestige oil spill resurfaces. *Science*, **314** 1861, (2006).

[7] J. CARDY. Critical percolation in finite geometry. *J. Phys.*, **A25** 201-206, (1992).

[8] J. CARDY. Sle for theoretical physicists. *Annals. Phys.*, **318** 81-118, (2005).

[9] B. DUPLANTIER. Conformally invariant fractals and potential theory. *Phys. Rev. Lett.*, **84** 1363-1367, (2000).

[10] B. DUPLANTIER and A. BINDER I. Harmonic measure and winding of conformally invariant curves. *Phys. Rev. Lett.*, **89** 264101, (2002).

[11] B. DUPLANTIER and H. SALEUR. Winding-angle of two-dimensional self-avoiding walks from conformal invariance. *Phys. Rev. Lett.*, **60** 2343-2346, (1988).

[12] W. KAGER and B. NIENHUIS. A guide to stochastic-loewner evolution and its applications. *J. Stat. Phys.*, **115** 1149-1229, (2004).

[13] G. F. LAWLER. *Intersections of random walks*. Birkhauser, Boston MA, (1991).

[14] G. F. LAWLER. Conformally invariant processes in the plane. *Math. Surveys Monogr.*, **114** 1-242, (2005).

[15] G. F. LAWLER, O. SCHRAMM and W. WERNER. Values of brownian intersection exponents i: Half-plane exponents. *Acta. Math.*, **187** 237-273, (2001).

[16] G. F. LAWLER, O. SCHRAMM and W. WERNER. Values of brownian intersection exponents ii: Plane exponents. *Acta. Math.*, **187** 275-308, (2001).

[17] G. F. LAWLER, O. SCHRAMM and W. WERNER. Conformal invariance of planar loop-erased random walks and uniform spanning trees. *Ann. Probab.*, **32** 939-995, (2004).

[18] K. LOEWNER. Untersuchungen über schlichte konforme abbildungen des einheitskreises. *Math. Ann.*, **89** 103-121, (1923).

[19] B. MANDELBROT. How long is the coast of britain? statistical self-similarity and fractional dimension. *Science*, **156** 636-638, (1967).

[20] B. NIENHUIS. Critical behavior of two-dimensional spin models and charge asymmetry in the coulomb gas. *J. Stat. Phys.*, **34** 731-761, (1983).

[21] C. H. PETERSON, S. D. RICE, J. W. SHORT, D. ESLER, J. L. BODKIN, B. E. BALLACHEY and D. B. IRONS. Long-term ecosystem response to the exxon valdez oil spill. *Science*, **302** 2082-2086, (2003).

[22] L. RICHARDSON. The problem of contiguity: an appendix of statistics of deadly quarrels. *General Systems Yearbook*, **6** 139-187, (1961).

[23] S. ROHDE and O. SCHRAMM. Basic properties of sle. *Ann. of Math.*, **161** 879-920, (2005).

[24] B. SAPOVAL, A. BALDASSARRI and A. GABRIELLI. Self-stabilised fractality of seacoasts through damped erosion. *Phys. Rev. Lett.*, **93** 098501, (2004).

[25] O. SCHRAMM. Scaling limits of loop-erased random walks and uniform spanning trees. *Israel J. Math*, **118** 221-288, (2000).

[26] S. SMIRNOV. Critical percolation in the plane: conformal invariance, cardy's formula, scaling limits. *C. R. Acad. Sci. Paris*, **333** 239-244, (2001).

[27] W. WERNER. Random planar curves and schramm-loewner evolutions. *Springer Lecture Notes in Mathematics*, **1840** 107-195, (2004).

[28] B. WIELAND and D. B. WILSON. Winding angle of fortuin-kasteleyn contours. *Phys. Rev. E*, **68** 056101, (2003).

[29] K. G. WILSON. Renormalization group and critical phenomena. *Rev. Mod. Phys.*, **55** 583-600, (1983).

Part II

The large-scale statistics of passive scalar transport

Introduction

The statistical properties of systems in thermal equilibrium are fully characterized by the knowledge of the integrals of motion. A prominent example is represented by the well-known Gibbs ensemble, where the partition function determined by the free energy allows to compute the probability of occurrence of each given state of the system. Turbulence is the paradigm of systems with many interacting degrees of freedom, strongly out of equilibrium. Here the integrals of motion are unsufficient to describe the statistics, as they cannot capture the distinctive features of turbulence: intermittency and anomalous scaling. Instead, these have been brilliantly traced back to *statistical* integrals of motion whose nature strongly differs from the dynamical integrals of motion of equilibrium systems [18]. Anomalous scaling in turbulence is observed in correspondence of a flux of the conserved quantities through the whole *inertial* range of scales showing the non-equilibrium nature of the process. In most cases, no upscale flux is present and the above picture does not apply to scales larger than the injection scale. Here, the statistics is expected to recover thermal equilibrium. Surprisingly enough, this is not true in the general case.
The problem is essentially related to the following question: how does information propagate toward large scales? Applications of this general question span the most diverse fields of physics. The large-scale structure of the universe originates from an ancient event that concerned a tiny volume. The propagation of seismic waves on earth seems to depend on the microscopic structure of crystals in mantle rocks. Hence the general physical interest to understand the large-scale statistics of a field which is generated at much smaller scales. In this part of the thesis I focus on a *passive scalar* field and demonstrate that the large-scale structure of passive scalar turbulence definitely deviates from the expected Gibbs equilibrium. This points to the propagation of small-scales properties toward large-scales.
What is a passive scalar and what are the particular properties that make it interesting?

Figure 3: Instances of real scalar turbulence.

A passive scalar is a quantity that is advected by a flow without back-reacting on it. There is

a variety of real transport problems (see figure 3 for instance) that can be described through the passive scalar scheme. This happens every time the reaction of some particular quantity on the carrying flow can be disregarded, like for dilute dyes, pollutants dispersed in a fluid or temperature in the case where buoyancy forces are negligible.

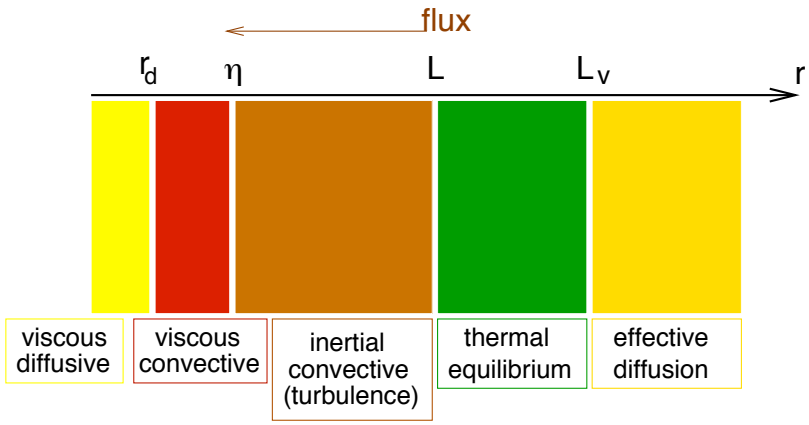

Figure 4: Sketch of the different spatial scales in turbulence. The inertial-convective range, traditionally-studied in turbulence, is indicated in brown. I focus on large-scales instead, marked in Green with label "thermal equilibrium".

Passive scalar transport extends the diffusion problem treated in the first part of the thesis, as its dynamics includes advection. Mathematically this corresponds to the addition of the product term $\mathbf{v} \cdot \boldsymbol{\nabla}\theta$ in the evolution equation for the scalar field. This term, in the presence of an incompressible velocity field, provides a small-scale cascade process that does not modify the input-output balance between injection and dissipation, but only transfers scalar fluctuations from large scales to small scales. In order to visualize the turbulent cascade, one can imagine the scalar organized in eddies of different sizes. The largest eddy in the problem is determined by the mechanism of scalar injection, whose typical lenght scale is here indicated with L. Due to advection, the large eddies introduced by the forcing split into smaller eddies that are further broken and so forth. This cascade process finally ends up with tiny eddies that are eventually smeared out by diffusion. The interval between the injection and the diffusive scales (*convective range*) has been long studied. Together with the cascade, a peculiar phenomenology appears in the convective range with a breakdown of scale-invariance [20, 34, 37, 38, 40]. The statistical properties of the scalar at a certain length scale cannot be obtained by a simple rescaling of the statistics at another scale. This manifests itself in the presence of a quasi-discontinuous spatial structure for the scalar field [11, 24, 30]. In other words, the probability of dramatic fluctuations of the scalar between two points increases as the two points approach with one another.
The Navier-Stokes equations for the velocity field, in the limit of large scale separation between injection (L_v) and dissipation (η), provide a very similar cascade process. This observation strongly suggested that research could obtain information on Navier-Stokes turbulence by studying the simpler problem of passive scalar transport. A great advancement in this sense was achieved with the introduction of the Kraichnan model of passive advec-

tion [29]. The key point of passive scalar success is the observation that its intermittency is much more pronounced than the intermittency of the velocity field. This hints to the possibility that the scalar field could be intermittent in the absence of any intermittency of the carrier flow. Kraichnan model studies the evolution of a passive scalar advected by an incompressible, Gaussian, scale-invariant, white-in-time, stochastic flow. This particular choice allows for a thorough analytical analysis of the model. The result is that despite the absence of any intermittency of the carrier flow, this problem displays scalar intermittency. Most importantly, it traces intermittency back to the presence of statistical integrals of motion that can be found as zero modes of partial differential operators [3, 14–16, 23].

All these ideas concern the turbulent cascade process developing at scales smaller than the injection scale. What about the scalar-field structures above the injection scale? Figure 4 shows a sketch of the spatial scales interested by different mechanisms in turbulence. The inertial-convective scales, traditionally studied, are represented in brown while I focus here on the "thermal equilibrium" range, colored in green. Note that no upscale flux of scalar fluctuations is provided by incompressible turbulent transport. Therefore the large-scale scalar statistics is supposed to display Gibbs equilibrium. However, since we focus on scales larger than L yet smaller than L_v, the underlying velocity field is turbulent. I investigated the problem both analytically for the Kraichnan model ensemble and by direct numerical simulations of realistic flows. The picture that emerges points to the presence of long-range correlations, due to the existence of large-scale zero modes. This "memory" of the fine-scale structure in passive scalar transport provides a transfer of information from small scales toward large scales. In the case of anisotropic scalar injection, this effect is even more dramatic than in the isotropic case. Under very broad conditions, a small amount of anisotropy introduced at small scales is propagated toward large scales where it eventually dominates the structure of the concentration field.

In chapter 1 I review some background concepts related to anomalous scaling and intermittency and recall the main results of the Kraichnan model for passive advection in the inertial-convective range of scales. In chapter 2 I switch to the thermal-equilibrium range and describe the results I obtained for the large-scale structure of passive scalar turbulence. These have been collected and published in the papers presented in chapter 2.

Chapter 1

The Kraichnan model of passive advection

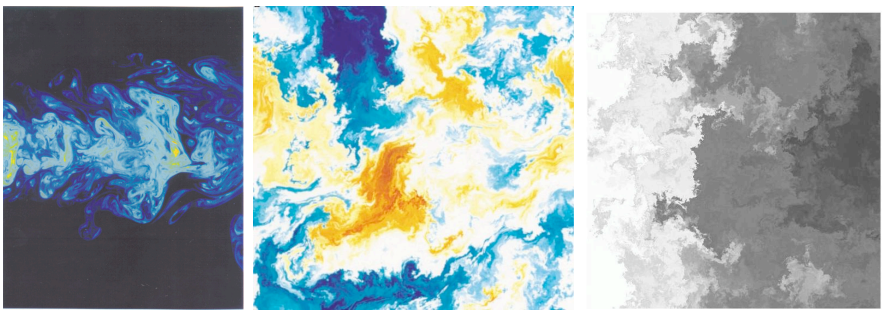

(a) (b) (c)

Figure 1.1: Instances of scalar snapshots obtained by experiments of a fluorescent dye in a turbulent jet [37] (a) and by DNS: in figure (b) the scalar is advected by a Kraichnan velocity field [13] and in figure (c) by two-dimensional Navier-Stokes turbulence in the inverse cascade regime [11]. The spatial structure of scalar turbulence is intermittent.

A passive scalar field θ is a quantity that is transported by a flow, but does not back-react on it. There is a variety of real problems where the feedback of a transported quantity is negligible and the evolution can be thus described by passive advection (e.g. the dispersion of a pollutant or of a dye dilute in the atmosphere or in the ocean [32]).

1.1 Passive scalar transport

Passive scalar transport by a turbulent incompressible carrier flow $\mathbf{v}$ is ruled by the well-known advection-diffusion equation:

$$\partial_t \theta + \mathbf{v} \cdot \boldsymbol{\nabla} \theta = \kappa \Delta \theta + f \tag{1.1}$$

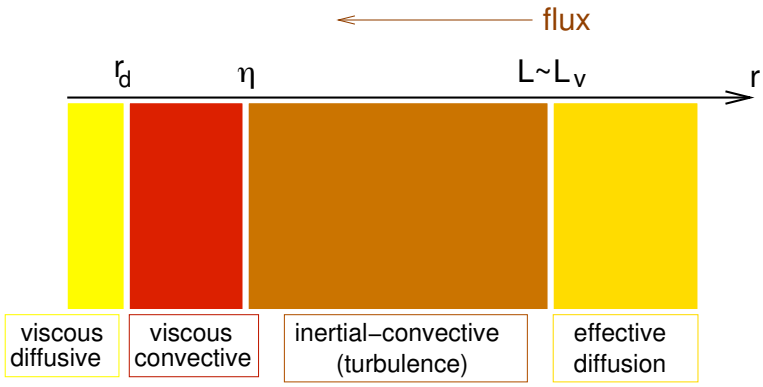

Figure 1.2: Sketch of the typical spatial scales of different processes in turbulence. Here scalar fluctuations are injected at a typical scale L similar to the velocity correlation length L_v.

With the additional incompressibility condition $\boldsymbol{\nabla} \cdot \mathbf{v} = 0$. Here κ is the diffusivity constant and f is the source of scalar fluctuations. Typically, the forcing f injects scalar fluctuations at a certain spatial scale L, dramatically separated from the scale r_d where diffusion processes are active. In this case a turbulent direct cascade takes place, i.e. a flux of scalar fluctuations develops from L towards small scales[1], down to r_d where fluctuations are smeared out by diffusion (see a sketch of the length scales in figure 1.2). Similarly, Navier-Stokes turbulence:

$$\partial_t \mathbf{v} + \mathbf{v} \cdot \boldsymbol{\nabla} \mathbf{v} = -\boldsymbol{\nabla} \frac{p}{\rho} + \nu \Delta \mathbf{v} + \mathbf{f}_v \tag{1.2}$$

provides a cascade process[2] of the velocity fluctuations $|\mathbf{v}|^2/2$, between a typical integral scale L_v and the Kolmogorov viscous scale η. The velocity field is therefore characterized by eddies spanning the whole range of scales from L_v to η. For the moment, and for the whole chapter, let us suppose that $L_v \sim L$, like in figure 1.2. The turbulent cascades of the conserved quantities $|\mathbf{v}|^2/2$ and $\theta^2/2$ take place in the so-called *inertial-convective* range of scales, where research has focused its main interest. In this range of scales, labeled "turbulence" in figure 1.2, a very peculiar and experimentally well documented phenomenology appears [37, 38, 40], both for scalar and Navier-Stokes turbulence. The objects one should observe in order to fully characterize the statistics of the scalar, and enlighten these properties, correspond to the differences $\delta_{\mathbf{r}}\theta$ of the field θ calculated in two points separated by a distance $\mathbf{r}$. In the case of isotropy of the underlying velocity field and of the pumping process f (see e.g. [25, 31] for an experimental realization), the statistics of the scalar differences depend only on $r = |\mathbf{r}|$. One can perform these statistics at various scales r and verify that the PDFs thereby obtained have different shapes. In other words the PDF of the scalar differences at various separations cannot be collapsed one onto another by simple rescaling. In particular, as the separation r decreases in the inertial range, the statistics becomes more and more non-Gaussian, with higher and higher PDF tails. This amounts to state that the

[1] Note that, for incompressible flows $\mathbf{v}$, no upscale flux is present for the passive scalar at scales larger than L, as will be discussed in chapter 2.

[2] The direction of the flux depends on the dimension of the space. Direct cascade develops in three dimensions and inverse cascade in two dimensions.

fine structure of the scalar field tends to be almost-discontinuous, with strong variations across tiny regions known as "fronts", separated by large regions where scalar fluctuations are weak. The presence of this *intermittent* structure of the scalar field is confirmed by both experimental results [37, 38, 40] and direct numerical simulations [11] - see figure 1.1 for example. More precisely, the tails of the PDF of $\delta_r\theta$ can be characterized by considering its moments, the structure functions:

$$S_N(\mathbf{r},t) = \langle[\theta(\mathbf{x}+\mathbf{r},t) - \theta(\mathbf{x},t)]^N\rangle$$

which can be obtained as appropriate combinations of the scalar correlation functions:

$$C_N(\mathbf{x}_1,...,\mathbf{x}_N,t) = \langle\theta(\mathbf{x}_1,t)\theta(\mathbf{x}_2,t)\cdots\theta(\mathbf{x}_N,t)\rangle. \tag{1.3}$$

Experiments and numerics have shown that the structure functions at a fixed order N behave as power laws in r. The exponents of these power laws change with N in a non-linear way, as schematically represented in figure 1.3:

$$S_N(r) \sim r^{\zeta_N} \qquad \zeta_N \neq \frac{N}{2}\cdot\zeta_2$$

This is the so called anomalous scaling of the structure functions and implies the lack of scale invariance for the scalar statistics. Indeed scale invariance would correspond to a linear behavior of the scaling exponents.

The same qualitative behavior is observed in many other problems and in particular in

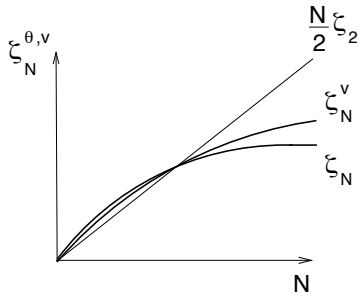

Figure 1.3: Sketch of the normal and anomalous scaling exponents ζ_N^θ for the scalar structure functions and ζ_N^v for Navier-Stokes velocity structure functions. Scalar intermittency is stronger than hydrodynamic intermittency.

hydrodynamic turbulence, i.e. for a velocity field solution of the Navier-Stokes equations (1.2) in the limit for large separation between the integral scale and the viscous scale. However, the anomaly of scalar exponents is much more pronounced than the anomaly for the velocity field (see figure 1.3). As Robert H. Kraichnan importantly realized, the intermittency of the scalar field is not slaved to the presence of an intermittent carrier flow. Following this idea, Kraichnan proposed a model of passive advection by a scale-invariant velocity field whose crucial results are the focus of next section.

1.2 Kraichnan model

Let us consider equation (1.1) with a Gaussian stochastic homogeneous isotropic carrier flow $\mathbf{v}$ [27–29] such that:

$$\langle v_\alpha(\mathbf{x}+\mathbf{r},t)v_\beta(\mathbf{x},s)\rangle = D^{\alpha\beta}(\mathbf{r})\delta(t-s)$$

where the spatial component of the correlation function is scale-invariant in the convective range (i.e. at small scales, up to L_v):

$$D^{\alpha\beta} = D_0\delta^{\alpha\beta} - \frac{1}{2}D_1 r^\xi\left((d-1+\xi)\delta^{\alpha\beta} - \xi\frac{r^\alpha r^\beta}{r^2}\right)$$

Let us take a white in time Gaussian stochastic process for the forcing as well, so that:

$$\langle f(\mathbf{x}+\mathbf{r},t)f(\mathbf{x},s)\rangle = F(\mathbf{r})\delta(t-s)$$

where the spatial component of the forcing correlation is defined as $F(\mathbf{r}) = \langle f(\mathbf{x}+\mathbf{r},t)f(\mathbf{x},t)\rangle$ and is fast decaying beyond the typical length scale L. The delta-correlation in time allows to write a closed equation for the N-point equal-time correlation functions (1.3):

$$\partial_t C_N + M_N C_N = F \otimes C_{N-2} \tag{1.4}$$

where

$$M_N = \sum_{i,j=1}^{N} D^{\alpha\beta}(\mathbf{r}_{ij})\partial_{r_i^\alpha}\partial_{r_j^\beta} + \kappa\sum_{i=1}^{N}\nabla^2_{r_i} \tag{1.5}$$

and the meaning of the symbol $\otimes$ in the right hand side is the following: $F \otimes C_{N-2} = \sum_{i\neq j=1}^{N}\langle\theta(\mathbf{x}_1,t)\cdots\hat{\imath}\cdots\hat{\jmath}\cdots\theta(\mathbf{x}_N,t)\rangle\langle f(\mathbf{x}_i,t)f(\mathbf{x}_j,t)\rangle$ where the symbols $\hat{\imath}$ and $\hat{\jmath}$ indicate that the values of the field θ in points $\mathbf{x}_i$ and $\mathbf{x}_j$ are omitted. Note that equations (1.4) with the expression (1.5) for the operators M_N are valid in the range of scale invariance of the velocity field, i.e. for small scales, up to L_v that is here considered similar to L. This result can be obtained by direct calculations [27]. The great novelty of Kraichnan model comes from the fact that it can be handled analytically. The result is that equations (1.4), in the absence of any intermittency of the velocity field, allow for anomalous scaling of the scalar correlation functions. The origin for that is traced back to statistical integrals of motion, linked to the zero modes of the operators M_N, as described in the next section.

1.2.1 Zero modes and anomalous scaling

The solutions of equations (1.4) can be written recursively as:

$$C_N(\underline{\mathbf{r}}) = \int G_N(\underline{\mathbf{r}};\underline{\mathbf{R}})\, C_{N-2}\otimes F\, d\underline{\mathbf{R}} \tag{1.6}$$

where G_N denotes the kernel of the inverse of $-M_N$ and we use the short-hand notation $\underline{\mathbf{r}} = (\mathbf{r}_1,...,\mathbf{r}_N)$ and $\underline{\mathbf{R}} = (\mathbf{R}_1,...,\mathbf{R}_N)$. The scaling properties of solutions (1.6) are dimensionally expected to be:

$$C_N(\lambda\mathbf{r}_1,...,\lambda\mathbf{r}_N) = \lambda^{(2-\xi)N/2}C_N(\mathbf{r}_1,...,\mathbf{r}_N). \tag{1.7}$$

However, the general solution of equations (1.4) is determined up to homogeneous solutions (or zero modes) of the operator M_N. In other words, the complete solution is the superposition of the normal scaling component (1.7) and the zero modes. Dimensional arguments do not apply to the latter, whose scaling properties are therefore called anomalous and might dominate the behavior of the solution, thus clarifying the origin of intermittency. The scaling behavior of the zero modes have been obtained exactly for the two-point correlation functions, and perturbatively around $\xi = 0$ or $d \to \infty$ for higher orders. These perturbative schemes allow to conclude that the anomalous scaling is indeed dominant in the convective interval. More precisely, the *irreducible*[3] zero-mode scaling exponents, in the limit for small ξ, are $\zeta_N = (N/2)(2-\xi) - N(N-2)/[2(d+2)] + O(\xi^2)$ (see [3,23]). Similarly, for large space dimensionalities, the zero-mode exponents are $\zeta_N = (N/2)(2-\xi) - N(N-2)/(2d) + O(1/d^2)$ as proved in [14]. In both cases they dominate the small scale behavior of the correlation functions, since they are smaller than the normal scaling exponent $(N/2)(2-\xi)$.

The zero modes of operators M_N show up in the study of the asymptotic expansion of G_N. Let us denote by Z_a the zero modes satisfying:

$$M_N Z_a(\underline{\mathbf{r}}) = 0. \tag{1.8}$$

The zero modes come in pairs ($Z_a^+(\underline{\mathbf{r}})$ and $Z_a^-(\underline{\mathbf{r}})$), with scaling exponents of opposite signs ζ_a^+ and $\zeta_a^- = -(n-1)d + (2-\xi) - \zeta_a^+$. It turns out that the kernel $G_N(\underline{\mathbf{r}}, \underline{\mathbf{R}})$ has asymptotic expansions:

$$G_N(\underline{\mathbf{r}}; \underline{\mathbf{R}}) = \sum_a Z_a^+(\underline{\mathbf{r}}) Z_a^-(\underline{\mathbf{R}}) \qquad \text{for } |\underline{\mathbf{r}}| \ll |\underline{\mathbf{R}}| \tag{1.9}$$

1.2.2 Small scale anisotropy

In general, the injection mechanism is not isotropic, as experimentally studied in [37]. In this case, C_N and F may be conveniently projected on the basis of eigenfunctions of the squared angular momentum, labeled by their eigenvalues $-j(j+d-2)$. Equations (1.4) can be projected in each j-sector, and because of the symmetry of operators M_N for rotations, the problem decouples in a system of m independent partial differential equations, where m is the number of sectors excited by the forcing f. In each excited sector, all the above arguments apply and we finally obtain a global solution C_N which is a sum of m contributions coming from each excited sector. At fixed order N, the zero-mode exponents are ordered so that the zero mode of the lower excited sector is leading over the other zero modes. In this sense, isotropy is recovered at small scales if the lower excited zero mode is the isotropic one (see [5]). Note that the lowest excited zero mode might be turned off in the case where it appears in the linear combination multiplied by a vanishing coefficient. Hence the crucial importance of the coefficients that might switch off some of the terms contributing to C_N, thus changing the global behavior of the solution. This will be crucial for the propagation of small-scale anisotropy toward large scales (see section 2.2).

[3] The irreducible zero modes are functions that depend non-trivially on all the positions of the N points and turn out to be dominant on the reducible ones.

1.3 Real flows and Lagrangian viewpoint

The most suitable language for the study of the passive scalar turns out to be the Lagrangian statistical formalism, thoroughly reviewed in [18]. The latter focuses on the trajectories of fluid particles $\mathbf{R}(t)$ such that:

$$\dot{\mathbf{R}}(t) = \mathbf{v}(\mathbf{R}(t), t) + \sqrt{2\kappa}\,\boldsymbol{\varsigma}(t) \tag{1.10}$$

where $\boldsymbol{\varsigma}(t)$ is a white noise with zero mean and covariance $\langle \varsigma_i(t)\varsigma_j(t')\rangle = \delta_{ij}\delta(t-t')$. The Lagrangian trajectories are connected with the statistics of the advected fields. Given the multi particle statistics, one can build the correlation functions of the latter and this allows to recognize the zero modes above introduced and give them an interpretation. Zero modes turn out to be Lagrangian integrals of motion, i.e. functions of the inter particle separations that are statistically preserved as the particles are transported by the flow (see [15, 23, 33]). Clearly the nature of these integrals of motion strongly differs from that of the dynamical integrals of motion in equilibrium systems.
The solution of equation (1.10) is determined for a given initial condition $\mathbf{R}(0)$. The scalar field evolves along the Lagrangian trajectories following:

$$\frac{d}{dt}\theta(\mathbf{R}(t), t) = f(\mathbf{R}(t), t)$$

Thus:

$$\begin{aligned} C_{2N}(\underline{\mathbf{r}}, t) &= \Big\langle \int^t f(\mathbf{R}_1(s_1), s_1)\, ds_1 \cdots \int^t f(\mathbf{R}_{2N}(s_{2N}), s_{2N})\, ds_{2N} \Big\rangle = \\ &= \Big\langle \int^t F(\mathbf{R}_{12}(s_1))\, ds_1 \cdots \int^t F(\mathbf{R}_{(2N-1)(2N)}(s_N)\, ds_N \Big\rangle + \cdots \end{aligned} \tag{1.11}$$

where the average $\langle\cdot\rangle$ is meant over the ensemble of the velocity, noise and forcing realizations. In the second line the average over the forcing realizations has been computed and the dots stand for the permutations of the pairings between the $2N$ particles. The functions F essentially restrict the integration to the time interval where the inter particle separations R_{ij} were smaller than the injection scale L. The kernel $G_N(\underline{\mathbf{r}}, \underline{\mathbf{R}})$ has exactly the meaning of the time that particles spend at given positions $\underline{\mathbf{r}}$ given their final distance $\underline{\mathbf{R}}$.
More precisely, the Lagrangian evolution is described by the multi particle Green functions $P_N(\underline{\mathbf{r}}; \underline{\mathbf{R}}; t) = \langle \prod_{i=1}^N p(\mathbf{r}_i, s; \mathbf{R}_i, t|\mathbf{v})\rangle$. The latter denote the transition probability that N particles starting at positions $\mathbf{R}_1, ..., \mathbf{R}_N$ arrive at positions $\mathbf{r}_1, ..., \mathbf{r}_N$ at time t. The $P_N(\underline{\mathbf{r}}; \underline{\mathbf{R}}; t)$ satisfy equations:

$$\partial_t P_N(\underline{\mathbf{r}}; \underline{\mathbf{R}}; t) = M_N P_N(\underline{\mathbf{r}}; \underline{\mathbf{R}}; t) \tag{1.12}$$

The kernel G_N of the inverse of $-M_N$ is the time integral of the Green function

$$G_N(\underline{\mathbf{r}}; \underline{\mathbf{R}}) = \int_0^\infty P(\underline{\mathbf{r}}; \underline{\mathbf{R}}; t) dt$$

Therefore, given the Green functions, one is able to compute the scalar multi-point correlations through relation (1.6). The asymptotic expansion of P_N for initially close particles is

a combination of zero modes and slow modes, which are essentially zero modes of powers of the operators M_N (see [4]). The asymptotic expansion of G_N is consistent with (1.9):

$$G_N(\underline{\mathbf{r}};\underline{\mathbf{R}}) = \int_0^\infty P(\underline{\mathbf{r}};\underline{\mathbf{R}};t)dt = \sum_a Z_a^+(\underline{\mathbf{r}})Z_a^-(\underline{\mathbf{R}}) \qquad \text{for} \quad |\underline{\mathbf{r}}| \ll |\underline{\mathbf{R}}|. \tag{1.13}$$

Given the equation of evolution (1.12) for the Green functions, one can show that the zero modes are scaling structures preserved in mean by the flow. This fact is simply proved by writing the Lagrangian average through an integral of the zero mode multiplied by the Green functions P_N: $\langle Z_a(\underline{\mathbf{R}}(t))\rangle = \int P(\underline{\mathbf{r}};\underline{\mathbf{R}};t)Z_a(\underline{\mathbf{R}})d\underline{\mathbf{r}}$. The time derivative of $\langle Z_a(\underline{\mathbf{R}}(t))\rangle$ vanishes simply because of equations (1.12), (1.8) and the fact that M_N is Hermitian: $\frac{d}{dt}\langle Z_a(\underline{\mathbf{R}}(t))\rangle = \int \partial_t P(\underline{\mathbf{r}};\underline{\mathbf{R}};t)Z_a(\underline{\mathbf{R}};0)d\underline{\mathbf{r}} = \int P(\underline{\mathbf{r}};\underline{\mathbf{R}};t)M_N Z_a(\underline{\mathbf{R}};0)d\underline{\mathbf{r}} = 0$. We have already seen that the anomalous scaling of the scalar correlation functions origins from the zero modes that we can now interpret as statistical integrals of motion. This picture is quite robust and relevant for transport by generic turbulent flows.

The physical mechanism that allows for the Lagrangian-average preservation of the zero modes is a compensation between two opposite trends. When N initially close particles evolve in the flow, the size of the cloud of particles - defined as $R = \sum_{n<m} R_{nm}^2/N$ - grows, while the shape is deformed by the local structure of the flow. The Lagrangian average $\langle Z_a(\underline{\mathbf{R}}(t))\rangle$ grows with the size R and is depleted by the shape evolution. The two behaviors cancel out and the zero mode is preserved toward the Lagrangian evolution.

Note that the specific assumptions of the Kraichnan model are directly needed only in deriving closed evolution equations for the Green functions. However, the picture drawn within the Lagrangian framework allows to learn qualitative lessons for general scalar turbulence. In particular the asymptotic expansion (1.13) holds for real flows as well (see [4]). The numerical values of the real anomalous exponents are not expected to match their Kraichnan-model predictions, as well as the numerical coefficients of the solutions for C_N. Nevertheless, the presence of statistical integrals of motion, preserved by the Lagrangian evolution remains a fundamental idea. Indeed, the Lagrangian viewpoint has suggested an effective numerical strategy that has confirmed the general picture drawn from the Kraichnan model for real flows as well (see [10, 12, 21, 22]). Hence the great importance of the Kraichnan model and of the Lagrangian picture, highlighting the crucial role of the zero modes.

Chapter 2

The large-scale breakdown of Gibbs equilibrium

In November 2004, a workshop was organized in Eilat, a small town on the Red Sea. There, Alexander Fouxon presented for the first time his work in collaboration with Gregory Falkovich on the anomalous scaling of the passive scalar at large scales [17]. They essentially modified the order of spatial length scales presented in figure 1.2, and considered the range of scales delimited below by the scalar injection scale L and above by the flow correlation length L_v (already studied in refs [1, 2, 19]). This range of scales is shown in green in figure 4. By analytical calculations in the Kraichnan model framework, they obtained zero modes for the fourth and sixth order correlation functions of the scalar field. I participated in the conference together with Antonio Celani and got interested in the problem. Since no upscale flux of scalar fluctuations develops, this range of scales is expected to display equilibrium statistics, although the presence of an underlying turbulent velocity field provides mixing. What is the Lagrangian origin of the arising large-scale anomaly? I traced back the presence of large-scale zero modes to correlations between two evolving scalar blobs. In this sense, the emerging anomalous scaling is related to a breakdown of Gibbs equilibrium, whose fundamental assumption of independence of the dynamics at different points in space is clearly violated in the presence of long-range correlations. This is the essence of the work I performed in this framework, that finally allowed to extend the results of Falkovich and Fouxon to realistic flows.

Later on, I got interested in the large-scale anisotropy of passive scalar turbulence. First, I performed a rigorous analysis in the Kraichnan model framework that highlighted the presence of anisotropic zero modes dominating, in broad conditions, the large-scale correlations. Then, I extended the result to realistic flows by direct numerical simulations. In this case, the breakdown of Gibbs equilibrium is even more dramatic than in the isotropic one, since it occurs already at the level of the two-point statistics. In other words, the large-scale dominance of anisotropy is noticeable from a single scalar snapshot, which is organized in large-scale elongated structures.

In the following I present the two sets of results I obtained for the large-scale structure of passive scalar turbulence, that have been published in the papers shown below.

2.1 Equilibrium violation in large-scale isotropic scalar turbulence

Let us consider the passive scalar problem (1.1) in the above-mentioned range of scales larger than L and smaller than L_v, like in the green region of figure 4. Here no scalar flux emerges, so that we might expect the scalar to be well-described by Gibbs equilibrium. The basic assumption of equilibrium statistics is that particles evolve independently one from the other. The Gibbs functional, under this assumption, allows to obtain the statistics of each Fourier mode, that turns out to be Gaussian with variance determined by the small scales pumping mechanism. In analogy with statistical mechanics, this range is labeled "thermal equilibrium", with an effective temperature determined by the small-scale turbulence. The scalar fluctuations are then expected to be distributed among all the different Fourier modes according to equipartition.

I performed a numerical analysis of the problem, choosing a two-dimensional velocity field in the inverse cascade of Navier-Stokes turbulence (see equation (1.2)), forced at small scales by a white in time forcing and dissipated by viscosity at small scales and by a drag-term proportional to $\mathbf{v}$ itself at large scales. This flow has been studied both experimentally [26, 39] and numerically [6, 7, 9, 11, 12, 36]. The velocity field is statistically homogeneous and isotropic, scale-invariant with exponent $1/3$ with no intermittency corrections.

Then I integrated the passive scalar evolution (equation (1.1)), isotropically forced at a scale L slightly larger than the dissipation scale. A small convective range established under L and the direct cascade process could develop (see figure 4 for a schematic view of the spatial scales order). Once the stationary state was reached, I measured the two-point correlation at scales larger than L and - not surprisingly - it satisfied equipartition at a very good level of precision (see figure 2.1). Details on the simulations can be found in the article presented below.

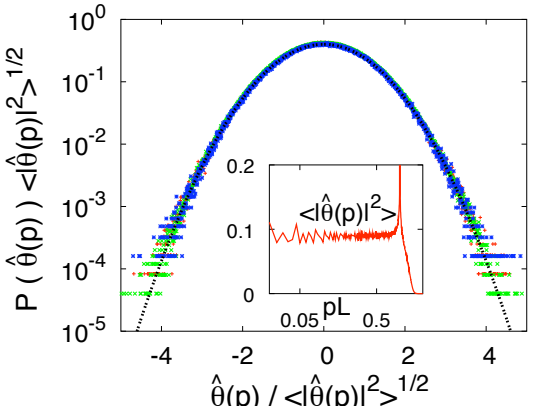

Figure 2.1: Marginal probability density function for three modes of the Fourier transformed scalar, in the range $L^{-1} > p > L_v^{-1}$. The dotted line corresponds to the equilibrium (Gaussian) expectation, shown for comparison. Inset: spectral density. Notice the neat plateau according to equipartition.

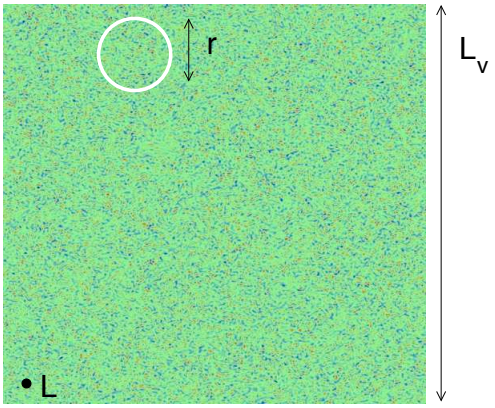

Figure 2.2: Scheme of the coarse-graining of the passive scalar field. Here a portion of a typical scalar snapshot obtained by 2D 1024X1024 direct numerical simulations is shown (see the paper presented at page 63 for the details). θ is injected at the scale L, the turbulent range develops at smaller scales. Thus, the typical intermittent structure of turbulence is not visible from the figure. The coarse-grained field θ_r is essentially an average of the field on domains of size r such that $L \ll r \ll L_v$, like the white circle in the figure. Each blob of size r contains $(r/L)^d$ scalar-correlation-length blobs and the variable θ_r - in the case of true Gibbs equilibrium - can be considered as a sum of $(r/L)^d$ independent variables.

2.1.1 Coarse-graining

However, the equilibrium two-point statistics is not enough to assure thermal equilibrium of the scalar. The presence of the fourth and sixth orders anomalies suggests that the breakdown of equilibrium would become apparent only after a finer analysis of the system. The higher-order correlation functions will turn out to be definitely non-trivial.
In order to get information on the multi-point statistics, I focused on the coarse-grained scalar field. This object is obtained by the original scalar field θ after a filtering procedure that basically averages the scalar over volumes of size r:

$$\theta_r(\mathbf{x}, \mathbf{t}) = \int G_r(\mathbf{x} - \mathbf{y})\theta(\mathbf{y}, t)\, d\mathbf{y} \tag{2.1}$$

The actual form of the filter G_r is not very relevant, a generic filter which is almost constant under the scale r and rapidly vanishes at scales larger than r serves the purpose (see figure 2.2 for a scheme of the coarse-graining procedure).
What is the Gibbs-equilibrium expectation for the statistics of the coarse-grained field?

2.1.2 Central-limit-theorem violation

The hypothesis of independence, which is implicitly assumed when speaking of Gibbs equilibrium, provides a powerful tool for making predictions: the central limit theorem. If $r > L$, the support of the filter G_r can be imagined as composed of $(r/L)^d$ blobs of size L. On the basis of a Gibbs-equilibrium picture, one expects each blob to be independent from the others, since no large-scale correlations are expected. Therefore the variable θ_r can be thought of as a sum of $(r/L)^d$ independent variables identically distributed:

$$\theta_r = \frac{1}{N}\sum_{i=1}^{N} \theta_L(i) \qquad N \propto (r/L)^d \tag{2.2}$$

By central-limit theorem the random variable θ_r should converge to a Gaussian with zero mean and moments $\langle\theta_r^{2n}\rangle = \langle\theta^2\rangle^n/N \propto \langle\theta^2\rangle^n/(r/L)^d$ in the limit of large number N of independent terms in the sum (2.2), i.e. of large r. The central-limit theorem provides a further and finer information than the limit of the series: it tells us how "fast" the Gaussian limit is approached. The *cumulants* are the relevant observables to determine this rate of convergence and compare it with the equilibrium expectation. The cumulants of a random variable are the differences between the n-moments of the variable and the Gaussian expectation for the n-moments. Cumulants and moments of the random variable θ_r are thus linked by a relation, that for orders 4 and 6 reads:

$$\langle\langle\theta_r^4\rangle\rangle = \langle\theta_r^4\rangle - 3\langle\theta_r^2\rangle^2 \sim (r/L)^{-16/3} \tag{2.3}$$

$$\langle\langle\theta_r^6\rangle\rangle = \langle\theta_r^6\rangle - 15\langle\theta_r^2\rangle^2\langle\theta_r^4\rangle + 30\langle\theta_r^2\rangle^3 \sim (r/L)^{-22/3} \tag{2.4}$$

where the scaling exponents are the theoretical anomalous exponents computed in [17] to be compared with the central-limit theorem expectations $\langle\langle\theta_r^4\rangle\rangle \sim (r/L)^{-6}$ and $\langle\langle\theta_r^6\rangle\rangle \sim (r/L)^{-10}$. Note that both cumulants decrease with r, so that it becomes extremely difficult to measure the signal against the noise at large r. Moreover strong cancellations make the convergence of the statistics extremely slow. The numerical analysis of the coarse-grained-scalar cumulants shows a neat violation of the equilibrium expectation, thus hinting to long-range correlations. As shown in figure 2.3, the anomalous exponents of the slow approach of the coarse-grained field to Gaussianity are in good agreement with the anomalous exponents computed in [17] in the Kraichnan model framework.

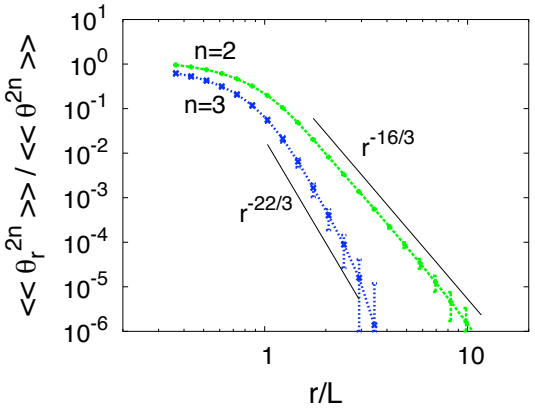

Figure 2.3: Cumulants of the coarse grained scalar field obtained by DNS of passive scalar transport by a two-dimensional velocity field (see caption of figure 2.2). The decay of the fourth and sixth order cumulants are slower than expected on the basis of equilibrium. The anomalous exponents are close to the theoretical predictions. The best fits give -5.32 ± 0.05 and -7.5 ± 0.5 for the fourth and sixth order cumulant exponent respectively, compared to the theoretical values $-16/3$ and $-22/3$ shown for comparison.

2.1.3 Long-range correlations

When computing the fourth-order cumulant, the leading contributions are given by sets of points arranged in two pairs of close particles, separated by a large distance r. This

amounts to state that the squared-scalar field correlations $\langle\theta^2(\mathbf{x}+\mathbf{r},t)\theta^2(\mathbf{x},t)\rangle$ must display a non-trivial power-law behavior with the correct exponent that gives rise to the anomalous exponent of $\langle\langle\theta_r^4\rangle\rangle$. I verified this expectation by analyzing the coarse-grained squared scalar statistics. The results, shown in figure 2.4 point to a good agreement with the theoretical expectation $\langle\langle\theta_r^4\rangle\rangle \sim (r/L)^{-4/3}$.

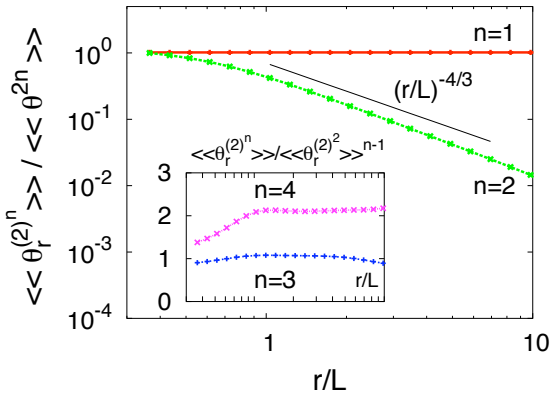

Figure 2.4: Cumulants of the coarse-grained square scalar field. The decay of the second order cumulant display a power law decay with exponent very close to the theoretical expectation $-4/3$, shown for comparison.

The physical mechanism at the basis of these correlations is given by the underlying turbulent velocity field. Indeed, it turns out that the squared-scalar field computed in two different points $\theta^2(x_1,t)\theta^2(x_2,t)$ is equivalent to a product of random variables. Physically the meaning of these random variables is the time taken by two small scalar blobs to disperse across the length scale L. Were the two scalar blobs independent, the squared scalar would display no anomaly. But in the presence of an underlying flow, the two scalar blobs are not uncorrelated. The observed anomaly is the effect of events where the two scalar blobs evolve both coherently and their size remains for a long time smaller than L. The results described in this section have been published in the paper presented at page 63.

2.2 Equilibrium violation and large-scale anisotropy

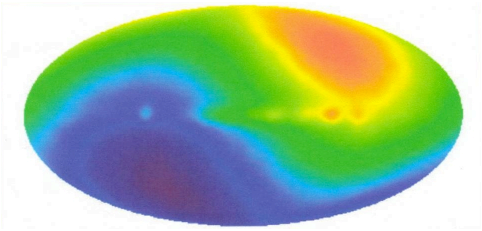

Figure 2.5: Instance of large-scale anisotropy in physics. Anisotropic structure of the cosmic microwave background radiation

Let us now remove the assumption of isotropy and consider a scalar forcing f that excites both isotropic and anisotropic sectors. We have already pointed out that the large-scale statistics of the passive scalar is markedly non-trivial already for the isotropic case. In the case of anisotropy an even more dramatic anomaly takes place already at the level of the two-point statistics. This provides, in very broad conditions, a predominance of the anisotropic component in the large-scale structure of the passive scalar.
Note that the propagation of anisotropy toward large scales is a question related to the most diverse fields of physics. The large-scale anisotropy of the cosmic-microwave-background-radiation has been supposed to originate from the big bang and to have then propagated in space and time [8] (see figure 2.5). Additionally the anisotropic propagation of seismic signals has been traced back to the anisotropic structure of the crystals in mantle rocks [35].

2.2.1 Kraichnan model analysis

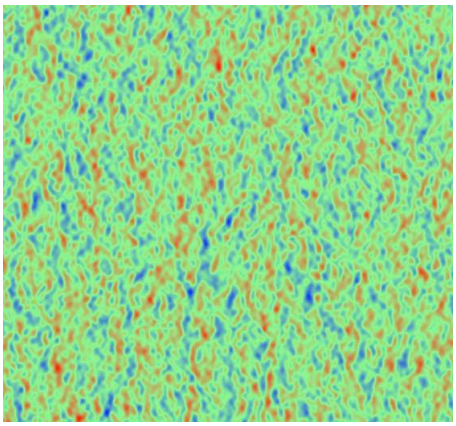

Figure 2.6: Snapshot of a scalar field advected by a Kraichnan velocity field with $\xi = 0$ in two dimensions. The scalar is injected at small scales (L) with a pumping preferentially acting on the vertical direction. The propagation of anisotropy toward large scales manifests itself in the presence of elongated structures much larger than the injection scale.

As a first step I treated the problem analytically in the Kraichnan model framework. The same arguments given in chapter 1 for the convective-inertial range of scales can be repeated and applied to the thermal-equilibrium scales. As already mentioned, the large-scale anisotropy of the passive scalar is already clear at the level of the two-point function. In order to prove that, I first wrote the two point function and the forcing correlation function on the basis of the eigenfunctions $Y_j(\hat{r})$ of the angular momentum: $C(\mathbf{r}) = \sum_{j=1}^{m} C_j(r) Y_j(\hat{\mathbf{r}})$, $F(\mathbf{r}) = \sum_{j=1}^{m} F_j(r) Y_j(\hat{\mathbf{r}})$. By virtue of the symmetry of operators M_N (1.5) under rotations, the problem (1.4) decouples in m independent partial differential equations, one for each excited sector:

$$M_j C_j = F_j \qquad M_j = D[(d-1) r^{1-d} \frac{d}{dr} r^{d-1+\xi} \frac{d}{dr} - j(j+d-2)(d+\xi-1) r^{\xi-2}]$$

The solutions can be written by means of the kernel $G_j(\mathbf{r}, \mathbf{R})$ as in (1.6). Considering the

large-scale expansion (1.9), in each j-sector, one ends up with the behavior:

$$C_j(r) \approx Z_j^-(r) \int_0^\infty dR \frac{R^{d-1}}{D(\zeta_j^- - \zeta_j^+)} Z_j^+(R) F_j(R) \qquad \text{for} \quad \frac{r}{L} \gg 1 \tag{2.5}$$

where $Z_j^\pm = r^{\zeta_j^\pm}$ are the two-point zero modes of the operators M_j:

$$M_j Z_j = 0.$$

The exponents $\zeta_j^\pm$ are easily obtained by the characteristic second-order equation:

$$\zeta_j^2 + \xi\zeta_j - (1+\xi)j^2 = 0$$

There are two solutions of opposite signs $\zeta_j^+ > \zeta_j^-$: only $r^{\zeta_j^-}$ is regular at large-scales. Now, since the zero-mode exponent ζ_j^- is maximum for the minimum excited sector, in the case where all the zero-modes are contributing to the behavior of the solution, the latter will surely have an isotropic dominance, since the isotropic zero mode will be the slowest decaying.
Note that, however, the integral in equation (2.5) gives a constant prefactor multiplying the large-scale zero mode in each excited sector. Some of these constants $q_j = \int_0^\infty dR\, R^{d-1} Z_j^+(R) F_j(R)/[D(\zeta_j^- - \zeta_j^+)]$ might vanish, thus "switching off" the j-th zero-mode contribution. Let us consider the special case for the $j = 0$ sector. Since the positive isotropic exponent ζ_0^+ vanishes, the constant q_0 reduces to:

$$q_0 = \int_0^\infty dR \frac{R^{d-1}}{D(-d+2-\xi)} F_0(R) = \int_0^\infty dR \frac{R^{d-1}}{D(-d+2-\xi)} \int_\Omega F(\mathbf{R}) d\Omega \propto \int F(\mathbf{R}) d\mathbf{R} \tag{2.6}$$

In other words, q_0 is the mean forcing correlation function or the value of its Fourier transform at wavenumber zero. This quantity does vanish for the very common choice of forcings localized in the wave-number space.
Under these very broad conditions, the isotropic zero mode does not contribute to the scalar correlation function due to the condition $q_0 = 0$. Other q_j are not forced to vanish, because no special relation like (2.6) holds for generic j. Therefore the slow power law behavior of the lowest anisotropic sector should in general dominate the large-scale structure of the passive scalar field. I verified this general expectation with a particular choice of the forcing correlation function and $d = 2$.

2.2.2 Lagrangian interpretation

Let us suppose to simply deal with a forcing that excites the isotropic sector and the $j = 2$ sector, with a fast-decaying correlation function for scales larger than L. A picture of a similar forcing correlation function is given in figure 2.7(a). One can build the large-scale behavior of the two-point correlation function by following the Lagrangian trajectories of two generic particles (see 2.7(b)), starting at a very large distance r one from the other. The scalar correlation function is obtained by the following integral:

$$C(\mathbf{r}, t) = \langle \int_0^t F(\mathbf{R}(s), s) ds \rangle \qquad \mathbf{R}(t) = \mathbf{r} \tag{2.7}$$

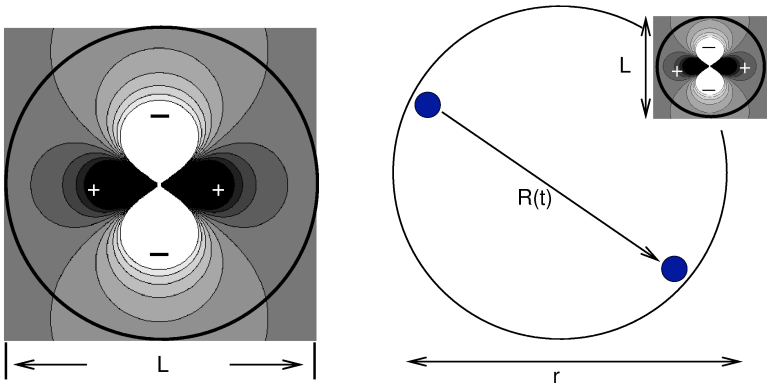

Figure 2.7: Example of forcing correlation function exciting 2 sectors. The forcing is positively correlated on the horizontal direction and negatively on the vertical one.

where the Lagrangian average is made on particles separated at time t by a distance $\mathbf{r}$. The integral is essentially zero until the particles come to a distance smaller than L. In order to extract the isotropic component one should average $C(\mathbf{r}, t)$ on all randomly distributed initial directions $\hat{r}$. The positive and negative contributions coming from vertically and horizontally aligned particles, cancel during the average: the isotropic component of C collects only exponentially small contributions. On the contrary, in order to extract the anisotropic component, one should perform the average by giving different weights to the different directions in space. Since particles trajectories keep a memory of their initial conditions due to the underlying turbulent advection, the different weights are not completely random when particles get closer than L. Therefore, positive and negative contributions do not cancel and give a slow power-law decay of the anisotropic scalar correlation. Hence the anisotropic nature of large-scale scalar turbulence.

2.2.3 Realistic flows

This Lagrangian interpretation suggests that the same results should hold for realistic flows. I thus performed direct numerical simulations of a two-dimensional Navier-Stokes velocity field (see section 2.1), advecting a passive scalar θ, forced at scale L anisotropically. The order of the length scales is like in figure 4, and the details of the simulations are given in the papers below. I could prove that the whole picture built first with the Kraichnan model analysis and then by the Lagrangian interpretation holds for realistic flows as well. The scalar two-point correlation, obtained by Fourier transforming the scalar spectra (see figure 2.8), shows a slow power-law decay of the anisotropic component, dominating the fast-decay of the isotropic one. As shown in figure 2.6, the large-scale anisotropy is visible from a single snapshot of the scalar that reveals the presence of elongated structures, much larger than the scalar correlation length L.

It would be interesting to check whether the traditional equilibrium expectation is violated

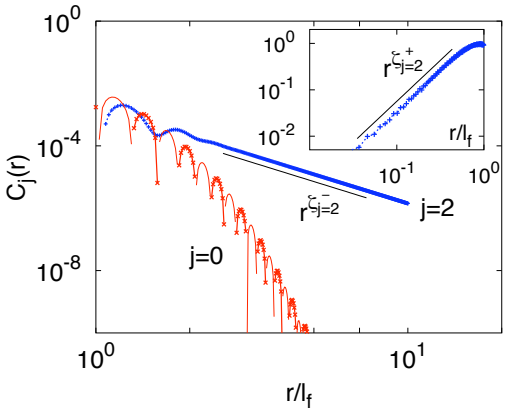

Figure 2.8: Scalar two-point correlation function obtained by DNS of a passive scalar transported by a two-dimensional Navier-Stokes flow in the inverse cascade regime. The order of the spatial scales is shown in figure 4, and the scalar injection is anisotropic, as shown in figure 2.7(a). The slow power-law decay of the anisotropic component dominates over the fast decay of the isotropic one. In the inset the small scale positive anisotropic zero mode.

also in other systems, like three-dimensional hydrodynamic turbulence. The general idea is that an alternative equilibrium picture might arise in this context. The probability distribution of different states of the system might be deduced from a modified version of the Gibbs functional. Theoretical, numerical and experimental further insights would be extremely interesting to clarify this point. The results descibed in this section have been published in the paper presented at page 67.

PRL **94,** 214503 (2005) PHYSICAL REVIEW LETTERS week ending 3 JUNE 2005

Large-Scale Structure of Passive Scalar Turbulence

Antonio Celani and Agnese Seminara
CNRS, INLN, 1361 Route des Lucioles, 06560 Valbonne, France
(Received 27 January 2005; published 3 June 2005)

We investigate the large-scale statistics of a passive scalar transported by a turbulent velocity field by means of direct numerical simulations. We focus on scales larger than the characteristic length scale of scalar injection, yet smaller than the correlation length of the velocity. We show the existence of nontrivial long-range correlations in the form of new power laws for the decay of high-order coarse-grained scalar cumulants. This result contradicts the classical scenario of Gibbs equilibrium statistics that should hold in the absence of scalar flux. The breakdown of ''thermal equilibrium'' at large scales is traced back to the statistical geometry of turbulent dispersion of two scalar blobs. The numerical values obtained for the scaling exponents of the coarse-grained scalar cumulants are in agreement with recent theoretical results.

DOI: 10.1103/PhysRevLett.94.214503 PACS numbers: 47.27.-i

The evolution of a passive scalar field $\theta(\boldsymbol{x}, t)$, like dilute dye concentration or temperature in appropriate conditions, transported by an incompressible velocity field $\boldsymbol{v}(\boldsymbol{x}, t)$, is governed by the advection-diffusion equation

$$\partial_t \theta + \boldsymbol{v} \cdot \nabla \theta = \kappa \Delta \theta + f, \tag{1}$$

where f is a source of scalar fluctuations that acts at a length scale L. We are interested in the typical situation where the velocity field is turbulent and characterized by a self-similar statistic $[v(x + r) - v(x)] \sim r^{1/3}$ in the range of scales delimited above by the velocity correlation length L_v and below by the viscous scale η. Passive scalar fluctuations are generated at the scale L, form increasingly finer structures due to velocity advection, and originate a net flux of scalar variance to small scales, where it is eventually smeared out by molecular diffusivity at a scale r_d. Here we will consider the case where these scales are ordered as follows: $L_v \gg L \gg \eta, r_d$. In the range $L \gg r \gg r_d$ the average scalar flux is constant and equals the average input rate: this is the well studied inertial-convective range where θ displays non-Gaussian statistics and anomalous scaling [1,2].

In this Letter we focus our attention on the range of scales larger than L. There, no scalar flux is present. Accordingly, one would expect Gaussian statistics and equipartition of scalar variance, i.e., the hallmarks of statistical equilibrium. Contrary to this expectation, we show that, in the intermediate range $L_v \gtrsim r \gtrsim L$, the ''thermal equilibrium'' scenario breaks down due to the appearance of new nontrivial power laws for the decay of high-order scalar correlations. These are traced back to the presence of long-range correlations in the dynamics of two scalar blobs advected by the turbulent velocity field. Our results extend the recent findings by Falkovich and Fouxon [3]—obtained in the context of the Kraichnan model of passive scalar advection where the velocity field is Gaussian, self-similar and short-correlated in time—to passive scalar advection by a realistic turbulent flows.

As an instance of a dynamical turbulent flow we consider two-dimensional Navier-Stokes turbulence in the inverse cascade range. This flow has been studied in great detail both experimentally (in fast flowing soap films [4] and in shallow layers of electromagnetically driven electrolyte solutions [5]) and numerically [6,7]. The velocity is statistically homogeneous and isotropic, scale-invariant with exponent $1/3$ (no intermittency corrections to Kolmogorov scaling) and with dynamical correlation times scaling as $r^{2/3}$ as expected on dimensional grounds. This flow has also been utilized to investigate passive scalar transport in the range $L \gtrsim r \gtrsim r_d$ [8] and multiparticle dispersion, an intimately related subject [9].

Let us start the description of our results by recalling that the equilibrium statistics for the scalar field is described by the Gibbs functional $\mathcal{P}[\hat{\theta}] = Z^{-1} \exp[-\beta \int |\hat{\theta}(\boldsymbol{k})|^2 d\boldsymbol{k}]$. Accordingly, in the range $kL \lesssim 1$, where no scalar flux is present, the Fourier modes should behave as independent Gaussian variables with equal variance $1/(2\beta)$ (equipartition), and the isotropic spectrum $E(k) = 2\pi k \langle |\hat{\theta}(\boldsymbol{k})|^2 \rangle$ should be proportional to k. As shown in Fig. 1, we indeed observe $E(k) \sim k$ and a statistics of single Fourier modes indistinguishable from Gaussian. However, from those findings alone one cannot state conclusively that large-scale passive scalar is in a thermal equilibrium state, given that they do not allow to rule out the possibility of long-range correlations for higher-order observables (e.g., four-point scalar correlations). A more refined description of the large-scale properties of the passive scalar is thus required. It can be obtained in terms of the coarse-grained field

$$\theta_r(\boldsymbol{x}, t) = \int G_r(\boldsymbol{x} - \boldsymbol{y}) \theta(\boldsymbol{y}, t) d\boldsymbol{y} \tag{2}$$

where G_r acts as a low-pass filter in Fourier space (for instance, the top-hat filter $G_r(\boldsymbol{x} - \boldsymbol{y}) = 1/(\pi r^2)$ if $|\boldsymbol{x} - \boldsymbol{y}| < r$ and zero otherwise; or the Gaussian filter $G_r(\boldsymbol{x} - \boldsymbol{y}) = (2\pi r^2) \exp[-|\boldsymbol{x} - \boldsymbol{y}|^2/(2r^2)]$). For $r \to 0$ the filter reduces to a two-dimensional δ function and therefore $\theta_r \to \theta$.

PRL 94, 214503 (2005) PHYSICAL REVIEW LETTERS week ending 3 JUNE 2005

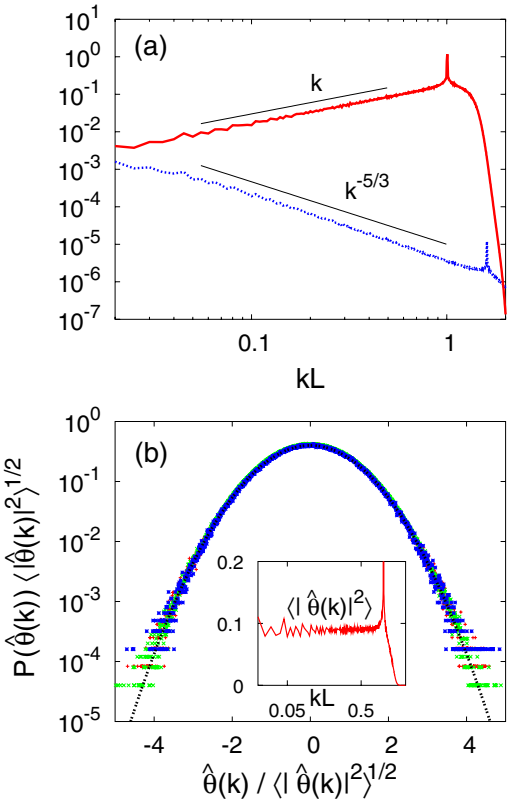

FIG. 1 (color online). (a) Passive scalar (red, upper trace) and velocity (blue, lower trace) spectra. The data result from the time integration of the two-dimensional Navier-Stokes equations $\partial_t \boldsymbol{v} + \boldsymbol{v}\cdot\nabla\boldsymbol{v} = -\nabla p + \nu\Delta\boldsymbol{v} + \boldsymbol{F} - \alpha\boldsymbol{v}$ and Eq. (1) by a pseudospectral method on a 1024^2 grid. The term $-\alpha\boldsymbol{v}$ is a kinetic energy sink used to model the effect of air friction on thin soap films. The passive scalar is injected by a Gaussian, δ correlated in time, statistically homogeneous, and isotropic forcing restricted to a narrow band of wave numbers. The initial condition for the velocity field is a configuration taken from a previous long-time integration and thus already at the statistically stationary state. The passive scalar starts from a zero field configuration, and after a transient of a few large-eddy turnover times $\tau_v = L_v/v_{\rm rms}$ where L_v is the integral scale of the velocity field, it reaches its own statistically steady state as well. Time averages are taken after this relaxation time has elapsed, for a total duration of more than 10^4 scalar correlation times $\tau_L \approx \tau_v(L/L_v)^{2/3}$. Here $L/L_v \approx 0.02$. The velocity spectrum agrees with the Kolmogorov prediction $k^{-5/3}$ and the passive scalar one follows very closely the equipartition spectrum in two-dimensions $E(k) \sim k$ [see also the inset of panel (b)]. (b) The marginal probability density function of a single Fourier amplitude $\hat{\theta}(\boldsymbol{k})$ is indistinguishable from a Gaussian (dotted curve) for all wave numbers in the range $L^{-1} \gtrsim k \gtrsim L_v^{-1}$. Here are shown three wave numbers with $kL = 0.5$, 0.25, 0.12. In the inset is shown the spectral density $\langle|\hat{\theta}(\boldsymbol{k})|^2\rangle$ that shows a neat plateau at $kL \ll 1$ (notice the linear scale on the vertical axis).

The statistics of θ is typically super-Gaussian [2]: its probability density function has exponential-like tails even for a Gaussian, δ correlated in time driving force f. Indeed, in the latter case it can be shown exactly, by a minor modification of the arguments given in Ref. [10], that θ is the product of two independent random variables $\theta \stackrel{\Delta}{=} \phi\sqrt{F_0 T}$ where ϕ is a Gaussian variable of zero mean and unit variance, F_0 is the average injection rate of scalar fluctuations, and T is a positive-defined random variable, independent from ϕ. The variable T is essentially the time taken by a spherical blob of minute initial size to disperse across a length L for a given flow configuration [11]. Therefore $\langle\theta^{2n}\rangle/\langle\theta^2\rangle^n = (2n-1)!!\langle T^n\rangle/\langle T\rangle^n \geq (2n-1)!!$; i.e., θ is super-Gaussian unless T is nonrandom. The distribution of θ_r is super-Gaussian as well; however, as r increases above the forcing correlation length, the probability density of θ_r tends to a Gaussian distribution, as it is clearly seen by the scale dependence of the distribution flatness and hyperflatness (see Fig. 2).

Within the framework of Gibbs statistical equilibrium, the scalar field has vanishingly small correlations above the scale L: therefore one could view θ_r as the sum of $N \approx (r/L)^2$ independent random variables (identically distributed as θ) divided by N. By central-limit-theorem arguments [12], the moments of order $2n$ of the coarse-grained scalar field (odd-order moments vanish by symmetry) should then scale as N^{-n}, giving $\langle(\theta_r)^{2n}\rangle \sim \langle\theta^2\rangle^n \times (r/L)^{-2n}$. This is a very good estimate for $n = 1$: indeed, as shown in Fig. 3, the product $(r/L)^2\langle\theta_r^2\rangle$ has a very neat plateau. This is consistent with the fast decay of the two-point scalar correlation $\langle\theta(\boldsymbol{x},t)\theta(\boldsymbol{x}+\boldsymbol{r},t)\rangle$ at $r \gtrsim L$. Indeed, in this case the second-order moment $\langle\theta_r^2\rangle = \int d\boldsymbol{y}_1 d\boldsymbol{y}_2 G_r(\boldsymbol{y}_1 - \boldsymbol{x})G_r(\boldsymbol{y}_2 - \boldsymbol{x})\langle\theta(\boldsymbol{y}_1,t)\theta(\boldsymbol{y}_2,t)\rangle$ is dominated by contributions with $|\boldsymbol{y}_1 - \boldsymbol{y}_2| \lesssim L$ yielding $\langle\theta_r^2\rangle \sim \langle\theta^2\rangle(r/L)^{-2}$. Alternatively, by Fourier transforming the

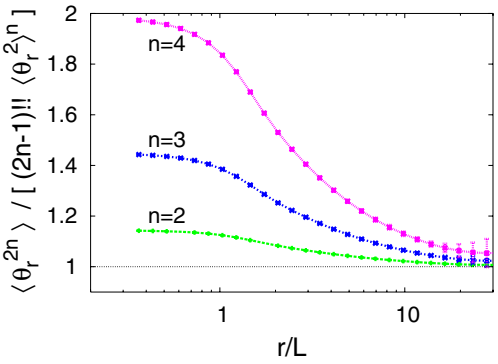

FIG. 2 (color online). The flatness and hyperflatness of the coarse-grained scalar field as a function of r/L, normalized by their Gaussian values $(2n-1)!!$. For $r \to 0$ the curves tend to the flatness factors of the field θ: the numerical values correspond to a super-Gaussian probability density function $\ln p(\theta) \sim -\theta^{1.6}$.

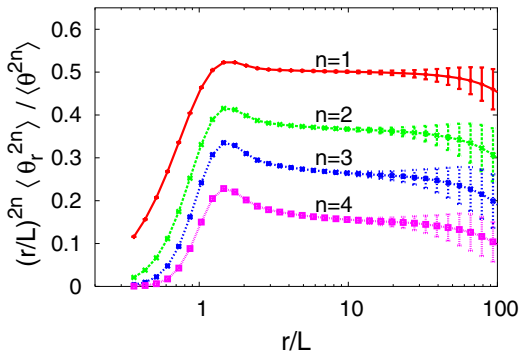

FIG. 3 (color online). Moments of the coarse-grained scalar field $\langle\theta_r^{2n}\rangle$ compensated by the thermal equilibrium expectation $(r/L)^{2n}$. The error bars are determined by dividing the sample in ten subsamples and computing the dispersion around the mean.

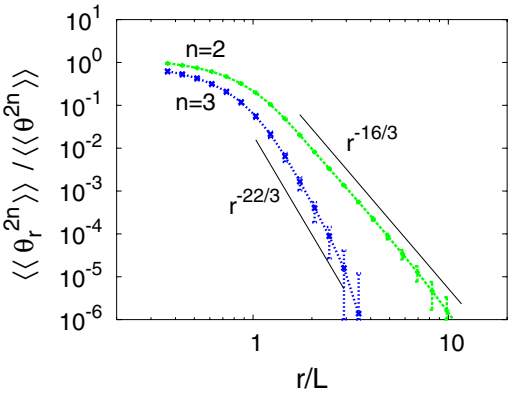

FIG. 4 (color online). Cumulants of order 4 and 6 for the coarse-grained scalar field. The best fits for the slopes give exponents 5.32 ± 0.05 for $n = 2$ and 7.5 ± 0.5 for $n = 3$. The theoretical values $-16/3$ and $-22/3$ are shown for comparison.

coarse-grained field one obtains $\langle\theta_r^2\rangle = \int |\hat{G}_r(\boldsymbol{k})|^2 \times \langle|\hat{\theta}(\boldsymbol{k}, t)|^2\rangle d\boldsymbol{k} \simeq \langle\theta^2\rangle(r/L)^{-2}$, since the transformed filter $\hat{G}_r(\boldsymbol{k})$ is close to unity for $kr \ll 1$ and falls off very rapidly for $kr \gtrsim 1$, and $|\hat{\theta}(\boldsymbol{k}, t)|^2 \simeq \langle\theta^2\rangle/(\pi L^2)$. In summary, two-point statistics appears to be consistent with Gibbs equilibrium ensemble. The situation for multipoint correlations will turn out to be different.

A careful inspection of higher-order moments shows a less good agreement with central-limit-theorem estimates (see Fig. 3): this points to the existence of subleading contributions to the moments $\langle\theta_r^{2n}\rangle$ for $n > 1$ arising from long-range correlations of multiple scalar products. In order to quantify more precisely the rate of convergence to Gaussianity and its relationship to long-range correlations, it is useful to consider the cumulants of the random variable θ_r. According to the central-limit theorem [12], the cumulant of order $2n$ should vanish with N^{-2n+1} leading to an expected scaling $\langle\langle\theta_r^{2n}\rangle\rangle \sim \langle\langle\theta^{2n}\rangle\rangle(r/L)^{-4n+2}$. Let us reiterate that the former expression is expected to be valid in absence of scalar correlations across length scales $r \gtrsim L$.

For $n = 1$ we have $\langle\langle\theta_r^2\rangle\rangle = \langle\theta_r^2\rangle$ whose behavior has been already detailed above. In Fig. 4 we show the behavior of $\langle\langle\theta_r^4\rangle\rangle = \langle\theta_r^4\rangle - 3\langle\theta_r^2\rangle^2$ and $\langle\langle\theta_r^6\rangle\rangle = \langle\theta_r^6\rangle - 15\langle\theta_r^2\rangle \times \langle\theta_r^4\rangle + 30\langle\theta_r^2\rangle^3$. For the fourth-order cumulant, we observe a scaling law very close to the theoretical expectation $\langle\langle\theta_r^4\rangle\rangle \simeq \langle\langle\theta^4\rangle\rangle(r/L)^{-16/3}$ obtained in Ref. [3] for $\gamma = 2/3$, which corresponds to Kolmogorov-Richardson scaling for the velocity dynamics. This has to be contrasted with the scaling law $(r/L)^{-6}$ given by central-limit arguments. The breakdown of the central-limit theorem is due to the existence of long-range dynamical correlations in the range $r \gg L$. These exclude the possibility of a true Gibbs statistical equilibrium at large scales. The leading contribution to the fourth-order cumulant $\langle\langle\theta_r^4\rangle\rangle = \int d\boldsymbol{y}_1 \times d\boldsymbol{y}_2 d\boldsymbol{y}_3 d\boldsymbol{y}_4 G_r(\boldsymbol{y}_1 - \boldsymbol{x}) G_r(\boldsymbol{y}_2 - \boldsymbol{x}) G_r(\boldsymbol{y}_3 - \boldsymbol{x}) G_r(\boldsymbol{y}_4 - \boldsymbol{x}) \times \langle\langle\theta(\boldsymbol{y}_1, t)\theta(\boldsymbol{y}_2, t)\theta(\boldsymbol{y}_3, t)\theta(\boldsymbol{y}_4, t)\rangle\rangle$ comes from configurations with the four points arranged in two pairs of close particles (e.g., $|\boldsymbol{y}_1 - \boldsymbol{y}_2| \lesssim L$ and $|\boldsymbol{y}_3 - \boldsymbol{y}_4| \lesssim L$) separated by a distance r (e.g., $|\boldsymbol{y}_1 - \boldsymbol{y}_3| \simeq r$). Otherwise stated, two-point correlators of the squared scalar field $\langle\langle\theta^2(\boldsymbol{x}, t)\theta^2(\boldsymbol{x} + \boldsymbol{r}, t)\rangle\rangle$ must display a nontrivial scaling $(r/L)^{-4/3}$. We will get back to the issue of the statistics of θ^2 momentarily. The sixth-order cumulant $\langle\langle\theta_r^6\rangle\rangle$ is extremely difficult to measure because of the strong cancellations between various terms. Upon collecting the statistics over about ten thousand scalar correlation times, we can conclude that the results are consistent with the power-law decay $\langle\langle\theta_r^6\rangle\rangle \simeq \langle\langle\theta^6\rangle\rangle(r/L)^{-22/3}$ suggested by the theory for $\gamma = 2/3$, and arising from terms like $\langle\langle\theta_r^4\rangle\rangle \times \langle\langle\theta_r^2\rangle\rangle$ that appear in the expansion of the sixth-order cumulant [3]. The actual exponent for $\langle\langle\theta_r^6\rangle\rangle$ cannot be de-

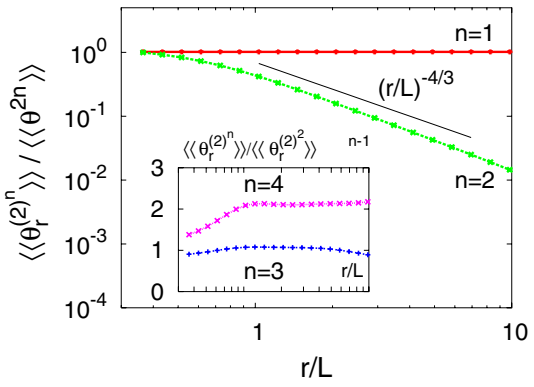

FIG. 5 (color online). Cumulants of the coarse-grained, squared scalar field $\theta_r^{(2)}$. The definitions for the low-order cumulants of a generic random variable z are: $\langle\langle z\rangle\rangle = \langle z\rangle$, $\langle\langle z^2\rangle\rangle = \langle z^2\rangle - \langle z\rangle^2$, $\langle\langle z^3\rangle\rangle = \langle z^3\rangle - 3\langle z\rangle\langle z^2\rangle + 2\langle z\rangle^3$, $\langle\langle z^4\rangle\rangle = \langle z^4\rangle - 4\langle z\rangle\langle z^3\rangle - 3\langle z^2\rangle^2 + 12\langle z^2\rangle\langle z\rangle^2 - 6\langle z\rangle^4$.

PRL 94, 214503 (2005) PHYSICAL REVIEW LETTERS week ending 3 JUNE 2005

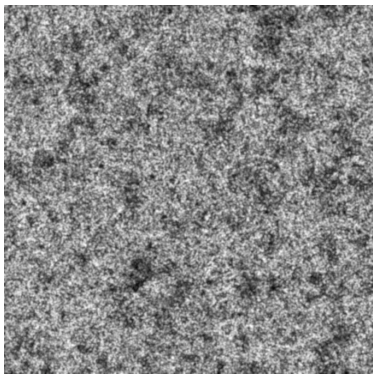

FIG. 6. A snapshot of the squared scalar field θ^2. Remark the inhomogeneous distribution of scalar intensity originating from long-range correlations $\langle\langle\theta_r^{(2)^2}\rangle\rangle \sim r^{-4/3}$.

termined with great precision, yet it lies within the range between -7 and -8, thus definitely different from the central-limit-theorem expectation, -10.

Further insight on the deviations from statistical equilibrium at large scales can be gained by studying the statistics of the coarse-grained squared scalar field

$$\theta_r^{(2)}(\boldsymbol{x}, t) = \int G_r(\boldsymbol{x} - \boldsymbol{y})\theta^2(\boldsymbol{y}, t)d\boldsymbol{y}. \tag{3}$$

The cumulants of $\theta_r^{(2)}$ give useful information about the presence of long-range correlations of the field θ^2. The first-order cumulant $\langle\langle\theta_r^{(2)}\rangle\rangle \equiv \langle\theta_r^{(2)}\rangle$ is trivially equal to $\langle\theta^2\rangle$. The second-order cumulant $\langle\langle\theta_r^{(2)^2}\rangle\rangle = \langle\theta_r^{(2)^2}\rangle - \langle\theta_r^{(2)}\rangle^2$ for a scalar field in thermal equilibrium should decay rapidly to zero at large scales $r \gtrsim L$. On the contrary, as shown in Fig. 5, we observe a slow power-law decay with an exponent close to the theoretical expectation (for $\gamma = 2/3$) $\langle\langle\theta_r^{(2)^2}\rangle\rangle \simeq \langle\langle\theta^4\rangle\rangle(r/L)^{-4/3}$ [3].

Higher-order cumulants behave self-similarly as $\langle\langle\theta_r^{(2)^n}\rangle\rangle \sim \langle\langle\theta_r^{(2)^2}\rangle\rangle^{n-1}$. This result can be interpreted in terms of the geometrical properties of the positive measure defined by the squared scalar field: at scales $r \gtrsim L$ the field θ^2 appears as a purely fractal object with dimension $D_F \approx 2/3$ (see Fig. 6) onto a space-filling background.

We end up by discussing the physical origin of long-range scalar correlations. For a Gaussian forcing we have $\theta^2(\boldsymbol{x}_1, t)\theta^2(\boldsymbol{x}_2, t) \overset{\Delta}{=} F_0^2\phi_1^2\phi_2^2T_1T_2$. At distances $|\boldsymbol{x}_1 - \boldsymbol{x}_2| = r \gg L$ the two Gaussian variables ϕ_1 and ϕ_2 are independent. However, this is not the case for T_1 and T_2 because of the underlying velocity field. Therefore, the long power-law tail for $\langle\langle\theta_r^{(2)^2}\rangle\rangle$ arises from events where $\langle T_1T_2\rangle \gg \langle T\rangle^2$. This amounts to say that two blobs of initial size smaller than L, released at a distance $r \gg L$ in the same flow, do not spread considerably by turbulent diffusion (i.e., $T_{1,2} \gg \langle T\rangle$) with a probability $\sim(r/L)^{-4/3}$.

In summary, we have shown that the scenario of Gibbs statistical equilibrium is not valid for large-scale passive scalar turbulence in spite of the absence of scalar flux. Long-range correlations appear at the level of high-order cumulants of the coarse-grained scalar field. It would be extremely interesting to understand whether the breakdown of ''thermal equilibrium'' holds for other turbulent systems as well, in particular, for two and three-dimensional hydrodynamic turbulence at very large scales.

We acknowledge illuminating discussions with G. Falkovich and A. Fouxon. This work has been supported by the EU under the contract HPRN-CT-2002-00300. Numerical simulations have been performed at CINECA (INFM parallel computing initiative).

[1] G. Falkovich, K. Gawędzki, and M. Vergassola, Rev. Mod. Phys. **73**, 913 (2001).
[2] Z. Warhaft, Annu. Rev. Fluid Mech. **32**, 203 (2000).
[3] G. Falkovich and A. Fouxon, Phys. Rev. Lett. **94**, 214502 (2005).
[4] H. Kellay and W. Goldburg, Rep. Prog. Phys. **65**, 845 (2002).
[5] P. Tabeling, Phys. Rep. **362**, 1 (2002).
[6] L. Smith and V. Yakhot, Phys. Rev. Lett. **71**, 352 (1993).
[7] G. Boffetta, A. Celani, and M. Vergassola, Phys. Rev. E **61**, R29 (2000).
[8] A. Celani, A. Lanotte, A. Mazzino, and M. Vergassola, Phys. Rev. Lett. **84**, 2385 (2000); A. Celani and M. Vergassola, Phys. Rev. Lett. **86**, 424 (2001).
[9] G. Boffetta and A. Celani, Physica (Amsterdam) **280A**, 1 (2000); P. Castiglione and A. Pumir, Phys. Rev. E **64**, 056303 (2001).
[10] A. Celani and D. Vincenzi, Physica (Amsterdam) **172D**, 103 (2002).
[11] U. Frisch, A. Mazzino, A. Noullez, and M. Vergassola, Phys. Fluids **11**, 2178 (1999).
[12] The statistics of the random variable $z_N = (\Sigma_i^N w_i)/N$, where w_i are independent and identically distributed random variables with zero mean and finite variance σ^2, is completely characterized by the generating function $G(s) = \langle\exp(sz_N)\rangle$. By virtue of statistical independency and identity in distribution of the w's, we have $G(s) = \langle\prod_i^N \exp(sw_i/N)\rangle = \langle\exp(sw/N)\rangle^N = g(s/N)^N$ where g is the generating function for w. For $N \gg 1$ we have $g(s/N) \simeq (1 + s^2\sigma^2/(2N^2))^N \simeq \exp s^2\sigma^2/(2N)$ (a version of the central-limit theorem) and therefore $\langle z_N^{2n}\rangle \simeq (2n - 1)!!\sigma^{2n}N^{-n}$. The cumulants $\langle\langle z_N^{2n}\rangle\rangle$ are defined in terms of the Taylor series of $\ln G(s)$ around $s = 0$: since $\ln G(s) = N\ln g(s/N)$ we have $\langle\langle z_N^{2n}\rangle\rangle \sim \langle\langle w^{2n}\rangle\rangle N^{-2n+1}$.

PRL 96, 184501 (2006) PHYSICAL REVIEW LETTERS week ending 12 MAY 2006

Large-Scale Anisotropy in Scalar Turbulence

Antonio Celani[1] and Agnese Seminara[1,2]

[1]*INLN, CNRS, 1361 Route des Lucioles, 06560 Valbonne, France*

[2]*Dipartimento di Fisica, Università degli Studi di Genova, and INFN Sezione di Genova, Via Dodecaneso 33, 16100 Genova, Italy*

(Received 27 March 2006; published 12 May 2006)

The effect of anisotropy on the statistics of a passive tracer transported by a turbulent flow is investigated. We show that under broad conditions an arbitrarily small amount of anisotropy propagates to the large scales where it eventually dominates the structure of the concentration field. This result is obtained analytically in the framework of an exactly solvable model and confirmed by numerical simulations of scalar transport in two-dimensional turbulence.

DOI: 10.1103/PhysRevLett.96.184501 PACS numbers: 47.27.−i

The emergence of large-scale anisotropy arising from small-scale sources is a phenomenon that spans the most diverse fields of physics. For instance, the microscopic anisotropy of crystals in mantle rocks in the Earth's interior is believed to induce large-scale seismic anisotropy [1], and some small anisotropic perturbation in an early cosmological era, evolving through gravitational collapse, is thought to be responsible for the large-scale anisotropy of the cosmic microwave background radiation [2]. Conversely, in statistical physics, microscopic details such as lattice anisotropies may be wiped out by the dynamics allowing a recovery of symmetry and universality at large scales [3]. In the theoretical and experimental analysis of turbulence much attention has been devoted to the anisotropy of the fine scales of fluid motion (see, e.g., Ref. [4] and references therein). Here, we take a different viewpoint and investigate the effect of anisotropy on the large-scale statistics of turbulence. In this Letter we show how, unexpectedly, breaking rotational invariance by an arbitrarily small amount at a given scale induces a strong anisotropy on the large scales, and symmetry is never restored.

We consider the evolution of a passive tracer described by a concentration field $\theta(\boldsymbol{x}, t)$ and transported by a turbulent flow $\boldsymbol{v}(\boldsymbol{x}, t)$

$$\partial_t \theta + \boldsymbol{v} \cdot \boldsymbol{\nabla} \theta = \kappa \Delta \theta + f, \tag{1}$$

where $\boldsymbol{v}$ is an incompressible, statistically homogeneous, and isotropic velocity field. The external driving f is the source of scalar field fluctuations acting at a characteristic scale l_f. The turbulent cascade toward small scales produces fine-scale structures of concentration that are eventually smeared out by diffusion at scales $r_d \ll l_f$, resulting in a statistically stationary state where input and dissipation are in balance on average. The pumping mechanism can be chosen so as to introduce a certain degree of anisotropy, that propagates across scales and may, in principle, pervade the system. However, the disordered motion of fluid particles induced by the underlying turbulent, isotropic medium, might be sufficient to restore rotational invariance at scales far below or above l_f. Indeed, this is the case at small scales $r \ll l_f$, where it can be shown that the dominant contribution to the statistics of the scalar field θ is isotropic [4]. At large scales $r \gg l_f$, since no upscale cascade of scalar fluctuations occurs, *a fortiori* one would expect an essentially isotropic concentration field. On the contrary, here we give theoretical and numerical evidence that large-scale statistics is dominated by the anisotropic contribution under very broad conditions. We show the following. (i) The correlation function $\langle \theta(\boldsymbol{r}, t)\theta(\boldsymbol{0}, t)\rangle$ at scales $r \gg l_f$ is dominated by its anisotropic component decaying as a power law with an anomalous scaling exponent, as opposed to the exponential fall-off of the isotropic part. This result is obtained analytically in the framework of the exactly solvable Kraichnan model and its validity for realistic flows is demonstrated by numerical simulations of passive scalar advection in the inverse cascade of two-dimensional turbulence. (ii) Large-scale anisotropy manifests itself in the concentration field with the appearance of ''pearl necklace'' structures aligned with the preferential direction imposed by the microscopic anisotropy. (iii) The loss of isotropy at large scales can be interpreted as a breakdown of equilibrium Gibbs statistics for the anisotropic degrees of freedom. (iv) In the Lagrangian interpretation of passive scalar transport the emergence of anisotropic power-law decay of correlation is associated to a long-lasting memory of the initial orientation of particle pairs advected by the flow.

Let us first consider the Kraichnan model of passive scalar advection (see, e.g., Ref. [5] for a thorough review), where $\boldsymbol{v}$ is a Gaussian, self-similar, incompressible, statistically homogeneous and isotropic, white-in-time, d-dimensional velocity field. Its statistics are characterized by the correlation $S_{\alpha\beta}(\boldsymbol{r})\delta(t) = \langle [v_\alpha(\boldsymbol{r}, t) - v_\alpha(\boldsymbol{0}, t)][v_\beta(\boldsymbol{r}, 0) - v_\beta(\boldsymbol{0}, 0)]\rangle = 2Dr^\xi[(d + \xi - 1)\delta_{\alpha\beta} - \xi r_\alpha r_\beta / r^2]\delta(t)$. The exponent ξ measures the degree of roughness of the velocity field and lies in the range $0 < \xi < 2$, the two extremes corresponding to Brownian diffusion and smooth velocity, respectively. The assumption of δ correlation is of course far from being realistic, yet it has the remarkable advantage of leading to closed equations

PRL 96, 184501 (2006) PHYSICAL REVIEW LETTERS week ending 12 MAY 2006

for equal-time correlation functions. In the following it will be sufficient to focus on the two-point correlation function $C(\boldsymbol{r}) = \langle\theta(\boldsymbol{r}, t)\theta(\boldsymbol{0}, t)\rangle$. In the limit of vanishing diffusivity $\kappa \to 0$ and in the statistically stationary state, C obeys the partial differential equation $\mathcal{M}C(\boldsymbol{r}) = -F(\boldsymbol{r})$ where $\mathcal{M} = \frac{1}{2}S_{\alpha\beta}(\boldsymbol{r})\frac{\partial}{\partial r_\alpha}\frac{\partial}{\partial r_\beta}$. Here F is the correlation function of the Gaussian, white-in-time, statistically stationary, homogeneous, anisotropic forcing $\langle f(\boldsymbol{r}, t)f(\boldsymbol{0}, 0)\rangle = F(\boldsymbol{r})\delta(t)$. At scales $r \lesssim l_f$ it equals the average input rate of scalar and then decays rapidly to zero, e.g., exponentially, as $r \gg l_f$. By virtue of the statistical isotropy of the velocity field, the operator $\mathcal{M}$ assumes a particularly simple form in radial coordinates: $\mathcal{M} = D[(d-1)r^{1-d}\partial_r r^{d-1+\xi}\partial_r + (d+\xi-1)r^{\xi-2}\mathcal{L}^2]$ where $\mathcal{L}^2$ is the d-dimensional squared angular momentum operator. It is then convenient to decompose the correlation functions on a basis of eigenfunctions of angular momentum $\mathcal{L}^2 Y_j = -j(j+d-2)Y_j$ with positive integer j. The shorthand notation $Y_j(\hat{\boldsymbol{r}})$, where $\hat{\boldsymbol{r}} = \boldsymbol{r}/r$, does not account for degeneracies and stands for the trigonometric functions in $d = 2$ and the spherical harmonics in $d = 3$. Accordingly, we define the components of the correlation functions in the jth anisotropic sector as $C(\boldsymbol{r}) = \sum_j C_j(r)Y_j(\hat{\boldsymbol{r}})$ and similarly for $F(\boldsymbol{r})$, where C_j and F_j depend on $r = |\boldsymbol{r}|$ only. This yields a system of uncoupled differential equations in the radial variable for each anisotropic component $\mathcal{M}_j C_j(r) = -F_j(r)$, where $\mathcal{M}_j = D[(d-1)r^{1-d}\frac{d}{dr}r^{d-1+\xi}\frac{d}{dr} - j(j+d-2)(d+\xi-1)r^{\xi-2}]$, that can be solved in each sector j. The resulting $C_j(r)$ is a linear combination of a particular solution determined by $F_j(r)$, and a homogeneous one $Z_j(r)$, a "zero mode." It is easy to see that the former behaves as $r^{2-\xi+j}$ for $r \ll l_f$ (recall that $F_j \sim r^j$ at small r if F is analytic in the neighborhood of $r = 0$) and that it must fall off exponentially fast for $r \gg l_f$, as dictated by the decay of F_j. The homogeneous solutions are $Z_j^{\pm}(r) = r^{\zeta_j^{\pm}}$ with scaling exponents $\zeta_j^{\pm} = \frac{1}{2}\times[-d+2-\xi \pm \sqrt{(d-2+\xi)^2 + 4\frac{j(j+d-2)(d+\xi-1)}{d-1}}]$. The zero mode with positive scaling exponent ζ_j^+ appears at small scales whereas the zero mode with negative scaling exponent ζ_j^- is relevant in the range $r \gg l_f$. In order to fully characterize the large-scale behavior of the correlation function, it is necessary to identify the prefactor appearing in front of the homogeneous solution. This can be accomplished by writing the equation for C_j in integral form: $C_j(r) = \int_0^\infty G_j(r, \rho)F_j(\rho)d\rho$, where $G_j(r, \rho)$ is the kernel of $-\mathcal{M}_j^{-1}$, i.e., the solution of $\mathcal{M}_j G_j(r, \rho) = -\delta(r-\rho)$. The explicit form is $G_j(r, \rho) = A(\rho)Z_+^j(r)Z_-^j(\rho)$ for $r < \rho$ and $G_j(r, \rho) = A(\rho)Z_-^j(r)Z_+^j(\rho)$ for $r > \rho$, with $A(\rho) = \rho^{d-1}/[D(\zeta_j^+ - \zeta_j^-)]$. Plugging this expression in the integral form for the correlation function yields a large-scale behavior $C_j(r) \approx Q_j Z_j^-(r)$ + exponentially decaying terms. The quantity $Q_j = \int_0^\infty A(\rho)Z_+^j(\rho)F_j(\rho)d\rho$ is of crucial importance and plays the role of a "charge" in analogy with electrostatics [6]. In the isotropic sector $j = 0$, it reduces to $Q_0 = \frac{\Gamma(d/2)}{2\pi^{d/2}D(d-2+\xi)}\int F(\boldsymbol{r})d\boldsymbol{r}$. When the isotropic charge $Q_0 \neq 0$, the leading behavior at large scales is isotropic, $C(\boldsymbol{r}) \sim C_0(r) \sim Q_0 r^{-d+2-\xi}$. The most interesting situation is when $Q_0 = 0$, corresponding to the broad class of forcings localized in wave number space ($Q_0 \propto \hat{F}(\boldsymbol{k} = \boldsymbol{0})$). In this event, there is no power-law contribution from the isotropic zero mode and therefore the isotropic part of the correlation function is characterized by an exponential decay at large r [6,7]. In the anisotropic sectors, it appears immediately that there is no reason to expect a null charge and the generic situation is $Q_j \neq 0$ for $j > 0$ (see Ref. [8]). As a result, the large-scale correlation is dominated by the anisotropic contribution arising from the zero mode, $C(\boldsymbol{r}) \sim r^{\zeta_j^-}Y_j(\hat{\boldsymbol{r}})$, that largely outweighs the exponentially small isotropic part. Among the various contributions arising from different sectors, the leading one corresponds to the lowest nonzero j excited by the forcing, typically $j = 2$ (odd j's are switched on only by breaking reflection invariance).

For the sake of illustration, we show in Fig. 1 an instance of a scalar field corresponding to the simple case of Kraichnan advection by a very rough velocity ($\xi = 0$), in $d = 2$ and with $Q_0 = 0$. Large-scale anisotropy manifests itself in the appearance of "pearl necklaces" made of like-sign scalar patches of size $\sim l_f$. These are aligned along the preferred direction of the forcing and extend for a length $\gg l_f$.

It is worth pointing out the relationship between the appearance of anisotropic, anomalous scaling in the large-scale behavior of the scalar correlation function and

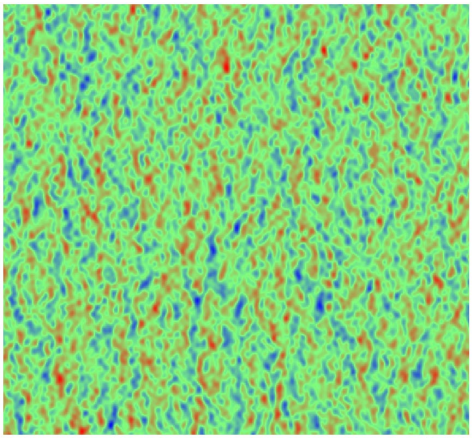

FIG. 1 (color online). Image of a scalar field for the Kraichnan model at $\xi = 0$, $d = 2$, $Q_0 = 0$, $Q_2 \neq 0$. The width of a single scalar patch is $\sim l_f$. Forcing is preferentially acting in the vertical direction. Here $C_0(r) \sim e^{-r^2/l_f^2}$ and $C_2(r) \sim r^{-2}$ at $r \gg l_f$.

equilibrium statistics. At large scales, because of the absence of scalar flux, the system could be expected to be in equilibrium and obey Gibbs statistics. In physical space this corresponds to a concentration field organized in independently distributed scalar patches of size l_f. As recently shown in Refs. [6,7], this is not true and substantial deviations are observed at the level of multipoint correlation functions already in the isotropic case. This departure has been traced back to the existence of nontrivial zero modes in that case as well. In the present case the breakdown of Gibbs statistics has an even more dramatic manifestation since it occurs already for two-point correlation functions, i.e., at the level of the spectral distribution of concentration. We now rephrase the previous findings in terms of the averaged scalar spectral density, i.e., the Fourier transform of the correlation function, $\hat{C}(\boldsymbol{k}) = \langle|\hat{\theta}(\boldsymbol{k}, t)|^2\rangle$, and its decomposition in angular sectors in wave number space $\sum_j \hat{C}_j(k) Y_j(\hat{\boldsymbol{k}})$, where $\hat{\boldsymbol{k}} = \boldsymbol{k}/k$. For a correlation function decaying exponentially to zero at large r, representative of large-scale equipartition in physical space, the spectral density is analytic in a neighborhood of $k = 0$. In the series for $\hat{C}(\boldsymbol{k})$ the harmonic $Y_j(\hat{\boldsymbol{k}})$ appears only in the powers of $\boldsymbol{k}$ of order $\geq j$, yielding the long wavelength behavior $\hat{C}_j^{(\mathrm{eq})}(k) \sim k^j$. This defines the equipartition spectrum for generic anisotropic fluctuations. However, because of the appearance of nontrivial zero modes in the anisotropic sectors the actual spectral density contains also a contribution $\hat{C}_j^{(\mathrm{zero})}(k) \sim k^{-d-\zeta_j^-}$ that is responsible for the power-law decay of correlations in physical space with $j > 0$. For the Kolmogorov-Richardson value $\xi = 4/3$ and the sector $j = 2$ the anomalous spectrum always dominates the equipartition contribution in spectral space as well ($-d - \zeta_{j=2}^- < 2$ for all $\xi < 3/2$).

It is useful to reinterpret the results obtained so far within the framework of the Lagrangian interpretation of passive scalar transport. The correlation function can be generically written as $C(\boldsymbol{r}) = \int T(\boldsymbol{\rho}|\boldsymbol{r}) F(\boldsymbol{\rho}) d\boldsymbol{\rho}$ where $T(\boldsymbol{\rho}|\boldsymbol{r}) d\boldsymbol{\rho}$ is the average time spent at a separation $\boldsymbol{\rho} + d\boldsymbol{\rho}$ by a pair of particles that end their trajectories at a separation $\boldsymbol{r}$. In the Kraichnan model T is the kernel of the operator $-\mathcal{M}^{-1}$. Since the action of the forcing is restricted to scales $\sim l_f$, the large-scale behavior of the correlation function is essentially dominated by the ensemble of trajectories that have spent in the past a sufficiently long time at a short distance $\rho \lesssim l_f \ll r$. When r/ρ tends to infinity T becomes independent of ρ and we obtain $T \sim r^{-d+2-\xi}$ [9]. The dependency on the final orientation $\hat{\boldsymbol{r}}$ is also lost. This leads to the estimate $C(r) \sim Q_0 r^{-d+2-\xi}$. However, as noticed previously, when $Q_0 = 0$ the isotropic part of the correlation function receives only exponentially small contributions from the forcing in the range $\rho \sim r \gg l_f$. Let us now turn our attention to the anisotropic part of the correlation function. Projecting $C(\boldsymbol{r})$ over $Y_j(\hat{\boldsymbol{r}})$ for $j > 0$ amounts to giving different weights, positive and negative, to particle pairs oriented in different directions $\hat{\boldsymbol{r}}$. Therefore C_j can be interpreted as a difference of times spent at $\rho \lesssim l_f$ by differently oriented pairs. The first key point is that the trajectories preserve a long-lasting memory of their initial orientation, with a slow power-law decay in r that reflects in the behavior of the correlation function. Indeed, it can be shown that in the Kraichnan model $T(\boldsymbol{\rho}|\boldsymbol{r}) = \sum_j b_j r^{\zeta_j^-} \rho^{\zeta_j^+} Y_j(\hat{\boldsymbol{r}}) Y_j(\hat{\boldsymbol{\rho}})$ for $r > \rho$. Plugging this expression in the integral form of the correlation function gives the result $C_j(r) \sim Q_j r^{\zeta_j^-}$ as above. Here emerges the second important point, i.e., the dependence of T on ρ: differently oriented trajectories sample the forcing unevenly in scales as $\rho \sim l_f$ and this results in a nonvanishing charge Q_j for $j > 0$.

A remarkable advantage of the Lagrangian interpretation is that it does not make appeal to the special features of the Kraichnan model. This suggests that the same mechanisms are at work for realistic turbulent flows as well, and this expectation has been repeatedly confirmed for different aspects of passive scalar transport [7,10,11]. Here we show that anisotropy dominates the large-scale statistics for real flows by showing the results of a numerical investigation of passive scalar transport in the inverse cascade of two-dimensional Navier-Stokes turbulence. This flow has been studied in great detail, both experimentally in fast flowing soap films [12] and in shallow layers of electromagnetically driven electrolyte solutions [13,14], and numerically [15–17]. The velocity field $\boldsymbol{v}$ is statistically homogeneous, isotropic, and scale-invariant with exponent $h = 1/3$ ($\delta_r v \sim r^h$) in the range $l_f^v \lesssim r \lesssim L_v$, where l_f^v denotes the kinetic energy injection length and L_v the velocity integral scale. The scalar field is governed by Eq. (1) driven by a homogeneous, anisotropic, Gaussian, δ-correlated driving f that excites the sectors $j = 0$ and $j = 2$ and satisfies the condition of null isotropic charge (see Ref. [8]). The various length scales are ordered as follows: $l_f^v \ll r_d \ll l_f \ll L_v$. In Fig. 2 we show the spectral content of scalar fluctuations $E_j(k) = \pi^{-1} k \int_0^{2\pi} \cos(j\phi_k) \hat{C}(\boldsymbol{k}) d\phi_k = k\hat{C}_j(k)$ at $kl_f < 1$, i.e., at large scales. The isotropic spectrum ($j = 0$) agrees very well with the Gibbs equilibrium distribution, $E_{j=0}(k) \propto k$, and corresponds to exponentially decreasing isotropic correlation at large scales (see the main frame of Fig. 3) in agreement with the theoretical arguments presented above. The anisotropic spectrum shows a power-law behavior $E_{j=2}(k) \sim k^{2.2\pm0.1}$ definitely dominating over the equilibrium spectrum $E_{j=2}^{\mathrm{eq}}(k) \sim k^3$. In physical space, this translates into a power-law decay of the anisotropic correlation function $C_{j=2}(r)$, as shown in the main frame of Fig. 3, and leads to the estimate $\zeta_{j=2}^- \simeq -3.2 \pm 0.1$. Therefore, the correlation function at large scales is dominated by the anisotropic power-law decay for 2D Navier-Stokes advection as well. Finally, we notice that for incompressible, time-reversible, self-similar flows the two zero-mode exponents are conjugated by the dimensional rela-

PRL 96, 184501 (2006) PHYSICAL REVIEW LETTERS week ending 12 MAY 2006

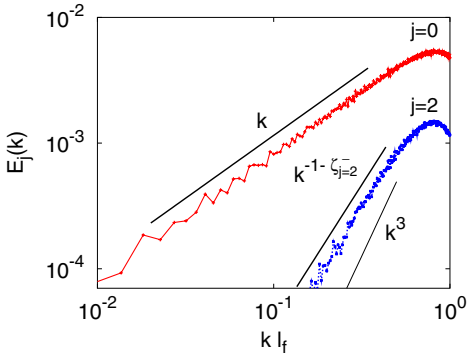

FIG. 2 (color online). Simulations of passive scalar advection by two-dimensional Navier-Stokes turbulence in the inverse cascade (for details see Ref. [7]). Here are shown the spectra $E_j(k)$ of concentration in the isotropic ($j = 0$) and anisotropic ($j = 2$) sectors. The spectral slopes are 1.0 ± 0.05 and 2.2 ± 0.1, respectively, ($\zeta^-_{j=2} = -3.2$). The equilibrium spectra k and k^3 are also shown for comparison.

tion $\zeta^+_j + \zeta^-_j = -d + 1 - h$ (within the Kraichnan model $1 - h = 2 - \xi$, due to the δ correlation in time). In the inset of Fig. 3 we show the behavior of the correlation function $C_{j=2}(r) \sim r^{\zeta^+_j}$ at small scales $r \ll l_f$ that indeed displays an exponent $\zeta^+_j = 1.8 \pm 0.1$ compatible with the previous relation [18].

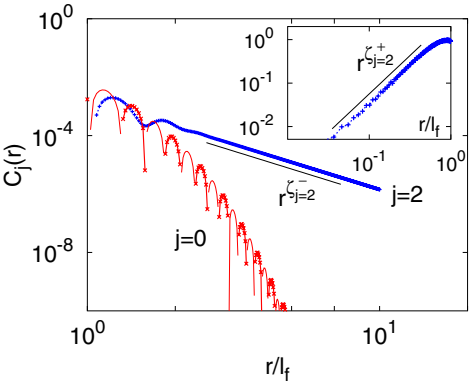

FIG. 3 (color online). Main frame: Correlation functions $C_j(r)$ at large scales $r \gtrsim l_f$ for $j = 0$ and $j = 2$. Notice the exponential decay of the isotropic part as opposed to the power-law behavior of the anisotropic component. In order to limit the statistical noise at large values of r/l_f these two curves have been obtained by interpolating the spectra shown in Fig. 2 at small k as power laws k and $k^{-1-\zeta^-_{j=2}}$, respectively, and computing the correlation function from the integral $C_j(r) = \int_0^\infty J_j(kr)E_j(k)/k dk$. Here $\zeta^-_{j=2} = -3.2$. Inset: Correlation function $C_{j=2}(r)$ at small scales $r \lesssim l_f$. The solid line is $r^{\zeta^+_{j=2}}$ with $\zeta^+_{j=2} = 1.8$.

In summary, we have shown that microscopic anisotropies introduced by the forcing have a dramatic imprint on the large-scale statistics of passive scalar turbulence. From this result new questions arise naturally, the most intriguing one being whether the large scales of hydrodynamic turbulence show such striking properties as well. Further theoretical, experimental, and numerical effort in this direction is needed to elucidate this point.

This work has been partially supported by the EU Contract No. HPRN-CT-2002-00300 and by CNRS PICS 3057.

[1] P. G. Silver, Annu. Rev. Earth Planet Sci. **24**, 385 (1996).
[2] E. F. Bunn, P. G. Ferreira, and J. Silk, Phys. Rev. Lett. **77**, 2883 (1996).
[3] J. Cardy, *Scaling and Renormalization in Statistical Physics* (Cambridge University Press, Cambridge, England, 1996).
[4] L. Biferale and I. Procaccia, Phys. Rep. **414**, 43 (2005).
[5] G. Falkovich, K. Gawędzki, and M. Vergassola, Rev. Mod. Phys. **73**, 913 (2001).
[6] G. Falkovich and A. Fouxon, Phys. Rev. Lett. **94**, 214502 (2005).
[7] A. Celani and A. Seminara, Phys. Rev. Lett. **94**, 214503 (2005).
[8] A simple example is given by the following choice of anisotropic driving in $d = 2$: the spectral density of the forcing $\hat{F}(k, \phi_k) = \pi^{-1}k^2 l_f^4 \exp(-k^2 l_f^2/2)\sin^2\phi_k$ results in a forcing correlation function that excites the two sectors $j = 0, 2$ only: $F(r, \phi) = F_0(r) + F_2(r)\cos(2\phi)$, where $F_0(r) = 2[1 - r^2/(2l_f^2)]\exp[-r^2/(2l_f^2)]$ and $F_2(r) = -(r/l_f)^2 \exp[-r^2/(2l_f^2)]$. The resulting charges are $Q_0 = (D\xi)^{-1}\int_0^\infty f_0(r) r dr \propto \int_0^\infty r[1 - r^2/(2l_f^2)] \times \exp[-r^2/(2l_f^2)]dr = 0$ and $Q_2 = (\sqrt{2}l_f)^{2+\zeta^+_2}\Gamma(2 + \zeta^+_2/2)/[D(\zeta^+_2 - \zeta^-_2)] \neq 0$.
[9] D. Bernard, K. Gawędzki, and A. Kupiainen, J. Stat. Phys. **90**, 519 (1998).
[10] A. Celani, A. Lanotte, A. Mazzino, and M. Vergassola, Phys. Rev. Lett. **84**, 2385 (2000).
[11] A. Celani and M. Vergassola, Phys. Rev. Lett. **86**, 424 (2001).
[12] H. Kellay and W. Goldburg, Rep. Prog. Phys. **65**, 845 (2002).
[13] P. Tabeling, Phys. Rep. **362**, 1 (2002).
[14] M. K. Rivera and R. E. Ecke, Phys. Rev. Lett. **95**, 194503 (2005); S. Chen *et al.*, Phys. Rev. Lett. **96**, 084502 (2006).
[15] L. Smith and V. Yakhot, Phys. Rev. Lett. **71**, 352 (1993).
[16] G. Boffetta, A. Celani, and M. Vergassola, Phys. Rev. E **61**, R29 (2000).
[17] D. Bernard, G. Boffetta, A. Celani, and G. Falkovich, Nature Phys. **2**, 124 (2006).
[18] Notice that, strictly speaking, the assumption of time reversibility for the inverse cascade is incorrect, due to the presence of a kinetic energy flux. However, the almost-Gaussian statistics of velocity (see, e.g., Ref. [16]) suggests that it is a good approximation.

Bibliography

[1] E. BALKOVSKY, G. FALKOVICH, V. LEBEDEV and M. LYSIANSKY. Large-scale properties of passive scalar advection. *Phys. Fluids*, **11(8)** 2269-2279, (1999).

[2] E. BALKOVSKY, G. FALKOVICH, V. LEBEDEV and I. SHAPIRO. Large-scale properties of wave turbulence. *Phys. Rev. E*, **52(4)** 4537-4540, (1995).

[3] D. BERNARD, K. GAWEDZKI and A. KUPIAINEN. Anomalous scaling in the n-point functions of a passive scalar. *Phys. Rev. E*, **54** 2564-2572, (1996).

[4] D. BERNARD, K. GAWEDZKI and A. KUPIAINEN. Slow modes in passive advection. *Journ. Stat. Phys.*, **98(3-4)** 519-569, (1998).

[5] L. BIFERALE and I. PROCACCIA. Anisotropy in turbulent flows and in turbulent transport. *Phys. Rep.*, **414(2-3)** 43-164, (2005).

[6] G. BOFFETTA and A. CELANI. Pair dispersion in turbulence. *Physica(Amsterdam)*, **280(A)** 1-9, (2000).

[7] G. BOFFETTA, A. CELANI and M. VERGASSOLA. Inverse energy cascade in two-dimensional turbulence: Deviations from gaussian behavior. *Phys. Rev. E*, **61** R29-R32, (2000).

[8] E. F. BUNN, P. G. FERREIRA and J. SILK. How anisotropic is our universe? *Phys. Rev. Lett.*, **77** 2883-2886, (1996).

[9] P. CASTIGLIONE and A. PUMIR. Evolution of triangles in a two-dimensional turbulent flow. *Phys. Rev. E*, **64** 056303, (2001).

[10] A. CELANI, A. LANOTTE and A. MAZZINO. Passive scalar intermittency in compressible flow. *Phys. Rev. E*, **60** R1138-R1141, (1999).

[11] A. CELANI, A. LANOTTE, A. MAZZINO and M. VERGASSOLA. Fronts in passive scalar turbulence. *Phys. of Fluids*, **13(6)** 1768-1783, (2001).

[12] A. CELANI and M. VERGASSOLA. Statistical geometry in scalar turbulence. *Phys. Rev. Lett.*, **86(3)** 424-427, (2001).

[13] S. CHEN and R. H. KRAICHNAN. Simulations of a randomly advected passive scalar field. *Phys. Fluids*, **68** 2867-2884, (1998).

[14] M. CHERTKOV and G. FALKOVICH. Anomalous scaling exponents of a white-advected passive scalar. *Phys. Rev. Lett.*, **76** 2706-2709, (1996).

[15] M. CHERTKOV, G. FALKOVICH, I. KOLOKOLOV and V. LEBEDEV. Normal and anomalous scaling of the fourth-order correlation function of a randomly advected passive scalar. *Phys. Rev. E*, **52** 4924-4941, (1995).

[16] M. CHERTKOV, G. FALKOVICH, I. KOLOKOLOV and V. LEBEDEV. Statistics of the passive scalar advected by a large-scale two-dimensional velocity field: Analytic solution. *Phys. Rev. E*, **51** 5609-5627, (1995).

[17] G. FALKOVICH and A. FOUXON. Anomalous scaling of passive scalar in turbulence and in equilibrium. *Phys. Rev. Lett.*, **94** 214502, (2005).

[18] G. FALKOVICH, K. GAWEDZKI and M. VERGASSOLA. Particles and fields in fluid turbulence. *Rev. Mod. Phys.*, **73(4)** 913-975, (2001).

[19] D. FORSTER, D. R. NELSON and M. J. STEPHEN. Large-distance and long-time properties of a randomly stirred fluid. *Phys. Rev. A*, **16** 732-749, (1977).

[20] U. FRISCH. *Turbulence. The legacy of A. N. Kolmogorov*. Cambridge University Press, Cambridge, (1995).

[21] U. FRISCH, A. MAZZINO and M. VERGASSOLA. Intermittency in passive scalar advection. *Phys. Rev. Lett.*, **80** 5532-5535, (1998).

[22] O. GAT, I. PROCACCIA and R. ZEITAK. Anomalous scaling in passive scalar advection: monte carlo lagrangian trajectories. *Phys. Rev. Lett.*, **80** 5536-5539, (2001).

[23] K. GAWEDZKI and A. KUPIAINEN. Anomalous scaling of the passive scalar. *Phys. Rev. Lett.*, **75** 3834-3837, (1995).

[24] C. GIBSON, C. FREIHE and S. McCONNELL. Structure of shear turbulent fields. *Phys. Fluids*, **20** 156-167, (1977).

[25] JAYESH and Z. WARHAFT. Probability distributions of a passive scalar in grid generated turbulence. *Phys. Rev. Lett.*, **67** 3503-3506, (1991).

[26] H. KELLAY and W. GOLDBURG. Two-dimensional turbulence: a review of some recent experiments. *Rep. Prog. Phys.*, **65** 845-894, (2002).

[27] R. H. KRAICHNAN. Small-scale structure of a scalar field convected by turbulence. *Phys. Fluids*, **11(5)** 945-953, (1968).

[28] R. H. KRAICHNAN. Convection of a passive scalar by a quasi-uniform random straining field. *J. Fluid Mech.*, **64** 937-762, (1974).

[29] R. H. KRAICHNAN. Anomalous scaling of a randomly advected passive scalar. *Phys. Rev. Lett.*, **72** 1016-1019, (1994).

[30] P. G. MESTAYER. Local isotropy and anisotropy in a high-reynolds-number turbulent boundary layer. *J. Fluid Mech.*, **125** 475-503, (1982).

[31] L. MYDLARSKY, A. PUMIR, B. I. SHRAIMAN, E. D. SIGGIA and Z. WARHAFT. Structure and multi-point correlators for turbulent advection. *Phys. Rev. Lett.*, **81** 4373-4376, (1998).

[32] F. PASQUILL and F. B. SMITH. *Atmospheric diffusion*. Ellis Horwood, (1983).

[33] B. I. SHRAIMAN and E. D. SIGGIA. Anomalous scaling of a passive scalar in turbulent flow. *C. R. Acad. Sci. Série II*, **321** 279-284, (1995).

[34] B. I. SHRAIMAN and E. D. SIGGIA. Scalar turbulence. *Nature*, **405** 639-646, (2000).

[35] P. G. SILVER. Seismic anisotropy beneath the continents: probing the depths of geology. *Annu. Rev. Earth Planet. Sci.*, **24** 385-432, (1996).

[36] L. SMITH and V. YAKHOT. Bose condensation and small-scale structure generation in a random force driven 2d turbulence. *Phys. Rev. Lett.*, **71** 352-355, (1993).

[37] K. R. SREENIVASAN. On local isotropy of passive scalars in turbulent shear flows. *Proc. R. Soc. Lond. A*, **434** 165-182, (1991).

[38] K. R. SREENIVASAN and R. A. ANTONIA. The phenomenology of small scales turbulence. *Annu. Rev. Fluid Mech.*, **29** 435-472, (1997).

[39] P. TABELING. Two-dimensional turbulence: a physicist approach. *Phys. Rep.*, **362** 1-62, (2002).

[40] Z. WARHAFT. Passive scalars in turbulent flows. *Annu. Rev. Fluid Mech.*, **32** 203-240, (2000).

Part III

Turbulent transport of condensing droplets

Introduction

This part of the thesis is devoted to the problem of condensation/evaporation in turbulent flows, that I treated theoretically and numerically. The growth or decrease of droplet size by condensation/evaporation of surrounding vapor molecules is relevant for the most diverse fields, spanning from physics [18] to engineering [30] and medicine [17]. When being inhaled through the respiratory tract, many types of droplets undergo size changes due to evaporation or condensation [28]. This is the case for certain types of medicinal drug nanocrystals assumed by inhalation. Hygroscopicity can substantially increase their size and this strongly affects their deposition along the highly complicated structures of human respiratory system [4]. Therefore, a correct dose assessment of such size-changing particles requires a detailed analysis of transport and size-dependent deposition in human airways.
The investigation of this effect is also very important in clinical studies for treating pulmonary disorders. Exposure to atmospheric particulate or pollutant are the possible cause for inhalation of toxic particles. Some of them are highly volatile and are subjected to a dramatic size decrease for evaporation [29]. The local particle deposition patterns, depending on particle size, seem to play a crucial role in the development of lung cancer [3]. Note that in conditions of light activity breathing, the inspiratory flow undergoes local transitions to turbulence and this may play a role in the process.
As another instance, this general problem is relevant for an important technological issue such as the development of spark-ignition engines. These are designed to inject gasoline droplets directly into the combustion chamber and can substantially improve fuel economy and reduce hydrocarbon emissions. A high level of turbulence is essential for enhancing the fuel-air mixing and the rate of fuel vaporization [30].

Though applied in a completely different framework, the same idea has a long history in cloud physics as well. Turbulence in clouds is a spectacular phenomenon which cannot be disregarded when approaching the problem of rain formation. The non-linear coupling of the dynamics at different scales coincides with a strongly out of equilibrium transport mechanism providing a local structure of the fields definitely non-trivial. I explored the problem by means of direct numerical simulations of turbulent transport of micro droplets and a vapor field. A correlation mechanism between droplets and vapor emerged, showing that a mean-field-type theory would not capture essential features of the dynamics. Namely, a mean droplet growth can establish also in the presence of a vapor field with zero average. A spreading of droplet-size distribution is observed, although a first look at the evolution equation of droplet radius would promise narrowing. The basic mechanisms emerged are direct consequences of turbulent transport and can be relevant for the long-standing problem of the bottleneck of condensation in warm clouds.
Warm clouds are huge natural laboratories where interactions of the most diverse nature

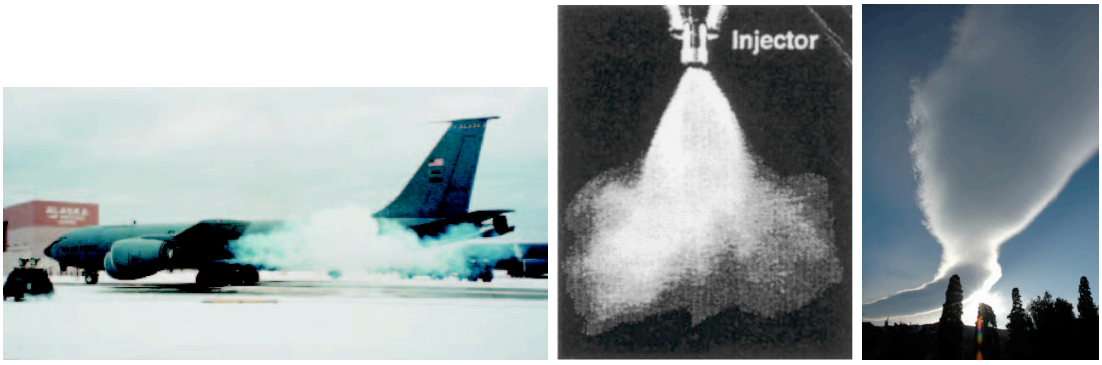

Figure 9: Turbulent condensation/evaporation in different physical systems. From left to right: typical exhaust plume from an engine run-up procedure, releasing unburnt and partially burnt toxic particulate dangerous for the ground personnel; engine injector of fuel droplets; water droplets in warm clouds.

occur: chemistry, microphysics, thermodynamics and electrostatics, all play important roles in the development of clouds and precipitation. The approach I adopt here does not aim to reproduce exactly the conditions of a real cloud. Rather, I strip bare the system to some basic ingredients: small droplets and condensing water vapor advected by a turbulent flow. From their formation onto tiny solid particles (cloud condensation nuclei) droplets must grow of more than three orders of magnitude in size, from $\approx 1\mu m$ to a few mm, in order to become raindrops. To bridge this gap, two main physical mechanisms are available in warm clouds. The first one is condensation, dominant immediately after droplet formation. Later, when droplets become sufficiently large, collisions become relevant and droplets undergo a much faster growth. Although collisions are much more efficient than condensation, this efficiency depends on the preceding stage. Hence the crucial importance of condensation for rain formation. In particular, since the probability of collisions due to gravity is proportional to the velocity difference between the two colliding droplets, it turns out that a population of identical droplets would collide seldom and would be eventually unable to produce rain. This wrong expectation is exactly what one obtains on the basis of a mean-field type analysis of the condensation equation. The narrowing of droplet size spectrum (the bottleneck of condensation) is a theoretical problem that must be solved in order to understand the efficiency of rain formation. Moreover, broad droplet size distributions have been detected in very broad conditions by *in situ* measurements in warm clouds. My suggestion is that such broadening can be ascribed to turbulence.

In this part of the thesis I focus on the role of turbulent transport for the problem of droplet condensation/evaporation in moist environment. I was mainly concerned with the application of this general issue to cloud physics that will be discussed in detail. In chapter 1 I will describe the formation and evolution of warm clouds, so to provide background information useful to put the problem in the context. In chapter 2 I present the results I obtained in the framework of condensation in turbulent environment with particular attention for cloud physics. I will dedicate a final paragraph to describe my recent interest in the problem of fuel droplet evaporation, now in progress.

Chapter 1

Cloud physics

The first attempts to cloud classification and rudimentary measurements date back to the 19th century. The first complete cloud-atlas was published in 1896 after 20 years of joint work [19]. This early attention to the variety of clouds gives an idea of how complex and rich this natural phenomenon is. Although they have been object of a long attention, clouds present a few long-standing problems which are still poorly understood at now. Of course, the progress in the experimental techniques has been huge, allowing for a much more detailed description of the conditions in clouds. The dramatic advances in aviation and the increased use of aircraft during the second world war were major improvements with respect to the early 19th century balloon flights toward the atmosphere[1]. However, small-scales measurements in clouds still remain a challenging task for experimental physics. On the other hand, the recent fast progress in computer resources allows to handle demanding simulations and provide an alternative tool to investigate cloud physics.
Cloud physics poses a number of unanswered questions whose relevance cannot be underestimated due to its paramount importance for climate changes, as assessed by the recent reports of the Intergovernmental Panel on Climate Change (IPCC).

What are the huge systems we are used to see just looking up to the sky? Warm clouds (where temperature is around $20\,^{\circ}\mathrm{C}$ and no ice is present) are basically composed by

[1] It is commonly accepted that the earliest balloon flight to explore the atmosphere was made from London to Kent, the 30th November 1784 by Dr. John Jeffries [5]

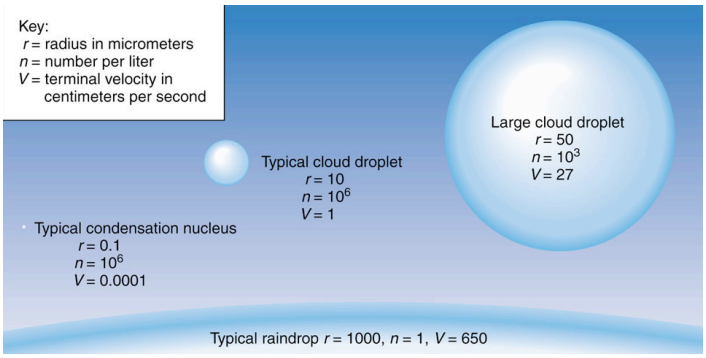

Figure 1.1: A schematic picture of a cloud condensation nucleus, two cloud droplets at different stages of their evolution and a raindrop.

droplets of different sizes and tiny solid particles suspended in a moist air (see figure 1.1). A strong turbulent flow transports these basic elements and builds the huge natural systems where precipitations originate. In the sequel I describe the evolution of a rain droplet from formation until precipitation.

1.1 Nucleation

The most naïve way to imagine droplet formation, is what is called *homogeneous nucleation*: water vapor molecules, coming together at random, spontaneously condense in a micro-droplet. This is a transition from a disordered state of vapor molecules to a more ordered state of liquid water organized in a droplet. The system undergoes this transition only if the final state is energetically favored with respect to the initial one. In other words, in order for the droplet to be stable the volume energy coming from the phase change of vapor into water, must fulfill the surface energy required to build the droplet. To meet this requirement droplets must exceed a critical size. In the same random way as they form, homogeneous droplets generally evaporate and disappear, in typical cloud conditions. Note that the value of the critical radius is finite only when there is vapor available for condensation, i.e. in a *supersaturated* environment (see equation (2.2) and successive discussion). This means that if the environment is poor of vapor, the formation of a droplet is never energetically favored.

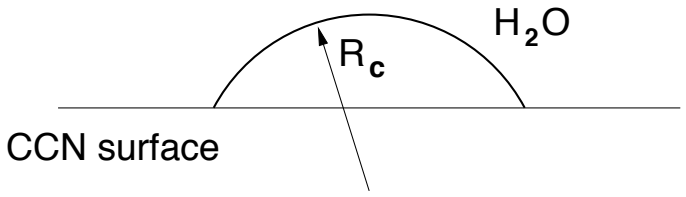

Figure 1.2: Sketch of the geometrical advantage of heterogeneous nucleation. The curvature radius achieved by a certain amount of vapor molecules condensing onto the CCN surface is larger than the radius of the sphere composed by the same amount of vapor molecules.

In order for homogeneous nucleation to justify the density of droplets in a warm cloud, supersaturation should be of the order of 400% whereas it is around 1% in typical cloud

conditions. Droplets form, instead, by *heterogeneous nucleation*, onto the surface of solid particles called cloud condensation nuclei (CCN). Due to their chemical composition these solid particles catalyze the random condensation of vapor molecules and modify the geometry of the process allowing for a more effective aggregation (see Figure 1.1). Once the spherical water layer completes the CCN is activated and the droplet is formed. Large, soluble CCN are the most likely to be activated. The electro-chemical properties and size distributions of CCN have been long studied and well described for different clouds so that this first stage of droplet life is very-well understood [18].
Recently, much attention has been devoted to CCN. Indeed, their density is enhanced by anthropogenic emissions, whose effects are of crucial importance for global warming and climate changes. The problem is fairly complex, since an enhanced concentration of CCN in the atmosphere has two opposite effects on the global temperature. From one side they extend the cloud cover, that screens Earth from solar radiation thus decreasing its temperature. On the other hand, the direct interaction of CCN with solar radiation seems to result in an overall warming, thus making the net effect uncertain [11, 14]. However, the *a posteriori* observations after volcanic eruptions indicate an immediate cooling, thus hinting to the possibility that, at least for certain chemical compositions of the CCN, the screening effect would prevail on the warming one. When Mount Pinatubo in the Philippines erupted in 1991 the huge plume of sulfur cooled the Earth by 0.5 degree Celsius the following year (see figure 1.3). Recently, the Nobel prize Paul Crutzen [6] has opened the debate on the possibility to artificially enhance earth's albedo and thereby cooling the planet by injecting particles of sulfur into the stratosphere. Another reason of interest in CCN is in that their concentration can influence the initiation time of precipitation. Therefore an artificial control of CCN concentration could in principle modify the rain-initiation time [8].

Figure 1.3: Image of the second largest volcanic eruption of the twentieth century. Mount Pinatubo, June 1991, Philippines.

1.2 Condensation

Once formed, droplets begin their path to become raindrops. This typically takes less than half an hour in real clouds. The remarkable efficiency of precipitation formation is poorly

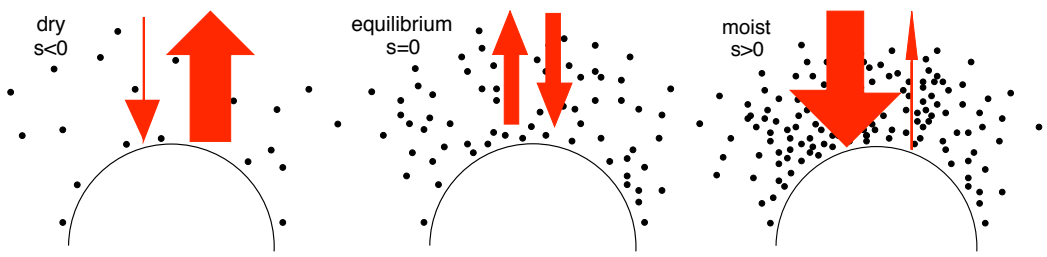

Figure 1.4: Schematic representation of condensation/evaporation in the presence of a vapor field. In the first figure on the left there is less vapor than at the saturation point ($s < 0$). Evaporation of water molecules from the droplet is favored with respect to vapor condensation. Adding some vapor molecules (or cooling them), equilibrium is reached ($s = 0$). A further addition of vapor moves the dynamical equilibrium toward condensation ($s > 0$).

understood at now. Indeed, since the typical size of a CCN is less than $1\,\mu m$, droplet radius evolution must cover more than 3 orders of magnitude in order to produce $2\,mm$-sized raindrops. To tackle this problem, let us begin by following the single-droplet evolution.
After the CCN has been completely covered by water, the vapor molecules keep diffusing on droplet surface and grow the droplet by condensation. The typical time of diffusion over droplet surface is much less than the typical time of condensation and of the smallest turbulent scale in the atmosphere (see [25]). Hence the detailed characterization of the vapor-field variation over droplet surface is generally avoided, in favor of a mean-field type description. A detailed comparison of the temporal scales (associated with the diffusion of water vapor molecules on droplet surface and with the changes in the ambient conditions related to turbulence) reveals that this approximation is valid for droplets smaller than $20\,\mu m$ in radius for typical cloud conditions (see [25]). Mass and energy conservations coupled with the steady diffusion equation over a spherical droplet with radius R give the well-known equation of radius evolution:

$$\frac{dR}{dt} = A_3 \frac{s}{R} \tag{1.1}$$

where A_3 is a function of thermodynamic variables and parameters (see e.g. [18]) and s is the *supersaturation*. The latter quantifies the amount of vapor available for condensation, i.e. the fraction of vapor that exceeds the saturation point (see figure 1.4). It is defined by:

$$s = \frac{e}{e_s} - 1 \tag{1.2}$$

where e and e_s are the vapor pressure and the saturation vapor pressure respectively. Where s is negative the quantity of vapor randomly condensing is not sufficient to compensate the quantity of liquid water randomly evaporating. The net effect is that the droplet evaporates. In the opposite case, where s is positive, there are more vapor molecules than at the equilibrium, and the net effect is their condensation onto droplet surface, hence droplet growth. Supersaturation computation requires the knowledge of the thermodynamic environment surrounding the droplet. This is a very hard information to obtain by *in situ* measurements. On the other hand, a model for the supersaturation evolution requires a characterization of transport and thermodynamics in the atmosphere.
The most simple model for supersaturation evolution in a fluid parcel rising with velocity w

is the well-known Twomey's model [23]. By differentiating equation (1.2) with respect to time one obtains the rate of change of the supersaturation as a function of the derivative of the vapor tension and of the saturation vapor tension. By Clausius-Clapeyron equation, energy conservation and the perfect-gas state equation one can reduce $\dot{e}$ and $\dot{e}_s$ to functions of the time derivatives of the pressure p the absolute temperature T and of the water-vapor mixing ratio $q_v = m_v/m_a$ (m_v and m_a being respectively the mass of water vapor and liquid water in the volume). By assuming a quasi-hydrostatic scheme for the vertical structure of temperature and pressure, one finally obtains:

$$\frac{ds}{dt} = A_1 w - A_2 \frac{dq_v}{dt} \tag{1.3}$$

The term of adiabatic cooling, $A_1 w$, describes the decrease in temperature and pressure due to vertical ascent. The combination of these two effects results in a net increase of s with the height. The term $-A_2 dq_v/dt$ is due to the phase change of water and vapor onto droplet surface. This directly modifies the vapor content inside the volume and also exchange latent heat thus modifying the temperature. The constant A_2 accounts for the sum of these two contributions. Note that, in the absence of entrainment (which is the situation I am interested into), the variation of the vapor content that appears in the second term only comes from condensation/evaporation onto the surface of droplets. In this case, the second term in equation (1.3) can be easily translated in a term proportional to s, through equation (1.1):

$$-A_2 \frac{dq_v}{dt} = -\frac{s}{\tau_s} \qquad \tau_s = \frac{4\pi A_2 A_3 \rho_w \langle R \rangle}{V} \tag{1.4}$$

where V is the volume of the parcel and ρ_w is the density of water. I will get back to this issue in chapter 2, where I will generalize equations (1.3) and (1.4) to include turbulence.

1.3 Initiation of collisions: the bottleneck of condensation

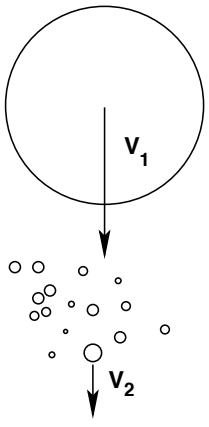

Figure 1.5: Sketch of gravitational collisions. A large, fast drop collide with many smaller and slower droplets during its falling path.

When the droplet achieves a large enough size, its terminal velocity becomes appreciable and the droplet begins its fall. During the path it might collide with other slower droplets (see figure 1.5) or might be caught by a faster droplet above. After the collision, the two droplets might separate and follow their own trajectory, but most probably they coalesce to form a bigger drop.

From this picture it is clear that the gravitational collision efficiency depends on how broad is the size distribution of cloud droplets. Indeed, in the presence of a monodispersed spectrum of droplets, the relative velocity between droplets tends to vanish and no gravitational collisions are possible. In this respect, observations have shown that droplet size spectra in warm clouds are indeed broad. This experimental observation consistently justifies the collision efficiency by indicating the presence of very different droplets. However a theoretical understanding of how broad spectra can be obtained by condensation is still lacking. Indeed, by simply looking at equation (1.1) one realizes that, as soon as the particle grows, the rate of growth decreases. If every droplet is exposed to the same value of supersaturation, this immediately implies that small droplets reach the large ones very fast. As a consequence, equation (1.1) in the presence of almost constant supersaturation gives a narrowing of the droplet-size distribution in time. Contrarily, the experimental evidences of broad droplet-size spectra are compelling. Broad spectra have been observed both near the cloud boundaries and in the inner cloud core, in warm clouds as well as in cold clouds. This striking feature of real clouds, that allows for the fast initiation of gravitational collision/coalescence and therefore rain formation, has not been univocally explained. Partial justifications are based on entrainment with dry air [22], on exceptionally broad initial CCN spectra and in particular on the presence of ultra-giant condensation nuclei [13]. The presence of the droplets themselves has been proposed to be source for local fluctuations of the turbulent kinetic energy [12] and of the vapor field [20] thus providing fluctuations in the environmental conditions.

Of course, in a turbulent medium, gravitation is not the only source of collisions. The kernel of collisions receives substantial contributions coming from turbulence [7, 10]. The effect of turbulence can enhance droplet density by the well-known preferential concentration of inertial particles [16, 21]. Caustic events are another mechanism of enhancement of collision efficiency [27].

Besides the problem of collisions that will not be treated here, my research has focused on the effects of turbulence on the droplet size spectra during the condensation stage. The results I obtained are the focus of next chapter.

Chapter 2

Condensation in turbulent flows

In this chapter I present the results I obtained for condensation in turbulent environments. The problem of droplet condensation in turbulence can be treated as general. Its applications range from health care to cloud physics to engineering. I mainly focused on the cloud physics issue that finally resulted in the papers presented in this chapter. I am also developing numerical simulations with laboratory-like settings that can be thus reproduced by experiments in wind tunnels and can be interesting for engineering applications.
The main elements of the analysis are micro droplets and vapor, transported by a turbulent flow. Droplets undergo size changes due to evaporation or condensation of the surrounding water vapor. Turbulent transport significantly influences droplet growth, in that it locally couples droplet trajectories with the vapor field. The goal is to evaluate the role of turbulence for the evolution of droplet size distributions, that are initially considered narrow. I investigated this general question by simulations of turbulent transport of micro droplets and a vapor field. It emerges that droplet trajectories do not sample homogeneously the whole volume. As shown in figure 2.1, droplets are concentrated in moist regions. This is the visible consequence of correlations induced by the underlying turbulent flow. Another consequence of correlation is that the history of each droplet is influenced by a long-lasting memory of the initial vapor condition experienced. This provides a population of droplets with strongly different evolutions and growth histories. From a series of direct numerical simulations I could support this general picture and show robustness with respect to the particular statistical regime of turbulence under consideration.

2.1 A model of condensation

The physical processes involved in the formation and evolution of warm clouds, are the most diverse, spanning from electrostatics, to chemical reactions, to thermodynamics and turbulence. A complete description of the couplings among all the different microscopic actors is beyond the scope of my research. Rather, I focus on a basic model for condensation, that describes the evolution of a vapor field and a lot of droplets transported by a turbulent flow. These basic ingredients already provide a definitely non-trivial behavior that turns out to be quite general. No particular atmospheric conditions are required, no vicinity with the borders of the cloud, no ultra-giant nuclei or particularly broad condensation nuclei spectra. The sole fundamental ingredient is turbulence. Different turbulent regimes do not affect the

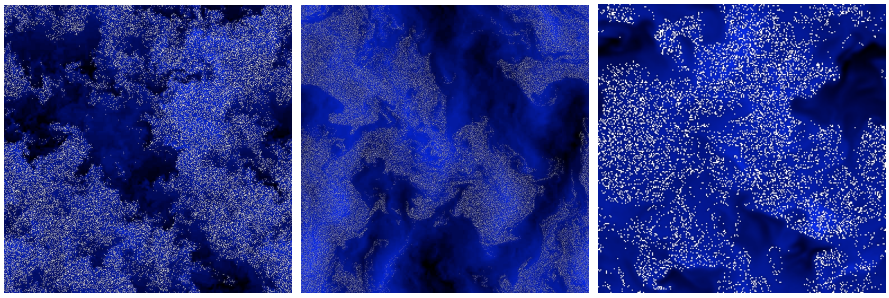

(a) (b) (c)

Figure 2.1: Correlations between droplet trajectories and the supersaturation field. The results have been obtained by DNS of droplet condensation in (a) homogeneous isotropic 2D turbulence (b) Bolgiano 2D convective turbulence and (c) homogeneous isotropic 3D turbulence (in this case the snapshot shows a $L \times L \times 2\eta$ slice of the domain). Details on the simulations are given in the text. Dark blue represents dry regions, light blue represents moist regions. The small white points represent droplet positions after roughly $0.2\tau_L$. Droplets are segregated in moist regions. This indicates the presence of correlations that broaden the droplet size distribution. This mechanism turns out to be qualitatively robust with respect to different statistical regimes.

qualitative results which appear to be robust with the variation of statistics. This general viewpoint essentially allows to highlight basic mechanisms that can be at work in real clouds also, because they are direct consequences of turbulent transport.

The advecting flow is ruled by the Navier-Stokes equations, already introduced in part II:

$$\partial_t \mathbf{v} + \mathbf{v} \cdot \boldsymbol{\nabla} \mathbf{v} = \nu \Delta \mathbf{v} - \boldsymbol{\nabla} \frac{p}{\rho_a} + \mathbf{f}_v + \mathbf{B} \tag{2.1}$$

where ν is the viscosity, p is the pressure, ρ_a is the air density, $\mathbf{f}_v$ is a source of energy fluctuations and $\mathbf{B}$ is buoyancy. For the moment, let us neglect buoyancy and temperature evolution that will be discussed in section 2.3.2. In the absence of buoyancy, equation (2.1) describes a homogeneous isotropic turbulent flow. This scheme is an idealization of the turbulent atmospheric regime. However it is expected to hold in real clouds for the spatial scales that allow to disregard the effect of stratification of the atmosphere. In clouds, this should be valid for spatial scales up to $100\,m$ (see [24]). Recently, a series of works has been published on the small scale structure of atmospheric turbulence and its interactions with droplets' evolution [1, 2, 12, 15]. Due to the lack of small-scale *in situ* measurements of cloud turbulence, these works are based on laboratory experiments in cloud chambers and direct numerical simulations. The general conclusion is that corrections to the above assumptions, mainly for what concerns isotropy, should be considered when focusing on the boundary between cloud and clear air. In the following I will always focus on adiabatic cloud cores, where no boundary effects would be appreciable.

The second ingredient of the model is vapor. In order to solve the radius evolution (1.1) due to condensation/evaporation, we need the supersaturation field, defined by equation (1.2). This quantity has been traditionally considered as a function of time, like in Twomey's model introduced in section 1.2. This was justified by the fact that most of the work was focused on a rising fluid parcel, which is a very small volume (we can imagine a fluid parcel like a cube with a edge of few tens of centimeters). In this respect I generalize the framework

and consider the supersaturation s as a field varying both in space and time. This is a straightforward generalization that allows to consider space correlations, that are typically crucial in turbulence. The simplest generalization of Twomey's model (1.3) is the equation:

$$\partial_t s + \mathbf{v} \cdot \boldsymbol{\nabla} s = k_s \Delta s + A_1 w - \frac{s}{\tau_s} \tag{2.2}$$

where k_s is the diffusivity of water vapor in air and $A_1 \approx 5 \times 10^{-4} m^{-1}$ is the supersaturation gradient, already introduced in section 1.2. The vertical velocity $w = \mathbf{v} \cdot \hat{z}$ is now a turbulent fluctuating field (and not the constant updraft velocity of the parcel model (1.3)). The absorption time τ_s depends now on the number density and radius of the droplets in a small volume V around each point in space:

$$\tau_s^{-1}(\mathbf{x}, t) = \frac{A_2 A_3 \rho_w 4\pi}{V} \sum_{i=1}^{N(V,\mathbf{x})} R_i(t) \tag{2.3}$$

Equations (2.1) and (2.2) are a simple scheme of evolution for the vapor field. In particular the vapor is transported, changes for adiabatic cooling and is directly modified by the presence of droplets. Indeed, where droplets evaporate they release vapor molecules and cool the environment providing a source of supersaturation, while a sink of supersaturation verifies where vapor condense onto droplet surface and release latent heat. Note that we do not describe here the further source of fluctuations coming from the advection-diffusion of temperature. In the derivation of Twomey's model, temperature is implicitely assumed to vary only for adiabatic cooling and latent heat effects.

The final ingredient of the model is the Lagrangian evolution of droplets. I start following droplet evolution right after their activation and abandon the drop before it reaches a size of about $20\,\mu m$ which is typically considered the threshold for the beginning of collision. In this range of sizes, droplets are essentially independent, because collisions are rare[1]. Moreover the low droplet Reynolds number, the low mass fraction of liquid water with respect to air, and the low ratio between droplet radius and the Kolmogorov scale of atmospheric turbulence (typically around $1\,mm$) allow to neglect droplet back reaction on the carrier flow. For a detailed evaluation of these parameters see [24]. Finally, the evolution of droplet trajectory can be described by Stokes drag since the density of water is much larger than the density of air, $\beta = 3\rho_f/(\rho_f + 2\rho_d) \approx 10^{-3}$. Each independent, passive, Stokes particle evolves following:

$$\begin{aligned}
&\frac{d\mathbf{X}(t)}{dt} = \mathbf{V}(t) \\
&\frac{d\mathbf{V}(t)}{dt} = -\frac{\mathbf{V}(t) - \mathbf{v}(\mathbf{X}(t), t)}{\tau_d} + \mathbf{g} \\
&\frac{dR(t)}{dt} = A_3 \frac{s(\mathbf{X}(t), t)}{R(t)} \\
&\tau_d = \frac{R^2}{3\nu\beta}
\end{aligned} \tag{2.4}$$

[1] This assumption is generally accepted. However, evaluations of the turbulent collision kernel are highly non-trivial and some recent work hints to the possibility that caustics might occur already during the condensation stage [27].

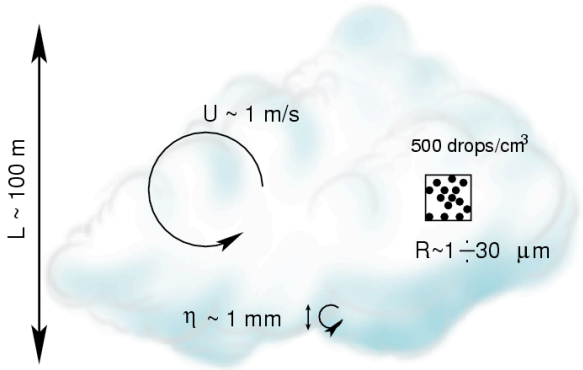

Figure 2.2: Orders of magnitudes of different spatial scales in cloud physics.

2.2 Degrees of freedom: large scales versus small scales

The set of equations composing the simple model described above is a challenging problem, both from an analytic and a numerical point of view. In order to capture the non-trivial correlations that might emerge from the model, I choose a numerical approach. Unfortunately, the number of degrees of freedom in the problem is huge. A schematic picture of this is shown in figure 2.2: the Reynolds number of cloud turbulence can reach values up to $10^7 \div 10^8$, with roughly 6 decades of scales dynamically coupled from about $1\,km$ down to $1\,mm$. The spatial scales of droplet evolution are even smaller, since droplet radii are typically around some microns in the condensation stage. Also, there are a few hundred droplets in a cm^3 of a developed cloud, that sum up to around $10^{15} \div 10^{18}$ droplets in the whole cloud. Clearly, a numerical simulation can describe only a portion of this huge number of degrees of freedom.
A first possibility is to focus on a small portion of the volume describing the small scales of the problem. Direct numerical simulations are the only way to investigate the small scales of atmospheric motion, hence their importance. Indeed, small-scale *in situ* measurements of turbulence in clouds are still unavailable. There are a few recent examples of this viewpoint in literature [2,25,26]. My work began with the observation that, despite its general interest, this approach might be unable to capture interesting features of condensation in turbulent flows. If we take two initially close particles and follow their trajectories, we immediately note an explosive separation due to turbulence. Thus, the first remark is that small-scale simulations oblige droplets to remain close, while their natural behavior would lead them to explore the whole cloud. The further remark is that the environmental conditions that droplets can experience in a cloud are highly variable in space. On the contrary, droplets obliged to remain in a small volume cannot experience these fluctuations and basically evolve all with the same ambient conditions.

2.3 Condensation and turbulence

The guiding idea of my work is that the dramatic fluctuations experienced by droplets inside cloud turbulence may justify the significant spreading of size distributions described in

section 1.2. In order to verify this general idea I performed direct numerical simulations in different settings and highlighted the presence of a robust mechanism for the formation of broad size spectra. Strong fluctuations are typical of large scales and this is the reason why I initially chose to describe a whole cloud instead of a single fluid parcel. Keeping in mind the lesson learned from large scales, I recently modified viewpoint and performed small scales simulations of increasingly larger clouds. This allowed me to draw a trend of the droplet-size spreading and to extrapolate it to obtain the large-scale expectation.

2.3.1 Homogeneous isotropic 2D turbulent transport

I first considered the simplest version of the model equations (2.1), (2.2) and (2.4), in two dimensions, neglecting buoyancy and the droplet back reaction on the vapor field (term $-s/\tau_s$ in equation (2.2)). This finally results in a homogeneous isotropic scheme that holds for adiabatic cloud cores at spatial scales up to around $100\,m$, where turbulent mixing is more important than stratification. As mentioned above, I began by focusing the large scales of the problem. I resolved the spatial scales from $100\,m$ down to roughly $10\,cm$ on a two-dimensional 1024×1024 grid. For smaller scales the turbulent fields were basically smooth.
In this large volume, I followed the trajectories and radii of thousands of droplets, initially put at random with uniform probability in the volume. Since I could not consider the huge number of droplets typical of cloud conditions, the sink of water vapor onto droplet surface was basically negligible (and this is the reason why I neglected the term $-s/\tau_s$ in equation (2.2)). The main result of this set of simulations is that I found a remarkable spreading

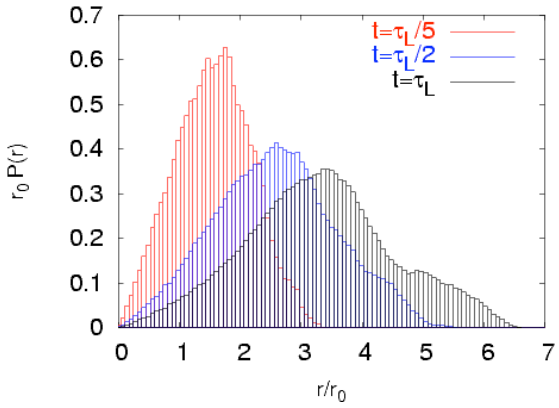

Figure 2.3: Droplet size spectrum evolution obtained by pseudo-spectral DNS of model equations (2.1) with no buoyancy, (2.2) with no droplet-vapor interaction term and (2.4) in two dimensions. Details on the simulations are given in the paper presented below. The particles are initially monodispersed with radius $r_0 = 5\,\mu m$ and positioned at random. After one large-eddy turnover time, roughly 40% of droplets reach a size of $20\,\mu m$.

of size distribution as shown in figure 2.3. After one large-eddy turnover time, roughly 40% of the total population had reached the threshold size for the beginning of collisions.
Besides, I observed that after a small fraction of a large-eddy-turnover time, droplets segregated in moist regions as shown in figure 2.1(a). Indeed, droplets dwelling for long enough in a dry region evaporate completely, leaving dry regions void of particles. The persistence

of droplets in regions with the same vapor content is due to correlations coming from turbulence as both are advected by the same velocity field. Of course segregation can be observed only in the case where correlations of droplet trajectories with the (negative) value of supersaturation last longer than the time needed for droplets to evaporate. Therefore, when droplets become large enough, they need so much time to completely evaporate that they manage to escape from the dry region and segregation disappears. This happens at about one large-eddy turnover time.
This effect suggested the presence of long-lasting correlations between droplet trajectories and supersaturation values. After a detailed analysis of the statistics I could conclude that correlations were actually active and this allowed me to find a reason for the remarkable spreading of size distribution that I observed. Indeed, droplet population can be roughly divided in two parts. Some droplets are initially placed at random in a moist region and remain correlated to high values of supersaturation thus growing fast. Other droplets, correlated to less moist regions, grow slower. At the very bottom we find droplets correlated to very dry regions that, as already discussed above, disappear. This intuitively justify the observed spreading of size distributions. Correlations are also responsible for a mean growth of droplet radii also in the presence of a zero mean supersaturation. Indeed, droplets that survive do not sample the volume at random, but are more probably located in the moist regions. In other words the Lagrangian average of the supersaturation is higher than the Eulerian one. Note that broad size distributions are observed also at local level, so that large and small droplets turn out to be close together.
The results here described have been published in the paper presented at page 97.

2.3.2 Bolgiano 2D convection

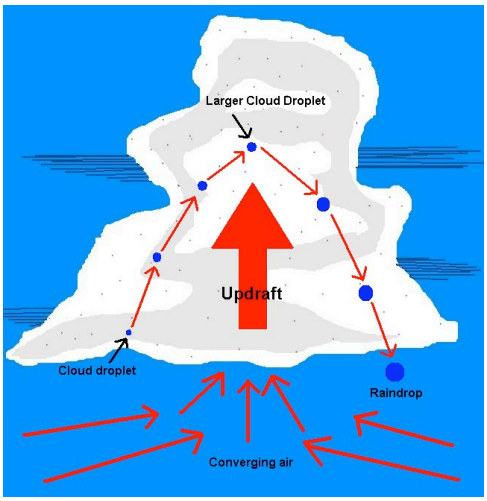

Figure 2.4: Schematic picture of convection and droplet evolution in clouds.

The real dynamics of cloud formation is of course more complex than what described above. In particular, convection is a key point of the large-scale atmospheric circulation (see figure 2.4). The general picture of cloud formation is that cloud condensation nuclei are introduced inside the cloud from below. After being activated, they grow as cloud droplets

while rising toward the top of the cloud. In the case of appropriate conditions, droplets might grow enough during the updraft condensation, and once arrived around the top might begin their fall. In this case, the successive collision/coalescence stage takes place during the fall and the cloud might precipitate.
In order to check the robustness of the qualitative mechanism described for the former case, I consider a more detailed version of the model, introducing convection. I add the evolution of temperature ruled by equation:

$$\partial_t T' + \boldsymbol{v} \cdot \boldsymbol{\nabla} T' = (G - \Gamma_a) w + k_T \Delta T' \tag{2.5}$$

where k_T is the temperature diffusivity, T' are temperature fluctuations with zero mean, while the mean temperature profile is linear with the quote, with gradient G. The term $\Gamma_a w$ is the source of temperature fluctuations coming from adiabatic cooling, Γ_a being the adiabatic lapse rate. Then I consider the coupling of temperature with the velocity field through the Boussinesq scheme (buoyancy in equation (2.1) is $\mathbf{B} = [1 - \alpha(T - T_0)]\hat{z}$), in a two-dimensional Bolgiano regime. Equations for droplet trajectories and radii (2.4) remain unchanged, while I consider equation (2.2), accounting for the term of exchange between water and vapor $-s/\tau_s$. Once more, I focus on the whole cloud, so that to consider the interaction between droplets and vapor I need to renormalize the particle number density. The main conclusion of the work is that the qualitative mechanism of correlation/segregation holds in this case also (see figure 2.1(b)), despite the completely different statistical regime. This is a remarkable feature of the result, since my main point is to convey the idea that, though with different quantitative connotations, this might hold in general conditions.
By accounting for the loss of water vapor onto droplet surface, I obtain an expected slowing down of the condensational growth and spreading (see figure 2.5). Indeed, I consider here the fact that droplets grow absorbing vapor from the surrounding, thus providing a drier and drier environment for their own growth. The final expectation on droplet size spectra broadening results less optimistic and more reasonable for typical cloud conditions.
In this framework, the initial condition for the vapor field is obtained as the stationary state achieved by equations (2.2), (2.1) and (2.5). However, with the initial activation of droplets the stationary state is lost, in favor of a decaying dynamics. Roughly speaking, droplets in moist regions absorb vapor whose loss is not compensated by droplet evaporation, because after a while droplets in dry regions evaporate completely and disappear (giving the same segregation phenomenology observed for the non-convective case). The net effect is that the environment becomes on average undersaturated. The mean radius growth shown in the bottom panel of figure 2.5, is thus even more remarkable, since it lasts despite the mean undersaturation. The results here described have been collected and published in the paper presented at page 105.

2.3.3 Homogeneous isotropic 3D turbulence

As anticipated in the introduction of the present section, I have recently approached the problem with a slighlty different viewpoint. The idea is to describe the effects of the strong turbulent fluctuations on condensation by focusing on small, increasingly larger clouds. In this framework, I performed a series of simulations of equations (2.1) with no buoyancy, (2.2) with the term of interaction droplet-vapor and equations (2.4) for the Lagrangian evolution (details in table 2.1). These allowed me to draw a trend of the size-distribution behavior with

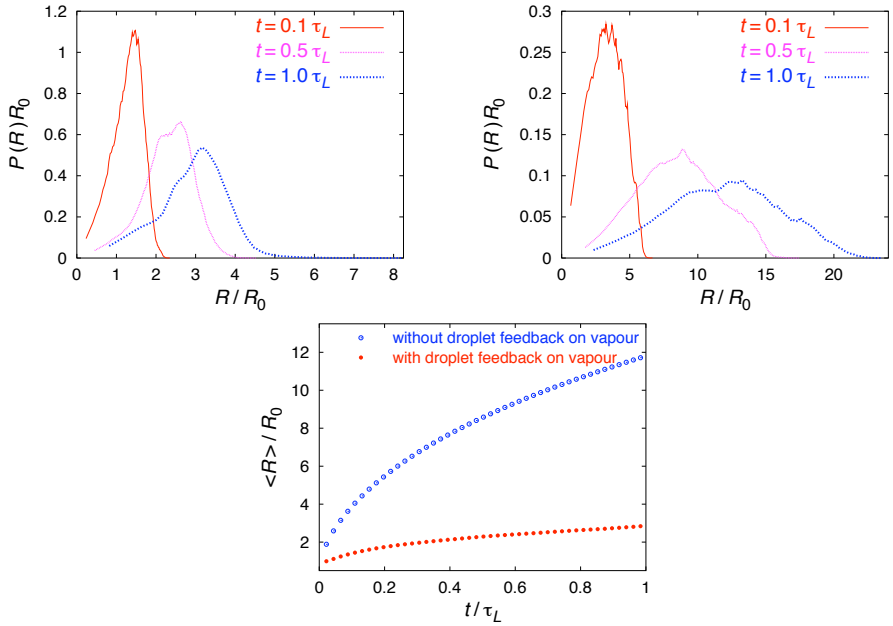

Figure 2.5: Time evolution of the droplet size spectrum obtained by DNS of condensation in 2D Bolgiano convective turbulence for the case of accounted (top left) and neglected (top right) feedback of droplets on vapor. Bottom: time evolution of the mean value of droplet size distribution with accounted (red) and neglected (blue) droplet-vapor interaction. The population of droplets was initially monodispersed with radius $r_0 = 4\,\mu m$. The feedback of droplets on vapor slows down the spreading and the mean growth of the size distribution. The result with no feedback of droplets on vapor gives maximum radii of $85 \div 90 \mu m$ with average $50 \mu m$, while the result accounting for the feedback gives a more reasonable maximum size of $20 \div 22 \mu m$ and average size of $12 \mu m$.

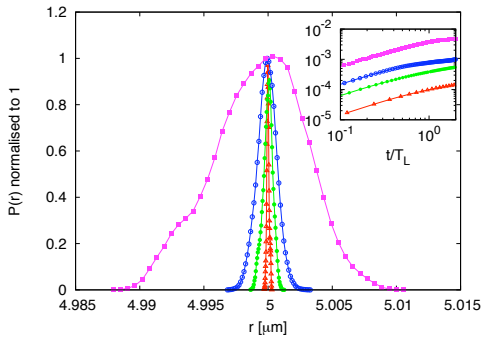

Figure 2.6: Droplet size distribution after τ_L. Results have been obtained through 3D DNS of condensation in homogeneous isotropic turbulence, described in the text. Details on the parameters are given in table 2.1. Red, green, blue and purple lines correspond respectively to simulations (a), (b), (c) and (d). Droplets were initially put randomly with homogeneous distribution in space and monodispersed radius $r_0 = 5 \mu m$. In the inset: evolution of the droplet size variance with time for the four simulations. The color are organized as in the main frame.

the size of the cloud or equivalently with the Reynolds number of cloud turbulence. While the results for each single simulation (see figure 2.6) give a limited degree of spreading, as already pointed out in [25,26], the trend of the latter with Reynolds is a positive power law, pointing to a relevant spreading achieved for sufficiently large clouds. This is due to the fact

	N	L cm	τ_L s	Re_λ	ϵ cm^2/s^3	η cm	τ_η s	$\sigma_s(t=0)$ $\times 10^{-3}\%$	v_{rms} m/s	N_{drops} $\times 10^5$	cpu hours
(a)	64^3	9	2.0	40	10	0.1	0.1	1.5	0.04	0.93	1
(b)	128^3	18	3.5	65	9	0.1	0.1	3.4	0.05	8.2	12
(c)	256^3	38	5.5	105	10	0.1	0.1	6.1	0.07	71	145
(d)	512^3	70	7.6	185	11	0.1	0.1	12	0.1	320	1110

Table 2.1: Parameter of the DNS. From left to right: number of gridpoints N, integral scale L, large-eddy turnover time τ_L, microscale Reynolds number Re_λ, average energy dissipation rate ϵ, Kolmogorov spatial scale η, Kolmogorov timescale τ_η, initial supersaturation standard deviation $\sigma_s(t=0)$, velocity standard deviation v_{rms}, number of droplets N_{drops} and cpu hours per large eddy turnover time.

that droplet radius grows according to the local supersaturation fluctuation experienced on the trajectory. In larger clouds the fluctuations in the vapor field are stronger. Therefore, the radius growth varies more and more from a droplet to another and the size distribution broadens faster and faster.
The spreading of the size distribution after one large-eddy turnover time τ_L is considered as a function of the microscale Reynolds number $Re_\lambda \sim Re^{1/2}$ (see, e.g., [9]). On the basis of equation (1.1), one can roughly estimate the square size broadening as:

$$\sigma(R^2) \sim 2A_3\sigma(s)\tau_L \tag{2.6}$$

The supersaturation field s is initially in a stationary state, whose fluctuations can be simply estimated on the basis of equation (2.2) $\sigma(s) \sim A_1 L \sim Re_\lambda^{3/2}$. By substituting this dimensional relation in equation (2.6) and remembering that τ_L scales as $\tau_L \sim Re_\lambda$, we easily end up with $\sigma(R^2) \sim Re_\lambda^{5/2}$, shown for comparison in figure 2.7. We expect this behavior to be modified when vapor fluctuations start to appreciably decay after the introduction of droplets. Indeed, the latter grow absorbing water vapor from the surrounding. The extrapolation of the power law $Re_\lambda^{5/2}$ to the Reynolds number of real cloud turbulence gives a spreading of around $(25. \pm 3.)\mu m^2$ after $\tau_L \approx 150s$.

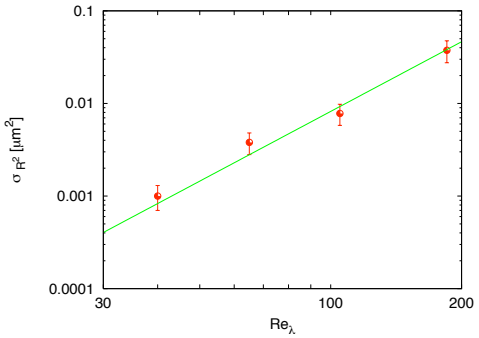

Figure 2.7: Droplet square size distribution standard deviation achieved after one large-eddy turnover time, as a function of the Reynolds number of cloud turbulence. The dashed line is the dimensional prediction $\sigma_{R^2} \propto Re_\lambda^{5/2}$ (see text). The trend of this curve points to a spreading of $(25. \pm 3.)\mu m^2$ after $\tau_L \approx 150\,s$ for a cloud core of size $L \approx 100\,m$ with initial supersaturation fluctuations $s_{rms} \approx 2\%$.

Finally I considered the following point. The broadening mechanism is essentially based

on the fact that droplets experience different ambient conditions. While it is impossible to simulate a flow with the huge inertial range of real cloud turbulence, one can obtain appropriate supersaturation fluctuations by simply tuning the coefficient A_1. This essentially corresponds to simulate the large scales of the problem and is equivalent to what already discussed in section 2.3.1, here applied in a three dimensional context, accounting for the droplet feedback on vapor. Is this enough to obtain the spreading expected on the basis of the small-scales trend? I performed the large scale simulation, tuning the parameters on a cloud core of size $L = 100\,m$. With $N^3 = 256^3$ grid points we are allowed to resolve spatial scales down to $\eta \approx 30cm$. Other typical values are: $v_{rms} \sim 0.6ms^{-1}$, $\sigma_s \approx 2\%$, $N_{drops} = 7. \times 10^6$, $T_L \approx 150\,s$. For large enough supersaturation fluctuations, the segregation mechanism already observed in the two-dimensional case, appears (see figure 2.1(c)). In figure 2.8, the droplet size spectrum after τ_L is shown for this simulation. With the same initially monodispersed spectrum, I obtained a droplet-size spectrum broadening of $\sigma_R(\tau_L) = (1.7 \pm 0.5)\mu m$; $\sigma_{R^2}(\tau_L) = (18. \pm 5.)\mu m^2$, slightly smaller than expected on the basis of the extrapolation described above. This points to the fact that the substantial contribution to the fast droplet size spreading is given by the strong fluctuations of the vapor field, hence the great importance of large-scales. A correction might arise for real cloud turbulence due to the much stronger intermittency with respect to the simulated turbulence. The results here presented have been collected in the paper presented at page 115, now under submission.

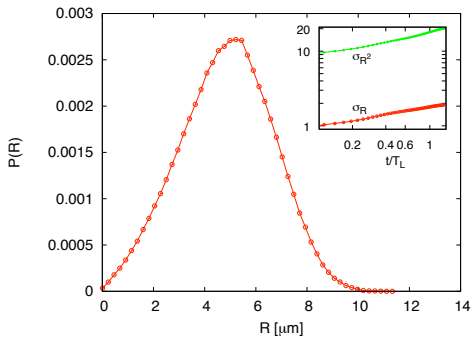

Figure 2.8: Droplet size distribution for the simulation matched to the large scales of the cloud, after $\tau_L \approx 150s$. In the inset: time evolution of the standard deviation of radius and square radius.

2.4 Laboratory-like framework and perspectives

An interesting development for this work would be to take into account the successive collision stage. The final droplet-size spectra of the condensation stage would be the initial condition for collision/coalescence. Depending on how broadly the initial droplet radii are distributed, one can evaluate how efficient the gravitational collision processes. Besides, one should consider that collisions are not only due to gravity, but also to turbulent transport. There is a long debate on how can clustering enhance the turbulent collision kernel (indicating the efficiency of turbulent collisions). In this respect, it would be interesting to first evaluate the degree of clustering achieved already in the condensation stage, to check whether collisions can happen already for small droplets due to their enhanced number density. Recent results have been published on this issue, coming both from *in situ*

measurements [16] and from laboratory experiments [15]. These could serve for comparison. Finally it would be interesting to evaluate the degree of droplet clustering in the successive stage, where droplets are larger and the effect is known to be more pronounced.

As already mentioned, the problem of the interactions between condensation and turbulence concerns different fields. In particular I am interested in the effects of turbulence on the evaporation of fuel droplets inside engines. This is an important effect for the correct design of spark-ignition engines. Indeed a faster evaporation of fuel allows for a more efficient fuel-air mixing occurring in the combustion chamber [30]. This may allow to improve both the performances and the emissions of the engine.
In order to faithfully reproduce the details of the system, I modified the model equations described in section 2.1 to take into account further possible couplings between the flow, the particles and the temperature and the vapor fields. I plan to perform simulations of a flow of particles entering a chamber with the possibility to evaporate and check the influence of turbulence on the evaporation time. Moreover, I would like to quantify the corrections given by the further couplings considered and check whether these change the qualitative mechanism I showed for the more simple settings. In particular, I would like to evaluate the corrections to the passive scalar scheme for the supersaturation due to the explicit integration of temperature fluctuations. This project is made in collaboration with C. M. Casciola and F. Salvadore from the University of Rome "La Sapienza". It would be extremely interesting to compare the numerical results with experiments of droplet condensation/evaporation in wind tunnels.

EUROPHYSICS LETTERS 15 June 2005

Europhys. Lett., **70** (6), pp. 775–781 (2005)
DOI: 10.1209/epl/i2005-10040-4

Droplet condensation in turbulent flows

A. Celani[1], G. Falkovich[2], A. Mazzino[3] and A. Seminara[1,3]

[1] *CNRS, INLN - 1361 Route des Lucioles, 06560 Valbonne, France*
[2] *Physics of Complex Systems, Weizmann Institute of Science - Rehovot 76100, Israel*
[3] *INFM, Dipartimento di Fisica, Università degli Studi di Genova and INFN, Sezione di Genova - Via Dodecaneso 33, 16146 Genova, Italy*

received 28 January 2005; accepted in final form 19 April 2005
published online 25 May 2005

PACS. 47.27.Eq – Turbulence simulation and modeling.
PACS. 47.27.Gs – Isotropic turbulence; homogeneous turbulence.

Abstract. – The problem of droplet growth by condensation in a turbulent flow of nearly saturated vapour is addressed theoretically and numerically. We show how the presence of an underlying turbulent velocity field induces a correlation between droplet trajectories and supersaturation. This leads both to the enhancement of the droplet growth rate and to a fast spreading of the droplet size distribution.

Introduction. – The evolution of microdroplets in a turbulent environment is an issue of great interest for a variety of applications ranging from health care [1], to engineering, to atmospheric sciences [2–4]. In the latter context, microdroplet growth by condensation/evaporation is a phenomenon of paramount importance for the early stages of cloud evolution. Warm clouds are essentially a polydisperse aerosol of water droplets suspended in a moist air. The smallest droplets are created by condensation onto sub-micron solid particles (cloud condensation nuclei), whereas raindrops typically exceed 1 mm in radius. This observation naturally motivates one to investigate droplet growth, which eventually leads droplets to fall under gravitational force. Different stages follow droplets formation. First, they grow by condensation of vapour molecules on their surface. Second, upon having reached a radius of the order of $20\,\mu$m, they begin to coalesce to form bigger drops. Here we focus on the first stage of the growth by condensation. Experimental measurements of droplet radii (see, *e.g.*, [5,6]) in fair weather clouds show a broad distribution in the range 1–$20\,\mu$m. The presence of droplets with very different sizes can significantly enhance the efficiency of successive collisions and thus contribute to a fast initiation of the precipitation process. However, up to now this effect has not been reproduced by classical models of the condensation stage [7]. Their basic ingredient is the assumption that droplets are essentially confined to a small portion of the cloud, dubbed "fluid parcel", where they experience the same value of humidity. Many efforts have been made to evaluate the influence of fine scale turbulence on the macroscopic properties of clouds (see [8] for a review). Recent numerical simulations of a turbulent ascending moist air parcel show that resolving the fluctuations below the scale of the parcel itself does not result in a significant spectral broadening [9–11]. The theory assuming Brownian random walk of an air

parcel in a vertical gradient of humidity does not give much broadening too [12]. Here we use a straightforward approach considering air velocity and vapour concentration as fields in space and evaluate droplet distribution in such a strongly fluctuating system. We thus consider the fundamental problem of a turbulent flow $\boldsymbol{v}$ which advects a vapour field and a number of droplets. Cloud physics is discussed as one of the possible applications of this analysis.

The idea is that the simultaneous transport of droplets and vapour by the same velocity field induces correlations between droplet trajectories and supersaturation values. Such correlation allows droplets to experience the same supersaturation value for a very long time. Let us stress that we do not consider edge effects like entrainment of dry air; the fluctuations of supersaturation are produced inside the cloud by the turbulent velocity field acting on the vertical gradient of humidity sustained by temperature. Strong fluctuations of humidity and the correlation between droplet trajectories and supersaturation lead to a significant spreading of the distribution of droplets radii.

In this letter we perform direct numerical simulations of the evolution of droplet trajectories and radii and of the velocity and supersaturation fields. We show a relevant effect of correlation induced by turbulent transport which reproduces a remarkable spreading of the size distribution. Droplets and water vapour molecules are the protagonists of this peculiar process. We discuss the possible impact of these ideas for condensation in clouds.

Model and DNS. – We consider the simplest generalization of the one-dimensional Twomey's model [13]. Twomey considered every droplet to grow in the same humidity conditions, while we consider the presence of vapour to vary in space and time. For this reason we introduce the supersaturation field $s(\boldsymbol{x},t) := \frac{e}{e_s}(\boldsymbol{x},t) - 1$, where e and e_s are the vapour pressure and the saturation vapour pressure, respectively. $s(\boldsymbol{x},t)$ quantifies the amount of vapour which is present in point $\boldsymbol{x}$ at time t: droplets are able to grow only where s is positive, that is in moist air (see eq. (3)). On the contrary, droplets tend to evaporate where s is negative (dry regions). The field s is taken as a passive scalar transported by a homogeneous turbulent flow $\boldsymbol{v}(\boldsymbol{x},t)$ which is not affected by its presence. Here we assume that local fluctuations of e_s are small so that fluctuations in s can be considered as a sum of fluctuations in e and e_s. In addition, vapour diffusivity and thermodiffusivity are close which makes s approximately satisfying the advection-diffusion equation. These assumptions lead to the following dynamical equations:

$$\partial_t s + \boldsymbol{v}\cdot\nabla s = A_1 w - \frac{s}{\tau_s} + D\nabla^2 s, \tag{1}$$

$$\partial_t \boldsymbol{v} + \boldsymbol{v}\cdot\boldsymbol{\nabla}\boldsymbol{v} = -\boldsymbol{\nabla}p + \nu\nabla^2\boldsymbol{v} + \boldsymbol{f}, \tag{2}$$

where w is the vertical component of the velocity field which obeys the Navier-Stokes equation (2). Let us remark that the passive scalar approximation for s can be applied in warm clouds, because here the parameters A_1 and τ_s depend very weakly on temperature([1]). The effect of the vertical temperature gradient, which certainly affects the global circulation in a cloud, can be neglected upon focusing on a volume of some hundreds of meters (see [14]). As we will discuss later, we are interested in such volume (large but not the largest), where the homogeneous-isotropic turbulence scheme holds. In the advection-diffusion equation (1), A_1 is the steady vertical gradient of the supersaturation so that the term $A_1 w$ is a source of supersaturation due to adiabatic ascent and the term $-s/\tau_s$ is the loss of water vapour due to condensation on droplet surface [2]. The balance of the source and sink with mixing and

([1])For warm-clouds temperatures, ranging from 273 to 300 K, we have A_1 ranging from $4.6E-4\,\mathrm{m}^{-1}$ to $5.7E-4\,\mathrm{m}^{-1}$, and (considering droplets of radius $10\,\mu$m and number density $100\,\mathrm{cm}^{-3}$) τ_s ranging from 3.1 s to 3.2 s.

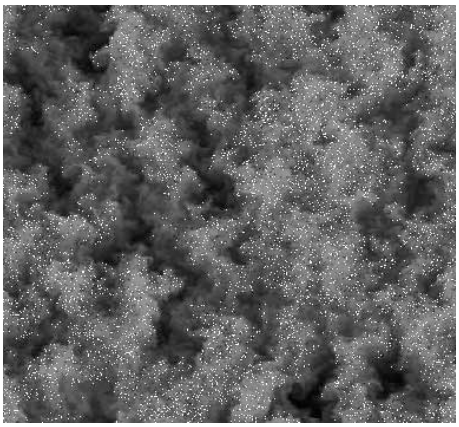

Fig. 1 – Spatial distribution of droplets (white points) and supersaturation field (light gray: supersaturated vapour $s > 0$, dark gray: subsaturated vapour $s < 0$). Droplets are preferentially concentrated in supersaturated portions of the cloud. This figure is obtained through a direct numerical simulation of a bi-dimensional domain $L \times L$. Evolution equations for velocity v and supersaturation s are integrated by a pseudo-spectral code with second-order Runge-Kutta scheme for time marching and periodic boundary conditions, with initial conditions obtained by running a simulation for about 20 large-eddy turnover time, in order to obtain a steady state. The velocity field is in the inverse cascade regime and shows power spectra very close to Kolmogorov 1941 prediction. For the velocity field, the energy injected at an average rate ϵ by a small-scale random forcing is dissipated on large scales by a linear friction $-\alpha \boldsymbol{v}$. Also the scalar field is in a steady state of direct cascade forced by the velocity field component in the direction of gravity (see eq. (1)). The resolution is 1024^2. Lagrangian equations (3), (4), (5) for $N = 20000$ droplet sizes and trajectories are integrated by an Euler method via bilinear interpolation of $\boldsymbol{v}$ and s. For this value of N the term s/τ_s is negligible compared to other terms in eq. (1). We chose absorbing boundary conditions for R, *i.e.* a droplet whose size vanishes is abandoned, and no new particles are considered to enter the volume. Initially droplets are homogeneously distributed.

diffusion determines the equilibrium value of supersaturation fluctuations. The timescale τ_s (*absorption time*) parameterizes such absorption of supersaturation as discussed in [8]. Its value depends on the presence of droplets: $\tau_s^{-1} \propto n \int_0^\infty r P(r,t) \mathrm{d}r$, where n is the numerical density of droplets, r is the value of droplet size and $P(r,t)$ is the size distribution. In the following analysis the sink term turns out to be negligible due to the smallness of n. This does not affect the qualitative behaviour of the supersaturation field. Equations (1), (2) are coupled with the Lagrangian evolution of droplet sizes R and trajectories $\boldsymbol{X}$:

$$\dot{R}(t) = A_3 s(\boldsymbol{X}(t),t)/R(t), \tag{3}$$

$$\dot{\boldsymbol{X}}(t) = \boldsymbol{U}(t) + \sqrt{2D}\boldsymbol{\eta}(t), \tag{4}$$

$$\dot{\boldsymbol{U}}(t) = -[\boldsymbol{v}(\boldsymbol{X}(t),t) - \boldsymbol{U}(t)]/\tau_d + g\hat{z}, \tag{5}$$

where $\tau_d = r^2/(3\nu\beta)$ is the Stokes timescale which characterizes every droplet([2]) ($\tau_d \approx 5{\cdot}10^{-4}$–$8 \cdot 10^{-3}$ s for water droplets of radius 5–20 μm in air). Note that we consider isolated droplets because during the condensation stage interactions between droplets are negligible.

([2])ν is the kinematic viscosity of air and $\beta = 3\rho_a/(2\rho_d + \rho_a)$.

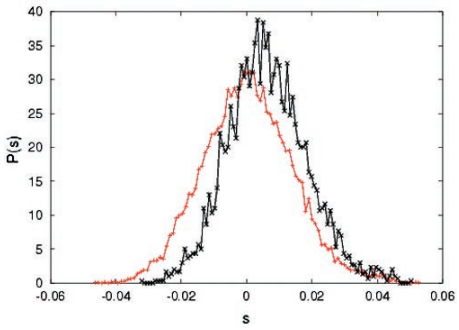

Fig. 2

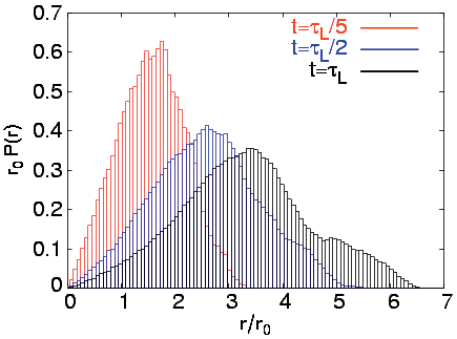

Fig. 3

Fig. 2 – Eulerian (gray, red on-line, curve) and Lagrangian (black curve) PDF of supersaturation at time $t = \tau_L$, where $\tau_L = \epsilon^{-1/3} L^{2/3}$ is the large-eddy turnover time.

Fig. 3 – Distribution $P(r)$ of droplet size r divided by the initial size r_0, at times $\tau_L/5$, $\tau_L/2$ and τ_L. The droplet size spectrum evolution shows a relevant spreading, which, after one τ_L produces 40% of droplets with $r > 4r_0$.

Equation (3) with the expression for A_3 can be found in [2], it has been widely used in classical models for an air parcel rising adiabatically. However, in our model, the size growth rate varies from a droplet to another, because it corresponds to the supersaturation value calculated along the trajectory of the droplet. Due to turbulent dispersion initially close droplets will eventually experience disparate values of supersaturation. From fig. 1 we detect a segregation effect in the spatial distribution of droplets. This feature is due to the presence of turbulent correlations between droplets and water vapour which allow droplets to experience for a long time the same supersaturation fluctuation. Consequently, when they fall for a long time in a dry region (shown in blue on-line) they totally evaporate and disappear making dry regions void of particles. A quantitative evaluation of the presence of correlations can be done by comparing Lagrangian and Eulerian statisics of the supersaturation field. We verify that the supersaturation values experienced by cloud droplets are greater than expected on the basis of Eulerian statistics alone (see fig. 2).

In fig. 3 the evolution of size distribution in time is shown. As expected from the presence of the correlation shown in fig. 1, we observe a relevant spreading of the size distribution which qualitatively agrees with observations. At the end of the condensation stage we observe a population of droplets having very different sizes: large droplets spent a long time in the moist environment while droplets in dry air remained small (this is very important for cloud physics, as remarked at the very beginning).

The question which naturally arises now is whether large and small droplets coexist locally, in a small volume. This is a very important question for coalescence because collision and collection are enhanced by the presence of very different droplets only if they come close, otherwise they never meet. To address this issue we divide the computational domain in a grid of $M \times M$ non-overlapping boxes (for different values of M). Within every box we consider, at a fixed time, the size distribution of the local population and evaluate it as a function of the variable $R/\langle R \rangle_{box}$, where $\langle R \rangle_{box}$ is the local mean radius([3]). Then we average the M^2 local PDFs

([3])For $M = 1$ they reduce to the global spectrum (last curve in fig. 3) normalized to the global mean radius.

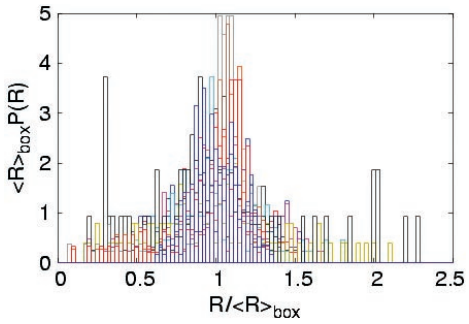

Fig. 4

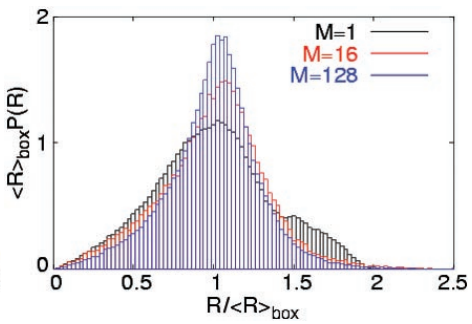

Fig. 5

Fig. 4 – Local distribution of droplet radii in 12 randomly picked boxes out of 4096 ($M = 64$) at time $t = \tau_L$.

Fig. 5 – PDF of droplet sizes averaged on M^2 boxes, for $M = 1, 16, 128$. We have excluded all boxes which contain only one particle. For the smallest boxes ($M = 128$) the number of almost void boxes, *i.e.* with one particle only, amounts to 3.6%. This value decreases upon increasing the total number of particles N. Here $N = 10^6$.

and compare the averages obtained for different M. In fig. 4 some of the local distributions of droplet radii PDFs are shown for $M = 64$, at time $t = \tau_L$: they are broad and therefore droplets with different sizes cohabit within small volumes. In fig. 5 the mean distributions are shown for $M = 1, 16, 128$. Again we observe broad distributions also for the smallest boxes we consider which is about three times the viscous scale η of our velocity field. The result shows that the broadening of the spectra is non trivial for the smallest scale we can consider.

Since the mean supersaturation is taken to be zero, a rough mean-field-type argument would yield no mean growth of droplet sizes (see eq. (3)). This prediction coincides with the classical one, which does not take into account the vapour field fluctuations. It turns out that the mean droplet size grows although the mean supersaturation value is set to zero (see fig. 6). Fluctuations thus play a crucial role for the growth of droplet radius.

To evaluate the role of inertia and sedimentation in this problem we compared the above simulations with analogous simulations where droplets are treated as fluid particles. Along Lagrangian trajectories we should observe the maximum correlation between droplets and vapour because here the supersaturation value is conserved. We would expect that inertia effects work against correlations, as they tend to deviate droplets from Lagrangian trajectories. Such effect is very weak, as we do not detect any differences between the two evolutions of the mean radius for the case with and without inertia effects (see fig. 6).

We observed no influence of inertia effects also for the segregation effect and the spreading of the size distribution. The only difference between the two simulations is visible from the evolution of mean-Lagrangian supersaturation, shown in fig. 7. From this figure we learn that in the early stage of their growth ($t/\tau_L < 0.4$) droplets are so small that inertia effects are completely negligible. They become visible (even if very weak) only at the end of the condensation stage. In view of these comparisons we can conclude that inertia and sedimentation do not change the qualitative picture of condensation we have drawn in the absence of inertia.

From the above results it turns out that turbulent fluctuations of the supersaturation field play a crucial role for droplets evolution. They allow droplets to behave in different ways

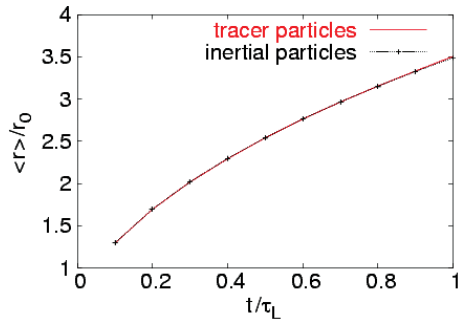

Fig. 6

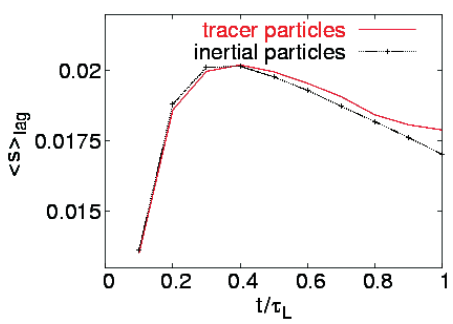

Fig. 7

Fig. 6 – Temporal evolution of $\langle r \rangle$, with $\overline{s} = 0$. The turbulent model allows the mean droplet size to grow by condensation although the Eulerian supersaturation average is set to zero. Notice that in these conditions classical models provide a constant mean droplet radius.

Fig. 7 – Mean-Lagrangian supersaturation for the model with (black curve) and without (gray, red on-line, curve) inertia effects.

depending on the particular fluctuation they experience, and lead to the segregation effect and the broadening of size spectrum.

As mentioned in the introduction, classical models of condensation in clouds focus on a single fluid parcel and do not reproduce the observed broadening of size spectra. We can now understand the reason for this shortcoming: droplets initially belonging to the same fluid parcel separate explosively and reach separations comparable with the cloud size in a time comparable with the condensation growth timescale: $t \simeq (L^2/\epsilon)^{1/3} \simeq 10^3\,\mathrm{s}$ for $L = 10^3\,\mathrm{m}$ and $\epsilon \sim 10^{-3}\,\mathrm{m^2\,s^{-3}}$. This makes questionable the very concept of fluid parcel. Therefore, to obtain the above results for a cloud, one should adopt a complementary point of view that consists in the simulation of the whole cloud volume. Such an approach must take into account that the spatial scales involved in atmospheric turbulence range from $\approx 1\,\mathrm{km}$ to $\approx 1\,\mathrm{mm}$. Accordingly, the degrees of freedom in a three-dimensional turbulent flow are approximately $Re^{9/4} \approx 10^{18}$ for typical cloud conditions. It is clearly impossible to simulate a system with such a huge amount of degrees of freedom. A possible way to overcome the problem is to examine a 2D turbulent flow. Moreover from the above results one expects that the most important scales in the problem are the largest ones([4]). One should indeed resolve the largest scales avoiding the detailed description of small scales.

Such approach does not describe timescales small enough to be comparable with the Stokes timescale for droplets. Hence the inertia effects cannot be taken into account. Even though droplet density, ρ_d, is much larger than air density, ρ_f, that approximation is reasonable for small droplets. Indeed the Stokes number for such droplets in a turbulent flow is $St = \tau_d/\tau_f \sim (2\rho_d\epsilon^{1/2}r^2)/(9\rho_f\nu^{3/2}) \approx 0.005$–$0.08$ for $R \approx 5$–$20\,\mu\mathrm{m}$, where τ_d and τ_f are timescales associated to the droplet and to turbulent fluctuations, respectively and the numerical evaluation has been carried out for $\epsilon \sim 10^{-3}\,\mathrm{m^2\,s^{-3}}$ and $\nu \sim 10^{-5}\,\mathrm{m^2\,s^{-1}}$.

Another point that is worth emphasizing in dealing with cloud physics is that the number of droplets in a cloud reaches values of 10^{17}–10^{18}. In the condensation stage it is not necessary to

([4])Furthermore, the assumption that for scales smaller than the fluid parcel scale there is no broadening and every droplet behaves in the same way seems to be reasonable according to [10].

consider this huge number of droplets because they do not interact with each other. Rather, we can follow the history of a large number of droplets which are representative of the statistical behaviour of the whole droplet population. The only drawback is that with a realistic number of droplets for a simulation the parameter τ_s is much larger than the largest timescale in the cloud. Indeed the simulated vapour field does not perceive the presence of droplets, because the sink term $-s/\tau_s$ in eq. (1) vanishes. But this is not the case of typical conditions for a developed cloud, in which the absorption time is 1–10 s (see [15]) and actually the sink term is relevant for producing vapour depletion. Therefore a way to evaluate an effective absorption timescale must be devised to reproduce the effect of droplets also on the vapour field.

* * *

This work has been supported by EU network HPRN-CT-2002-00300 and by Cofin 2003 "Sistemi Complessi e Problemi a Molti Corpi". Numerical simulations have been performed at CINECA (INFM parallel computing initiative).

REFERENCES

[1] Martonen T. B. (Editor), *Medical Applications of Computer Modeling* (WIT Press, UK) 2001.
[2] Pruppacher H. R. and Klett J. D., *Microphysics of Clouds and Precipitation* (Kluwer Academic Publishers, Boston) 1997.
[3] Rogers R. R. and Yau M. K., *A Short Course in Cloud Physics* (Pergamon Press, Oxford) 1989.
[4] Malinowski S. P., Zawadzki I. and Banat P., *J. Atmos. Ocean. Technol.*, **15** (1998) 1060.
[5] Warner J., *J. Atmos. Sci.*, **26** (1969) 1049.
[6] Brenguier J. L. and Chaumat L., *J. Atmos. Sci.*, **58** (2001) 628.
[7] Bartlett J. T. and Jonas P. R., *Q. J. R. Meteorol. Soc.*, **98** (1972) 150.
[8] Shaw R. A., *Annu. Rev. Fluid Mech.*, **35** (2003) 183.
[9] Vaillancourt P. A., Yau M. K. and Grabowski W. W., *J. Atmos. Sci.*, **58** (2001) 1945.
[10] Vaillancourt P. A., Yau M. K., Bartello P. and Grabowski W. W., *J. Atmos. Sci.*, **59** (2002) 3421.
[11] Korolev A., *J. Atmos. Sci.*, **52** (1995) 3620.
[12] Turitsyn K., *Phys. Rev. E*, **67** (2003) 062102.
[13] Twomey S., *Geofis. Pura Appl.*, **43** (1959) 243.
[14] Vaillancourt P. A. and Yau M. K., *Bull. Am. Meteorol. Soc.*, **81** (2000) 285.
[15] Khvorostyanov V. I. and Curry J. A., *J. Atmos. Sci.*, **56** (1999) 3985.

styleb.cls TJOT˙07˙210510 December 15, 2006 19:28

Journal of Turbulence
Volume xx, No. xx, 2007

Taylor & Francis
Taylor & Francis Group

Droplet condensation in two-dimensional Bolgiano turbulence

A. CELANI†, A. MAZZINO‡, A. SEMINARA*†‡ and M. TIZZI‡

†CNRS, INLN, 1361 Route des Lucioles, 06560 Valbonne, France
‡ Department of Physics, University of Genova and INFN Genova Section, via Dodecaneso 33, 16146 Genova, Italy

The evolution of microdroplets transported by a turbulent flow is considered. Droplets surrounded by moist air are able to grow by diffusion of water vapour on their surface. A two-dimensional model of dry Boussinesq thermal convection is considered in which the turbulent velocity field is driven by a temperature gradient. The evolution of the velocity, temperature, vapour fields and of droplet trajectories and radii is analysed by means of high-resolution direct numerical simulations. Despite the fact that the environment becomes drier and drier, a mean growth of droplets is obtained. The mechanism identified is based on the presence of correlations between the vapour field and droplet trajectories. Besides, a spreading of size distribution is observed, with the formation of droplets with very different sizes. Improvements with respect to previous models are discussed.

Keywords: Atmospheric turbulence; Turbulent convection; Direct numerical simulation; Two-dimensional turbulence

1. Introduction

The development of clouds is a topic of great interest, due to the clear importance of clouds for life on Earth. Their shape, lifetime, composition, can alter important climate parameters. The numerous physical processes which take place inside these enormous natural laboratories, make the problem complicated both from a theoretical and from an experimental point of view [1]; measures of small-scale characteristics in clouds are very difficult and their knowledge is still not complete. In this major problem some fundamental issues still must be fully understood. Measures in clouds reveal a broad-size distribution of small droplets while classical air-parcel models point to narrowing size spectra during the condensation stage. Indeed, as long as the collisions are rare (for droplets smaller than about 20 μm in radius), condensation is the only mechanism which can sustain droplet growth. However, the classical model of condensation inside a fluid parcel [2] predicts a narrowing of droplet size spectrum. Though some improvement has been achieved by including the effect of entrainment [3] of dry air inside the cloud, such a mechanism can only partially justify the presence of a wide range of droplet sizes, as it concerns only the cloud boundaries, whereas the spreading of size distribution is measured in adiabatic cloud cores as well. Other mechanisms have been proposed to explain such a property of the inner part of the cloud: the effect of stochastic fluctuations in the vapour field has been considered in [4], as well as in [5, 6] where droplet reaction on the vapour field is responsible for its local fluctuations. The effects of developed turbulence have been first

*Corresponding author. E-mail: agnese.seminara@inln.cnrs.fr

Q1

Journal of Turbulence
ISSN: 1468-5248 (online only)
http://www.tandf.co.uk/journals
DOI: 10.1080/14685240601105716

styleb.cls TJOT˙07˙210510 December 15, 2006 19:28

included in [7]. There, an ascending fluid parcel of moist air was considered, where droplets were able to grow by condensation: this resulted in a very limited degree of spreading of the size distribution.

In a recent paper [8], a very simple model of condensation in clouds was considered. Such simplicity allowed the authors to isolate a spreading mechanism due to correlations produced by the carrying flow: the idea was that droplets and vapour are correlated since they are advected by the same velocity field. Therefore, every droplet experiences the same ambient conditions for a timescale comparable to the large-eddy turnover time. In this picture, droplets belonging to a very moist region are able to grow faster than other droplets correlated to less moist regions, thus spreading the size distribution. Finally, droplets correlated to dry regions will evaporate and disappear leaving dry regions void of particles. That shows the importance of large-scale spatial fluctuations of the vapour field: droplets behave differently since they grow within different conditions of humidity. Clearly, in order to observe this mechanism the investigation of a large part of the cloud is required.

The aim of the present work is to verify the robustness of the identified mechanism in a more realistic framework including previously neglected aspects. In particular, in [8] homogenous isotropic turbulence was considered, sustained by an injection of energy modelled as a random process. Moreover, the back reaction of droplets on the vapour field was neglected, due to the small number of droplets. We wish now to make a further step by including two additional ingredients: the thermal convection due to an imposed temperature gradient and the effect of droplet feedback on vapour. Even if, in principle, results can substantially change, because of the different dynamics with the peculiar statistical properties of the Bolgiano regime for all the involved fields, we show the persistence of the described mechanism with a considerable broadening of size distribution. The qualitative picture does not present any remarkable difference.

2. The model

This section is devoted to describe the model we introduce to perform a numerical analysis of the condensation problem in two dimensions. As discussed above, we consider improvements of the model presented in [8] to describe more realistic features, namely the convection due to thermal unstable stratification and the feedback of droplets on the vapour field.

Convection is driven by the temperature field T, which is an active scalar coupled to the velocity field via the buoyancy term. In particular, we are dealing with a stratified medium (our idealised atmosphere), where a cooling contribution proportional to the vertical component w of the velocity field ($w = \boldsymbol{v} \cdot \hat{z}$) is explicitly taken into account in the equation for the temperature field. The physical meaning of such a term is the cooling of an ascending air parcel at a constant rate Γ_a (adiabatic lapse rate). Note that we set Γ_a to the moist value, which amounts to incorporating an average contribution due to latent heat effects. Because of stratification we can split the temperature as the sum of two terms, a mean profile $-Gz$ and a fluctuation T' around it with zero average which satisfies the equation

$$\partial_t T' + \boldsymbol{v} \cdot \boldsymbol{\nabla} T' = (G - \Gamma_a) w + \kappa \Delta T', \tag{1}$$

where the term $(G - \Gamma_a)w$ is the injection of scalar fluctuations and κ is the molecular diffusivity. Note that, here, the role of temperature is to sustain, as a local pumping term, velocity fluctuations. The simplest, even if non-trivial, way to obtain a convective background

is to focus, as a first step, on a two-dimensional setup. This is the essence of the Bolgiano turbulent regime.

Temperature fluctuations drive the vorticity field ω, which follows the equation

$$\partial_t \omega + \boldsymbol{v} \cdot \boldsymbol{\nabla} \omega = \beta \boldsymbol{g} \times \boldsymbol{\nabla} T' + \nu \Delta \omega, \tag{2}$$

where $\boldsymbol{g}$ is the gravitational acceleration, β is the thermal expansion coefficient and ν is the kinematic viscosity. Since compositional effects are generally thought to be small (see [9]), we consider here dry buoyancy. We focus on the *Bolgiano regime* [10] in which the dynamics is ruled by the scale-by-scale equilibrium between the inertial term $\boldsymbol{v} \cdot \boldsymbol{\nabla} \omega$ and the Boussinesq buoyancy term $\beta \boldsymbol{g} \times \boldsymbol{\nabla} T'$ (see the appendix for a description of this regime).

Let us now discuss the inclusion of the back reaction of droplets on the vapour field. To do that, we first introduce an important ingredient of the considered model: the vapour field. The *supersaturation* field $s(\boldsymbol{x}, t)$ quantifies the amount of vapour which is present in the position $\boldsymbol{x}$ at time t. It is defined by $s(\boldsymbol{x}, t) \equiv e(\boldsymbol{x}, t)/e_s(\boldsymbol{x}, t) - 1$, where e and e_s are the vapour pressure and the saturation vapour pressure, respectively. In the regions where s is positive (*moist regions*) vapour exceeds the equilibrium point and therefore tends to condense. Conversely, *dry regions* are poor of vapour and water here is expected to evaporate. According to a simple generalisation of the well-known Twomey's model [2], where we considered space/time dependences brought by the turbulent velocity field instead of the sole time dependence of the classical Twomey's model, the supersaturation field is considered as a passive scalar and is thus ruled by the equation

$$\partial_t s + \boldsymbol{v} \cdot \boldsymbol{\nabla} s = A_1 w - \frac{1}{\tau_s} s + D \Delta s, \tag{3}$$

where $A_1 w$ is a local source (or sink) of supersaturation due to the cooling (or heating) of an ascending (or descending) volume, while $-s/\tau_s$ accounts for the *local* feedback of droplets on vapour. We wish to introduce such interaction at local level in order to describe the spatial variations in the statistics of s, which depend on how many droplets are locally present. The *absorption time* τ_s is thus considered here as a field, evolving in space and time according to the size and number density of droplets. During evolution, in each point $\boldsymbol{x}$, τ_s is inversely proportional to the sum of the radii R_i of the $N(\boldsymbol{x}, t)$ droplets present in a little volume around $\boldsymbol{x}$ (see e.g. [11]):

$$\frac{1}{\tau_s}(\boldsymbol{x}, t) = A \sum_{i=1}^{N(\boldsymbol{x},t)} R_i(t), \tag{4}$$

where A is a function of thermodynamic parameters and temperature. The coefficients A and A_1 can be considered constant since their maximum variation within the whole domain (few hundreds meters) is less than 1% (see [12]). In the numerical procedure we consider that every droplet affects the value of τ_s in the four nodes surrounding its position. The weight of the contribution to each node depends on the distance from the node via bilinear interpolation.

The Lagrangian equations for the trajectory and radius of each droplet are required to complete the model. Thanks to the small droplet Reynolds numbers, the small Stokes numbers and the small mass loading (ratio of the total mass of particles and the mass of the carrier fluid), we can consider droplets as independent, passive particles (see [13]). Moreover we assume droplets as tracer particles (see discussion in [8]), since the Stokes timescale of the largest droplet in our simulations is about 0.01 s, much shorter than the shortest timescale

styleb.cls TJOT˙07˙210510 December 15, 2006 19:28

associated with our turbulent velocity field ($\tau_\eta \approx 2.5$ s). Hence, for the ith droplet we obtain

$$\frac{\mathrm{d}}{\mathrm{d}t}\boldsymbol{X}_i(t) = \boldsymbol{v}(\boldsymbol{X}_i(t), t) + \sqrt{2D}\boldsymbol{\eta}_i \tag{5}$$

$$\frac{\mathrm{d}}{\mathrm{d}t}R_i^2(t) = 2A_3 s(\boldsymbol{X}_i(t), t), \tag{6}$$

where $\boldsymbol{\eta}_i$ are independent white noises and A_3 can be considered as a constant. Note that gravity acceleration has been neglected in equation (5), since the terminal velocity is a small fraction (from 0.01 to 0.25) of the minimum velocity we can resolve.

The feedback of droplets on vapour has now an important role linked to the correlation effect shown in [8]. If such effect was still present, dry regions would be void of droplets, providing no vapour loss there. All droplets would be segregated in moist regions where they would grow consuming the surrounding vapour thus slowing down their growth. This could change the prediction on the spreading of size distribution. Moreover, let us stress that the air can become undersaturated on average, as discussed in the following; thus from equation (6), with a mean-field-type argument, we would not expect any mean growth of radii. The aim of the following section is therefore to quantify the importance of the droplet back reaction on vapour in the present framework.

3. Results

As discussed in the previous section, we focus on a regime which presents the different statistical properties of velocity, temperature and supersaturation with respect to Kolmogorov 1941s. We wish now to consider the evolution of droplets advected by a convective velocity field and interacting with the described supersaturation field. We performed a series of high resolution (1024^2) direct numerical simulations of model equations (1)–(6), integrating the 2D velocity field $\boldsymbol{v}$, the temperature field T and the supersaturation field s by a standard 2/3-dealiased pseudospectral method on a doubly periodic square domain of length 2π. The dissipative terms have been substituted, as customary, by hyperviscous terms of order eight for the viscosity and of order 4 for the diffusivities. A linear friction term is added to the vorticity equation to prevent the energy from accumulating at the lowest accessible modes. The time evolution is implemented by a standard second-order Runge–Kutta scheme with a time step of about $\tau_\eta/250$. Once the stationary state is reached (after about $17\,\tau_L$), we put one million droplets randomly in a space and with the initial size around $R_0 = 4\,\mu$m, growing according to equation (6); we follow their evolution for over $2\,\tau_L$. Since the atmospherical Reynolds number can reach enormous values, around 10^7–10^8, we have to choose the range of scales we are interested in. If we focus the attention on a small fluid parcel, describing the small-scale dynamics in great detail, we cannot take into account the effect of large-scale fluctuations of the fields. Namely we would have almost the same ambient conditions for all droplets inside the computational domain, because fluctuations are tiny at small scales. But droplets transported by the turbulent flow are in fact able to span a very large volume of the cloud and therefore to experience very different ambient conditions. We then choose to simulate the evolution of the whole cloud, not resolving the small-scale details (see [8] for discussion).

Before showing the results, we give a remark on the mean vapour field. The equation of evolution of s, does not preserve its average: it is not clear *a priori* the general trend of the

styleb.cls TJOT˙07˙210510 December 15, 2006 19:28

4C/Art

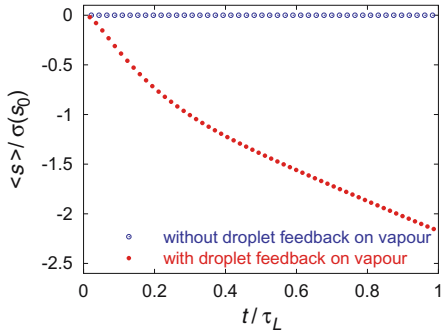

Figure 1. Mean supersaturation evolution in time. Here, $\sigma(s_0)$ is the standard deviation of the initial field $s(\boldsymbol{x}, 0)$ and τ_L is the large-eddy turnover time. Note that there is a constant negative trend which suggests the presence of correlations between s and τ_s^{-1} as discussed in the text.

mean supersaturation $\langle s \rangle$. Indeed, by averaging equation (3) we obtain

$$\frac{\mathrm{d}}{\mathrm{d}t}\langle s(\boldsymbol{x}, t)\rangle = -\left\langle \frac{s(\boldsymbol{x}, t)}{\tau_s(\boldsymbol{x}, t)} \right\rangle. \tag{7}$$

Let us guess the sign of $\langle s/\tau_s \rangle$. If the fields $s(\boldsymbol{x}, t)$ and $\tau_s^{-1}(\boldsymbol{x}, t)$ were independent, $\langle s/\tau_s \rangle = \langle s \rangle \langle \tau_s^{-1} \rangle$ and the rhs of equation (7) would have the sign opposite to $\langle s \rangle$, given that $\langle \tau_s^{-1} \rangle > 0$. In this case equation (7) tells us that the mean supersaturation decays in time. Consider now the extremely correlated situation in which all droplets are concentrated in moist regions. In this case, dry regions would be totally void of droplets: here τ_s^{-1} would vanish (see equation (4)). In contrast, we would have droplets—and therefore $\tau_s^{-1} > 0$—only in moist regions, i.e., where $s > 0$, providing $\langle s\tau_s^{-1} \rangle > 0$. From equation (7) we can conclude that in the presence of correlations there is a general negative trend of $\langle s \rangle$. The result shown in figure 1 demonstrates that the average supersaturation has a constant negative trend which confirms the presence of correlations between droplets and vapour. As a consequence we are dealing with a drier and drier environment, which works against the growth of droplets.

We wish now to ask directly whether correlations are actually present. The answer is given in figure 2, where we show the snapshots of the field $s(\boldsymbol{x}, t)$ beside the field $\tau_s^{-1}(\boldsymbol{x}, t)$. The figure shows that droplets are present (i.e. $\tau_s^{-1}(\boldsymbol{x}, t) > 0$ in the left panel) only in moist regions (shown in light blue in the right panel).

From these results we can conclude that the dynamical state produced by thermal convection does not affect the presence of correlation and the segregation of droplets in moist regions detected in the framework of homogeneous isotropic turbulence [8]. We come now to the quantitative description of droplet size spectrum evolution.

The picture we have qualitatively drawn for the back reaction of droplets on vapour is that every droplet grows absorbing the surrounding vapour, providing a drier and drier environment and slowing down its growth. Since τ_s^{-1} is proportional to droplet radii, the larger the droplet, the faster the vapour loss. Therefore we expect that such feedback results in a slowing down of the mean droplet growth and of the spectrum broadening as well. In figure 3 we compare the mean radius growth obtained by two simulations beginning with the same initial condition: in order to obtain the effect of droplet feedback on water vapour, one of the two simulations neglects the term $-s/\tau_s$ in equation (3). As we expected, neglecting the back reaction of droplets on vapour results in an overestimate of the mean growth rate. Indeed, in a large-eddy

styleb.cls TJOT˙07˙210510 December 15, 2006 19:28

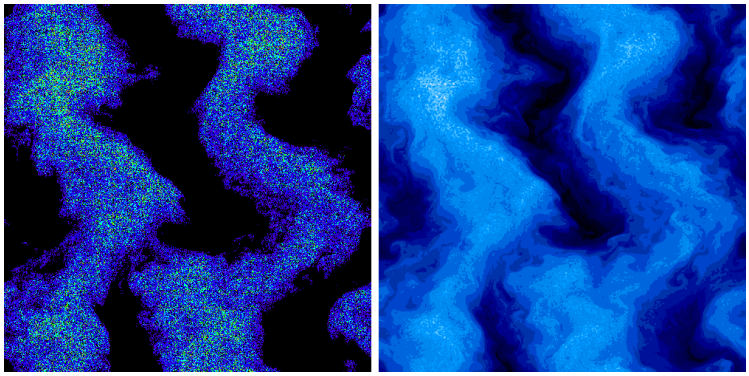

Figure 2. Left panel: snapshot of the field $\tau_s^{-1}(\boldsymbol{x}, t)$ obtained by summing the radius of droplets inside a small volume $\delta V_{\boldsymbol{x}}$ around point $\boldsymbol{x}$ at time $t = 0.1\,\tau_L$ (entire domain). From equation (4), τ_s^{-1} vanishes where no particles are present (black regions). Right panel: snapshot of the supersaturation field $s(\boldsymbol{x}, t)$ at the same time $t = 0.1\,\tau_L$. Dry regions are represented in dark blue, while moist ones are represented in light blue. Dark regions of the left panel correspond to dark regions of the right one: dry regions are void of droplets. Note that the different patterns with respect to figure 1 in [8] are due to the different dynamical regime considered.

turnover time τ_L, which corresponds to $\sim$100 s, droplets grow due to the sole condensation mechanism, until $\sim 50\,\mu$m on average. This value is actually much larger than observed in real clouds (see e.g. [1]). Taking into account this term goes in the direction of slowing down the condensational growth, making the prediction more realistic.

With the same spirit we compare the evolution of droplet size spectrum obtained with the same couple of simulations. The result of the comparison is shown in figure 4 for the two cases with and without the feedback of droplets on vapour: again the expectation of a slower spreading was right. However, the quantitative data show that also taking into account the droplet feedback on vapour, the condensation stage produces droplets with a significantly broad size distribution.

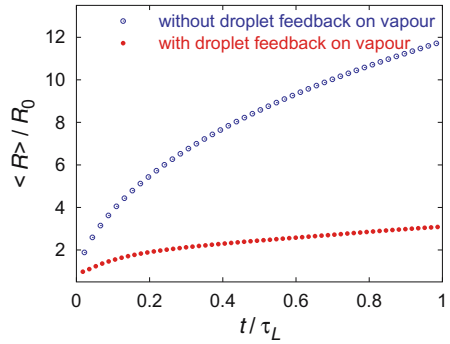

Figure 3. Growth of the mean radius in time, for the case with (red line) and without (blue line) the sink term $-s/\tau_s$. Note that neglecting the feedback of droplets on water vapour results in an overestimate of the mean growth of droplets.

styleb.cls TJOT˙07˙210510 December 15, 2006 19:28

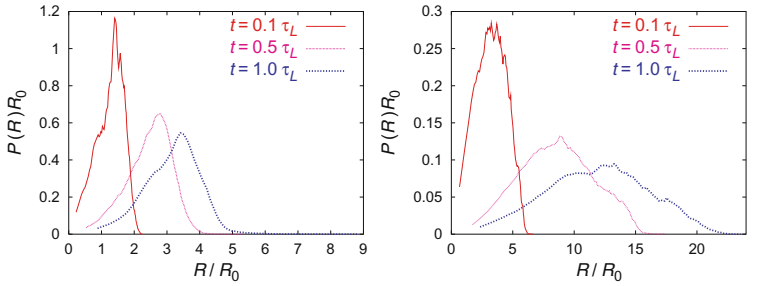

4C/Art

Figure 4. Droplet size spectrum for the case with accounted (left panel) and neglected (right panel) feedback of droplets on vapour. Note that, since $R_0 = 4\,\mu$m, neglecting the feedback term results in the production of droplets with radii up to $85 \div 90\,\mu$m after one τ_L ($\approx$100 s), while accounting for such term results in a more reasonable maximum size of $20 \div 22\,\mu$m.

4. Conclusions and perspectives

The aim of the present work was to improve the results obtained in [8] for droplet condensation in highly idealised models of turbulent clouds. Two new ingredients were introduced to move towards a more realistic framework. We considered indeed thermal convection to drive the velocity field through buoyancy. The latter mechanism changes the stationary state of the turbulent system and yields a very different statistics with respect to the classical 2D inverse cascade regime. Moreover, we consider here the feedback of droplets on vapour which was previously neglected. Such interaction is modelled by an additional term in the equation of evolution for the vapour field and, heuristically, works against the fast growth and spreading of droplet radii. The results show that the spreading mechanism identified in [8] is still present despite the different statistical properties of the turbulent regime analysed. The slowing down of spreading and mean growth does not affect the general behaviour of the droplet size spectrum; in contrast, it results in a more realistic prediction.

A necessary step in the direction of a description of droplet condensation is a complete 3D simulation of the system. Such issue could support the significance of the mechanism identified for a more exhaustive picture of droplet growth by condensation in warm clouds.

Acknowledgements

This work has been supported by the EU under the contract HPRN–CT–2002–00300, by the Italian MIUR COFIN 2005 project no. 2005027808 and by the Italian consortium CINFAI; as has been partially supported by L'ORÉAL Italia Per le Donne e la Scienza.

Appendix A. The Bolgiano regime

The two-dimensional Boussinesq turbulent convection is described by the following couple of partial differential equations [14]:

$$\partial_t \omega + \boldsymbol{v} \cdot \boldsymbol{\nabla} \omega = -\beta \boldsymbol{\nabla} T \times \boldsymbol{g} + \nu \Delta \omega \tag{A1}$$

$$\partial_t T + \boldsymbol{v} \cdot \boldsymbol{\nabla} T = \kappa \Delta T. \tag{A2}$$

styleb.cls TJOT˙07˙210510 December 15, 2006 19:28

Here, T is the temperature field and the vorticity ω is a scalar field, since in a plane flow $\boldsymbol{\nabla} \times \boldsymbol{v}$ has only the normal component. In order to mimic both the fact that the fluid is supposed to be heated from below and that the mean temperature profile in a cloud is an almost linearly decreasing function of the elevation, a mean profile $\langle T(\boldsymbol{r}, t)\rangle = \boldsymbol{G}\cdot\boldsymbol{r}$ is assumed, with a constant gradient $\boldsymbol{G}$ pointing downwards in the direction of the gravity field. In a similar model, studied in [15–17], no mean gradient is present and a forcing term is added to the equation for the temperature field. There, the average temperature becomes constant and turbulence is not excited locally, but emitted from the underlying layer.

In equation (A2) the temperature field affects the vorticity through the buoyancy forces, thus providing an example of active scalar turbulence. At large enough values of β, the buoyancy forces can equilibrate the inertial terms in the velocity dynamics, while the temperature fluctuations cascade towards the small scales at a rate ϵ.

Let us briefly recall the phenomenology of 2D turbulent convection (for the 3D case, see e.g. [18, 19]). The balance of buoyancy and inertial terms in equation (A2) introduces the Bolgiano length scale l_{B} [18]. At small scales, $r \ll l_{\mathrm{B}}$, the inertial term is larger than buoyancy forces and the temperature is basically a passive scalar. At scales $r \gg l_{\mathrm{B}}$, buoyancy dominates and affects the velocity, which performs an inverse energy transfer in two dimensions. However, unlike what happens in the usual 2D Navier–Stokes turbulence, the kinetic energy input rate here depends on the scale. Dimensional arguments yield:

$$\epsilon(r) = \beta \boldsymbol{g} \cdot \langle \boldsymbol{v}(\boldsymbol{x}+\boldsymbol{r}, t) T(\boldsymbol{x}, t)\rangle \sim r^{4/5} \tag{A3}$$

and the dimensional expectations for both velocity and temperature structure functions:

$$S_N^v(r) = \langle (\delta_r v_\parallel)^N \rangle \sim [\epsilon(r)\, r]^{N/3} \sim r^{\zeta_N^v} \qquad \zeta_N^v = \frac{3N}{5} \tag{A4}$$

$$S_N^T(r) = \langle (\delta_r T)^N \rangle \sim r^{\zeta_N^T} \qquad \zeta_N^T = \frac{N}{5}. \tag{A5}$$

Numerical results show that no intermittency corrections are observed for the velocity, whereas the temperature field appears strongly intermittent and saturates to a constant value (see [14]). Second-order structure functions for both velocity and temperature are reported in figure A1, in good agreement with the dimensional predictions (A4) and (A5).

4C/Art

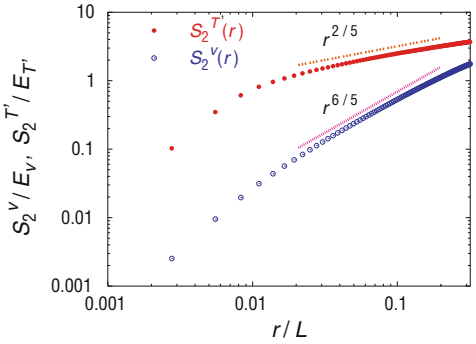

Figure A1. Second-order structure functions of both velocity (curve below) and thermic fluctuation (curve above) in the stationary state. Droplet evolution during the condensation stage has been studied in this state. Slopes are relative to the dimensional predictions (A4) and (A5). Ordinates are made dimensionless through $E_{T'} \equiv (\langle T'^2/2\rangle)^{1/2}$ and $E_v \equiv \langle v^2/2\rangle^{1/2}$.

styleb.cls TJOT˙07˙210510 December 15, 2006 19:28

References

[1] Shaw, R.A., 2003, Particle-turbulence interactions in atmospheric clouds. *Annual Reviews of Fluid Mechanics*, **35**, 183–227.

[2] Twomey, S., 1959, The nuclei of natural cloud formation: part II. The supersaturation in natural clouds and the variation of cloud droplet concentrations. *Geofisica Pura e Applicata*, **43**, 243–249.

[3] Telford, J.W., 1996, Clouds with turbulence; the role of entrainment. *Atmospheric Research*, **40**, 261–282.

[4] Bartlett, J.T. and Jonas, P.R., 1972, On the dispersion of the size of droplets growing by condensation in turbulent clouds. *The Quarterly Journal of the Royal Meteorological Society*, **98**, 150–164.

[5] Shaw, R.A., Reade, W.C., Collins, L.R. and Verlinde, J., 1998, Preferential concentration of cloud droplets by turbulence: effects on the early evolution of cumulus cloud droplet spectra. *Journal of the Atmospheric Sciences*, **55**, 1965–1976.

[6] Jaczewski, A. and Malinowski, S.P., 2005, Spatial distribution of cloud droplets in a turbulent cloud-chamber flow. *The Quarterly Journal of the Royal Meteorological Society*, **131**(609), 2047–2062.

[7] Vaillancourt, P.A., Yau. M.K., Bartello, P. and Grabowski, W.W., 2002, Microscopic approach to cloud droplet growth by condensation: part II. Turbulence, clustering and condensational growth. *Journal of the Atmospheric Sciences*, **59** 3421–3435.

[8] Celani, A., Falkovich, G., Mazzino, A. and Seminara, A., 2005, Droplet condensation in turbulent flows. *Europhysics Letters*, **70**(6), 775–781.

[9] Stevens, B., 2005, Atmospheric moist convection. *Annual Reviews of Earth and Planetary Science*, **33**, 605–643.

[10] Bolgiano, R., 1959, Turbulent spectra in a stably stratified atmosphere. *Journal of Geophysical Research*, **64**(12), 2226–2228.

[11] Vaillancourt, P.A., Yau, M.K. and Grabowski, W.W., 2001, Microscopic approach to cloud droplet growth by condensation: part I. Model description and results without turbulence. *Journal of the Atmospheric Sciences*, **58**, 1945–1964.

[12] Korolev, A.V. and Mazin, I.P., 2003, Supersaturation of water vapor in clouds. *Journal of the Atmospheric Sciences*, **60**, 2957–2974.

[13] Vaillancourt, P.A. and Yau, M.K., 2000, Review of particle-turbulence interactions and consequences for cloud physics. *Bulletin of the American Meteorological Society*, **81**(2), 285–298.

[14] Celani, A., Mazzino, A. and Vergassola, M., 2001, Thermal plume turbulence. *Physics of Fluids*, **13**(6), 2133–2135.

[15] Toh, S. and Matsumoto, T., 1999, The dynamics of structures of T-vorticity in 2D free convection turbulence. *Proceedings of IUTAM Symposium on Geometry and Statistics of Turbulence, Hayama, November 1999* (Dordrecht: Kluwer Academic).

[16] Biskamp, D. and Schwarz, E., 1997, Scaling properties of turbulent convection in two-dimensional periodic systems. *Europhysics Letters*, **40**(6), 637–642.

[17] Biskamp, D., Hallatschek, K. and Schwarz, E., 2001, Scaling laws in two-dimensional turbulent convection. *Physical Review* E **63**, 045302.

[18] Monin, A. and Yaglom, A., 1975. *Statistical Fluid Mechanics* (Cambridge, MA: MIT Press).

[19] Siggia, E.D., 1994, High Rayleigh number convection. *Annual Reviews of Fluid Mechanics*, **26**, 137.

Condensation of cloud microdroplets in homogeneous isotropic turbulence

Alessandra S. Lanotte[1], Agnese Seminara[2,3], and Federico Toschi[4]
[1] CNR - ISAC and INFN, Str. Lecce-Monteroni, I-73100 Lecce, Italy
[2] CNRS - INLN, 1361 Route des Lucioles, F-06560 Valbonne, France
[3] Dipartimento di Fisica, Università degli Studi di Genova and INFN Sezione di Genova, Via Dodecaneso 33, I-16146 Genova, Italy
[4] CNR - IAC "Mauro Picone", Viale del Policlinico 137, I-00161 Rome, Italy

May 18, 2007

Abstract

We consider the growth by condensation of small water droplets in a homogeneous isotropic turbulent flow. Droplet size spectra evolution is described by means of high-resolution (up to 512^3 grid points) $3D$ direct numerical simulations of a simple model of advection and condensation. The dynamics and growth of millions of droplet is integrated. A droplet-size spectra brodening is obtained and it is shown to increase with the Reynolds number of turbulence. An evaluation of this increase points to a significant spreading achieved by real cloud turbulence. Results can be understood in terms of dimensional arguments and give an interesting information for a possible LES analysis of the problem at hand.

1 Introduction

The growth of microdroplets by condensation is a long-standing problem of cloud physics [1], meteorology [6], medicine [7] and engineering [8]. A fundamental understanding of key issues such as the turbulent mixing inside clouds or the interaction of turbulence with microphysics is important for a variety of applications (the parameterization of small scales in models resolving larger scales, the analysis of radiative transfer through clouds, the prediction of the initiation of precipitation). The peculiar features of turbulence, affecting the motion on a wide range of space-time scales, can alter significantly the condensation process, by providing a strongly fluctuating and intermittent moist environment. This is a well-known concept in engineering, where turbulence is considered as a key ingredient for the optimization of fuel-air mixing and the rate of fuel vaporization in engines [8]. Similar ideas have a long hystory in cloud physics as well: turbulence is believed to act both on collision processes [9, 14, 13, 11, 35, 12, 10] and on condensation, that we focus here.

Condensation is a fundamental process for the early stages of cloud evolution. It is the only mechanism able to grow droplets immediately after their formation, when

they are few μm in size. When a few of them become large enough to fall - a radius of $20\,\mu m$ is commonly considered as a threshold - they begin to collide and coalesce. Collisions are much more efficient than condensation as a growth mechanism. Indeed, after nucleation droplet radius grows of roughly one order of magnitude by condensation. In a comparable timescale, collisions grow droplets to raindrops, bridging a gap of around 2 orders of magnitude in size. However, the high efficiency of the latter is strongly influenced by the general features of the former. In particular, gravitational collisions are highly effective when the population of droplets coming from condensation span a large variety of sizes. Uniform condensational growth leads to narrow droplet-size spectra instead (see e.g. [3, 2]). Namely, provided that all droplets grow in similar ambient conditions, small droplets grow faster than large ones and thus all droplets finally tend to converge to the same size. This is the long-standing problem of the bottleneck in the transition between condensation and collision-coalescence.

The presence of broad droplet-size distributions have been detected by *in situ* measurements in warm clouds under very broad conditions [15]. Still, this property keeps eluding full theoretical understanding despite the number of different approaches developed to this purpose. Some of them rely on the effects of entrainment and mixing with non-cloudy air interesting the regions of the cloud near to the boundaries (see, e.g., [16]). However, broad spectra are also observed inside the inner adiabatic cores [17], where no boundary effects can possibly explain their presence. Droplets themselves have been proposed to be sources of local variability in the environment conditions. Indeed, droplet evaporation is an internal source of turbulent kinetic energy due to cooling associated to the absorption of latent heat, coupled with buoyancy [19, 21, 20]. Besides, their presence locally change the water vapor content through phase change [18]. The general conclusion is that these microscopic fluctuations influence the process of mixing occurring at the interface between cloud and clear-air. Also, the presence of ultra-giant condensation nuclei has been proposed to explain the large raindrops production [22]. Other properties such as salinity and surface curvature may produce absolute and relative broadening, as proposed in [23].

Stochastic fluctuations of the environmental conditions, induced by turbulence have been envisioned as a broadening mechanism since the '60s, see e.g. [24, 26, 25], when the theory of stochastic condensation was first proposed. This approach explains droplet spectra broadening by observing that fluctuations of the ambient conditions make droplets grow at different rates. This simple idea is very powerful, in that it interests the whole cloud, regardless the presence of additional microscopic mechanisms, the presence of ultra-giant nuclei or boundary effects such as mixing with dry air and entrainment. Although all these ingredients play a role in these huge natural laboratories, their contribution may differ according to different conditions. On the other hand, turbulence in clouds is a spectacular phenomenon with a wide range of scales dynamically coupled in the process of non-linear energy cascade. For this reason, turbulence is a very good candidate as broadening mechanism generally at work within convective warm clouds. At a Reynolds number approaching $Re \sim 10^8$, turbulence is known to be highly intermittent, with statistics strongly deviating from a gaussian one and a substantial probability of fluctuations far exceeding the standard deviation [5]. This means that droplets coming close one to the other might have previously experienced disparate conditions, thus invalidating any expectation based on uniform condensation.

Here we want to show that some qualitative features emerging from a simple idealised setting - to be introduced below - may be well present in more complex models, just because they are a consequence of basic properties of turbulence itself.

In view of this purpose, under consistent hypothesis, we consider a model of condensation that privileges simplicity and generality with respect to the detailed description of all the microphysical features. Droplets growth in a fully developed turbulent flow can not be treated analitically and numerical simulations become a fundamental tool of investigation. Numerical approaches to cloud turbulence are very demanding because of the huge number of active degrees of freedom. In terms of the spatial structure of the turbulent fields, direct numerical simulations (DNS) can either focus on large-scale structures [27, 28], or resolve the small scale features [29, 30, 31, 19]. The two choices are actually complementary and both have strong and weak points (see Section 2, for further details). Here we develop a third point of view. First we evaluate the spreading of droplet-size distributions through a series of direct numerical simulations, at increasing resolutions, matched to the small scales. Not surprisingly, each single DNS gives a small degree of spreading, as already pointed out in previous works focusing on small rising fluid parcels (see e.g. [30, 31, 19]). However this only tells us that small scale turbulence alone is not enough to explain the large size spreading observed in clouds. Therefore, we evaluate the dependence of the size spectra broadening on the turbulent Reynolds number, i.e. on the range of spatial scales resolved. The broadening is found to increase with the Reynolds number of turbulence with a trend that can be understood on the basis of dimensional arguments. We extrapolate this curve to high Reynolds numbers to evaluate the effects of realistic cloud turbulence within the model adopted. It turns out that homogeneous isotropic turbulence in a cloud core of size around $100\,m$ would produce a remarkable spreading of the droplet size distribution. Note that this does not clarify whether the whole range of spatial scales is actually crucial to obtain the extrapolated behavior. We perform a further simulation that provides arguments supporting a role of primary importance for large scale fluctuations. This is an interesting conclusion in the context of large-eddy simulations or, more generally, models that have to deal with the problem of parameterization of small scales.

The paper is organised as follows. In Section 2, we introduce the model for the time evolution of the vapor field and the droplets advected by the turbulent air flow. Section 3 is devoted to explain the numerical approach and DNS details. Results concerning the spreading of droplet size spectrum are discussed in Section 4. Section 5 is devoted to conclusions and perspectives.

2 Model equations and numerical procedures

We focus our attention on a turbulent velocity field carrying vapor and droplets. The latter undergo size changes for evaporation or condensation of the surrounding vapor. The three-dimensional velocity field $\mathbf{v}$ evolves according to the Navier-Stokes equations for an incompressible flow,

$$\partial_t \mathbf{v} + \mathbf{v}\cdot\boldsymbol{\nabla}\mathbf{v} \,=\, -\boldsymbol{\nabla}\frac{p}{\rho_a} + \nu\Delta\mathbf{v} + \mathbf{f}, \qquad \boldsymbol{\nabla}\cdot\mathbf{v} \,=\, 0, \tag{1}$$

where p is the pressure, ρ_a is the air density, ν is the air kinematic viscosity and $\mathbf{f}$ is an external statistically homogeneous and isotropic pumping, providing a turbulent

stationary flow. Cloud turbulence is generated by large-scale turbulent fluctuations which can be strongly anisotropic. Indeed the presence of gravity introduces a preferential direction through large scales thermal gradients and buoyancy, the engine of convective motions. However, we can assume that for sufficiently small internal cloud cores, vertical stratification of the environment can be neglected and the small-scale flow is essentially forced by nonlinear transfer from larger scales, rather than by buoyancy. Isotropy can thus be assumed for the small scale motion. In [33], the authors argue that this should be valid in warm-cloud cores for spatial scales up to $L \sim 100\,m$. In addition to large-scale thermal gradients, anisotropy is also produced through buoyancy by microscopic temperature fluctuations. Indeed sedimenting droplets can evaporate, absorbing latent heat and thus locally cooling the environment. This effect can be important in some conditions, as proved in [20, 21, 19] for the cloud-clear air mixing at small turbulent kinetic energy rates. However, provided that we focus on the inner adiabatic core, away from the cloud boundaries, on first approximation we neglect this microscopic source of anisotropic fluctuations. With equation (1), we are thus focusing on the turbulent motion of in-cloud air, neglecting the role of convective motions. Note that previous two-dimensional DNS [27, 28] suggest that the qualitative effects of turbulence on condensation do not depend on the specific statistical details of the turbulent regime analysed.

Water vapor molecules carried by the turbulent velocity field are the source for droplet growth by condensation. The relevant quantity for droplet condensation/evaporation is the supersaturation, which quantifies the presence of vapor available for cloud particles growth. It is defined as $s := e/e_s - 1$, where e and e_s are the vapor pressure and the saturation vapor pressure respectively. Droplets are able to grow when the surrounding vapor content exceeds the saturation point ($s > 0$ in equation (4), moist air). On the contrary droplets tend to evaporate when s is negative (dry regions). Exhaustive *in situ* measures of the small-scales statistics of the vapor field are not available at now. Therefore, different models proposed cannot yet be directly validated by comparison with real data.

For the sake of generality and simplicity, we adopt here the simplest generalization of the well known Twomey's model [34]. While Twomey considered a one-dimensional equation for the time-dependent supersaturation function, here we consider the turbulent vapor to fluctuate both in space and time. For this reason we introduce the supersaturation as a field $s(\mathbf{x}, t) := \frac{e}{e_s}(\mathbf{x}, t) - 1$, that quantifies the amount of vapor which is present in point $\mathbf{x}$ at time t. Since $s(\mathbf{x}, t)$ is allowed to fluctuate from positive to negative values, dry and moist regions can coexist at the same time.

The generalization of Twomey's equation [34, 1, 14, 31] for the supersaturation field is an advection-diffusion equation:

$$\partial_t s + \mathbf{v} \cdot \boldsymbol{\nabla} s \;=\; \kappa \Delta s + A_1 w - \frac{s}{\tau_s}\,. \tag{2}$$

Here we assume that the scalar field $s(\mathbf{x}, t)$ is passively advected by the turbulent flow $\mathbf{v}(\mathbf{x}, t)$ which is not affected by its presence. Here, we are neglecting the compositional effects of vapor on the buoyancy forces acting on the flow that are generally thought to be small [4]. In the last equation, $\kappa \approx 10^{-5} m^2 s^{-1}$ is the molecular diffusivity of water vapor in air and $w(\mathbf{x}, t)$ is the vertical component of the turbulent velocity field $\mathbf{v}$. The term $A_1 w$ acts as a source/sink term of supersaturation resulting from the variation in temperature and pressure due to vertical motion. A_1 can be interpreted as a global supersaturation

gradient. The term $-s/\tau_s$ accounts for the double effect of condensation/evaporation on supersaturation: on one side the phase change directly modifies the water vapor content, on the other side it locally modifies temperature due to absorption or release of latent heat. In dry regions, $s(\mathbf{x},t) < 0$, droplets tend to evaporate releasing vapor and cooling the environment. Here, the term $-s/\tau_s$ is a source of supersaturation. Conversely in moist regions, droplets tend to absorb vapor for condensation and to release latent heat, here $-s/\tau_s$ acts as a sink term. The parameter τ_s is the relaxation timescale of the supersaturation and depends locally on the concentration and size of droplets. In each volume V, τ_s is defined as (see appendix A):

$$\tau_s^{-1} = \frac{4\pi\rho_w A_2 A_3}{V} \sum_{i=1}^{n} R_i \,, \tag{3}$$

where R_i are the radii of the n droplets inside the considered volume; A_2 is a function of thermodynamic parameters (see appendix A); ρ_w is the water density; A_3 is the rate of droplet radius growth by condensation (see equation (4)). In the numerical procedure, we consider each droplet to affect the value of τ_s in the eight nodes of the grid cell surrounding its position. The weight of the contribution to each node is calculated via a three-linear interpolation. Table 1 shows the reference values of these parameters used in the numerical experiments.
Note that Twomey's one-dimensional equation for s is derived under a given temperature profile neglecting fluctuations. It is difficult to quantify temperature fluctuations in clouds, since *in situ* microscale cloud data are unavailable. For what concerns the vapor field, this amounts to neglect an additional source of fluctuations induced by temperature advection and diffusion. The remarkable feature of the simple model identified by equations (1) and (2), is that despite its simplicity it allows to identify nontrivial mechanisms leading to the spreading of the size spectra.

Given the evolution equation for the Eulerian turbulent fields, we can now introduce the Lagrangian dynamics of cloud particles and the time evolution of their radii. A complete description of the relation between the water vapor and the size of a droplet would imply an integral equation for the local dynamics occurring at the droplet surface. Nevertheless, since the typical timescales of microscopic dynamics are much smaller than that of condensation, we consider the droplet to be instantaneously in equilibrium with the surrounding vapor (a detailed quantification of this assumption is given, e.g., in refs. [29, 31, 14]). Under basic assumptions[1], we end up with the following equation for the i-th droplet growth rate (see also [1] for further details),

$$\frac{dR_i(t)}{dt} = A_3 \frac{s(\mathbf{X}_i(t),t)}{R_i(t)} \,, \tag{4}$$

where A_3 is a function of the local conditions and is here assumed to be constant throughout the entire volume (variations of this parameter with temperature in typical warm cloud conditions are smaller than 3%). According to equation (4), the growth rate varies from

[1]We assume that (i) droplets are almost spherical (significant deformations from the spherical shape are typical of much larger drops, from sizes of hundreds of μm on CHECK!!); (ii) the coefficient A_3 is not significantly altered by either the chemical composition of droplets or the size of the droplet itself (this holds for droplets already activated onto condensation nuclei); (iii) curvature and salinity corrections are negligible (this holds for radii larger than about $1\,\mu m$)

$A1$ (m^{-1})	A_2 $(kg^{-1}m^3)$	$A3$ $(\mu\, m^2 s^{-1})$	N_{drops}/V (cm^{-3})	τ_s (s)	R $(\mu\, m)$	St
5×10^{-4}	350	25.0	130	5.0	5	5×10^{-3}

Table 1: Reference values for some of the physical parameters used in the numerical experiments. The values of the vapor relaxation time τ_s, the droplet radius R and the Stokes number St correspond to the initial conditions.

a droplet to another, since it depends on the supersaturation fluctuation $s(\mathbf{X}_i(t), t)$ measured along the trajectory $\mathbf{X}_i(t)$ of the single droplet. Due to turbulent dispersion initially close droplets will eventually experience disparate values of supersaturation. This is the striking difference with respect to Twomey's model where all the droplets were exposed to the same supersaturation value.
Cloud droplets can be described as independent, passive, Stokes particles, whose trajectories $\mathbf{X}_i(t)$ and velocities $\mathbf{V}_i(t)$ evolve according to:

$$\frac{d\mathbf{X}_i(t)}{dt} = \mathbf{V}_i(t) \tag{5}$$

$$\frac{d\mathbf{V}_i(t)}{dt} = -\frac{\mathbf{V}_i(t) - \mathbf{v}(\mathbf{X}_i(t), t)}{\tau_d^i} + g\hat{\mathbf{z}}. \tag{6}$$

Here $\mathbf{v}(\mathbf{X}_i(t), t)$ is the fluid velocity at the particle position; $\tau_d^i(t) = \frac{R_i^2(t)}{3\nu\beta}$ is the particle response time (or Stokes time); $\beta = 3\rho_a/(\rho_a + 2\rho_w) \approx 3\rho_a/(2\rho_w)$ is the air/water density ratio; and g is the gravity acceleration. Equations (5) and (6), derived from Maxey and Riley [36], are valid for dilute suspensions of small spherical heavy particles. During the condensation stage, this working hypothesis are well verified as discussed in [33].

3 Framework of numerical simulations and range of parameters

This section is devoted to introduce the physical approach employed in the numerical simulations. As discussed earlier, DNS of cloud physics present a major problem: there is a huge number of degrees of freedom that cannot be fully described simultaneously. Turbulence is organized in spatial structures of typical scales ranging from hundreds of meters down to the Kolmogorov scale (typically $1\, mm$). Similarly, the timescales range from thousands to fractions of a second. Within this highly turbulent medium, a population of $10^{15} \div 10^{18}$ droplets evolve. Moreover, even if droplets are much smaller than any turbulent spatial scale, their trajectory span the whole range of turbulent scales. This results in correlations with the fluctuations of the vapor field [27, 28] and with the structures of the velocity field [37]. Therefore, turbulent motion at any scale play a significant role in droplet dynamics. However when dealing with experiments *in silico*, because of computational limitations, it is compulsory to choose a setting which describes only a

label	N	L (cm)	T_L (s)	Re_λ	ϵ $(m^2 s^{-3})$	η (cm)	τ_η (s)	$\sigma_s(t=0)$ (%)	v_{rms} (ms^{-1})	N_{drops} $(\times 10^5)$
(a)	64^3	9	2.0	40	10^{-3}	0.1	0.1	1.5×10^{-3}	4×10^{-2}	0.93
(b)	128^3	18	3.5	65	$9. \times 10^{-4}$	0.1	0.1	3.4×10^{-3}	$5. \times 10^{-2}$	8.2
(c)	256^3	38	5.5	105	10^{-3}	0.1	0.1	6.1×10^{-3}	$7. \times 10^{-2}$	71
(d)	512^3	70	7.6	185	1.1×10^{-3}	0.1	0.1	1.2×10^{-2}	$1. \times 10^{-1}$	320

Table 2: Parameter of the DNS. From left to right: number of gridpoints N, integral scale L, large-eddy turnover time T_L, microscale Reynolds number Re_λ, average energy dissipation rate ϵ, Kolmogorov spatial scale η, Kolmogorov timescale τ_η, initial supersaturation standard deviation $\sigma_s(t=0)$, velocity standard deviation v_{rms} and number of droplets N_{drops}.

portion of the system. By this choice, the analysis forcely loses part of the degrees of freedom, no matter how much complete and detailed the model is.

Recent results [27, 28], by means of direct numerical simulations in two dimensions, pointed out the importance of the large-scale fluctuations of the vapor field. These provide a strongly variable environment which is finally able to make the history of each droplet different thus broadening the size spectra. Of course in such context, the small scales of turbulence cannot be resolved and the analysis is limited to a statistically representative subset of the whole population. In [30], the complementary setting is adopted: by concentrating on a small rising parcel, authors can consistently describe in full details the droplet evolution. This approach, which focuses on what would happen in a cloud of very small dimensions, provides small fluctuations that eventually produce a limited degree of spreading.

Here we wish to put toghether the two complementary approaches. The goal is to obtain an estimate of the spreading of the droplet size spectrum due to condensation in a cloud core of size around $L = 100m$. As a first step, we perform a series of direct numerical simulations at increasing resolution. The grid spacing δx of each simulation corresponds to $1\,mm$. At each increase in resolution we are allowed to resolve larger integral scales L, corresponding to the size of the cloud. We consider four numerical experiments, labeled as run (a), (b), (c) and (d), with 64^3, 128^3, 256^3 and 512^3 grid points respectively. The integral scale of the system varies from $L \sim 9cm$ up to $L \sim 60cm$. The microscale Reynolds numbers $Re_\lambda \approx \sqrt{Re}$ [5] range from $Re_\lambda \sim 44$ to $Re_\lambda \sim 185$. The ratio between the air kinematic viscosity and the vapor molecular diffusivity is $\nu/\kappa = 1$, so that the flow and the scalar dissipative scales are of the same order. Table 2 lists all the relevant DNS parameters.

Clearly the process of doubling the resolution, if iterated, would ideally lead to the description of the whole range of scales from $\eta \approx 1mm$ to $L \approx 100m$. As we can only perform the first iterations of this process, we will recover the result for the target system as an extrapolation of the process to $L = 100m$ (Re_λ about few thousands). For each DNS, equations (1) and (2) are integrated, by means of a fully parallelised MPI code, using standard pseudospectral methods with dealiasing, in a computational domain peri-

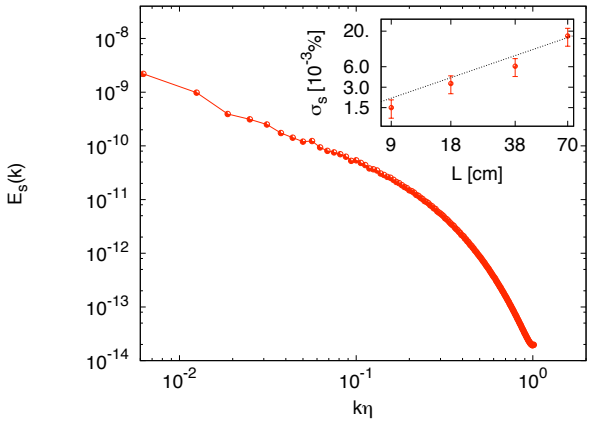

Figure 1: Log-log plot of the stationary supersaturation spectrum for the run (d) at $Re_\lambda \sim 200$. It shows a well defined $k^{-5/3}$ power law behavior, as expected from Kolmogorov-Obukhov-Corssin theory. The turbulent velocity field also shows a Kolmogorov spectrum (not shown). Inset: log-log plot of the standard deviation of the supersaturation field σ_s, measured in the stationary state, versus the size of the system L. The behavior is in agreement with the dimensional prediction $\sigma_s \sim A_1 L$.

odic in the three directions. Molecular viscosity (and diffusivity) is chosen so as to match the Kolmogorov lengthscale with the grid spacing $\eta \simeq \delta x$: this choice ensures a good resolution of the small-scale dynamics. Kinetic energy is injected at an average rate ϵ, by keeping constant the total energy in each of the first two wavenumber shells [38]. The scalar field is forced by the assigned gradient A_1; the term $-s/\tau_s$ is off as long as droplets are not injected into the flow. Time stepping is done using a 2^{nd} order Adam-Bashfort scheme. The time step is chosen to accurately resolve the smallest turbulent fluctuations, and the particle acceleration.

Starting from a zero field initial condition, the system reaches, after few large-scale eddy turn over times $T_L = L/v_{rms}$, a statistically stationary state. Figure 1 shows the supersaturation spectrum at the stationary state for run (d) before particles injection. In agreement with classical Kolmogorov-Obukhov-Corrsin theory (see e.g. [40]), this exhibits a $k^{-5/3}$ power law behavior in the Fourier space. Since the scalar spectrum is peaked on the large scales, as the integral scale increases, we approach larger and larger fluctuations. In the inset of Fig. 1, we show that the supersaturation standard deviation σ_s increases with the size of the system. The behavior is compared with the expectation $\sigma_s \sim A_1 L$, based on a dimensional balance of terms in equation (2). From the physical viewpoint, the increase of the cloud size corresponds to a stronger adiabatic cooling. This directly provides larger fluctuations in the vapor field, since the adiabatic cooling drives s through the source term $A_1 w$ in equation (2). The extrapolation of the vapor field standard deviation to $L \approx 100\ m$ gives $\sigma_s(L = 100m) \sim (2.0 \pm 0.6)\%$, a reasonable value for warm clouds.

Once the steady state has been attained, a monodispersed (with initial radius $R_i = 5\,\mu m$) population of droplets is injected into the flow. Initially, these are distributed homoge-

neously in space and with velocities equal to the local fluid velocity. Equations (5) and (6) are then advanced in parallel, by a standard second order Runge-Kutta method. We chose absorbing boundary conditions for droplet radius, i.e. a droplet whose size vanishes is abandoned, and no new particles are considered to enter the volume. Lagrangian velocities are computed via linear interpolation in the three spatial directions [39], which was demonstrated adequate to obtain well resolved particle accelerations. Similarly, we compute the vapor field $s(\mathbf{X}(t))$ at the particle position. Droplet concentration is for all experiments $\approx 130\, cm^{-3}$, which means that, on average, about one out of eight cells contains a droplet. In the largest simulation we followed the time evolution of 32 millions droplets. Coupling between droplets and the vapor field takes place via the term $-s/\tau_s$ of eq. (2), so that the initial vapor available is consumed for condensation onto droplet surface. From now on the symbol σ_s stands for the standard deviation of the supersaturation in the stationary state, which is the initial condition for our Lagrangian analysis. The complete system -flow, scalar and droplets- has been studied, at the largest resolution, for about two large-scale eddy turn over times. Longer time integrations were performed at lower resolutions.

4 Results and Discussion

Our simulations start with a spatially uniform distribution of monodispersed droplets with vanishing acceleration (velocity equal to that of the fluid). As cloud particles are released, they explore the volume space and experience the range of vapor fluctuations available in the system. The fluctuations of the vapor field decrease due to the feedback of droplets. After $2-3$ large scale eddy turn over times it generally stabilizes to a lower value of scalar energy. Our main focus is on the evolution of droplet size distributions. In Figure 2, the droplet size distributions are shown for runs (a)-(d) after one large scale eddy turn over time. A small degree of spreading is present for each simulation, and increases with the size of the cloud. This increase is due to the fact that larger domain sizes correspond to larger supersaturation fluctuations and longer large-eddy-turnover times. In other words, travelling in a larger cloud volume, droplets are exposed to more and more intense fluctuations of vapor for longer and longer times. In the inset of Fig. 2 we show the time evolution of the size distribution standard deviation σ_R. For $t \leq T_L$, this behaves linearly meaning that at short time lags, droplets grow with the vapor fluctuation initially experienced and do not feel the underlying local variations. A similar linear growth is observed for the standard deviation of the droplets square radius as well $\sigma_{R^2}(t) = (\langle R^4(t)\rangle - \langle R^2(t)\rangle^2)^{1/2}$ (not shown). This is because the droplet size distribution is close to Gaussian, and the mean radius is much larger than the standard deviation hence $\sigma^2_{R^2} \approx 2\sigma^4_R + 4\sigma^2_R\langle R\rangle^2 \approx 4\sigma^2_R\langle R\rangle^2$.
At larger times, when vapor is appreciably absorbed for condensation droplets growth slows down. From these results we try now to estimate the droplet size spreading achieved when the integral scale approaches a realistic value. To this purpose we evaluate the standard deviation σ_{R^2} of the distribution of the square radius at time T_L for each run. Note that experimental measures of the square radius can be found in [17]. In Fig. 3, the standard deviation $\sigma_{R^2}(T_L)$ is plotted as a function of the Reynolds number Re_λ characterizing flows (a),(b),(c) and (d). The simplest expectation, based on self-similarity of the growth process under different turbulent regimes, is that the final degree of spreading will

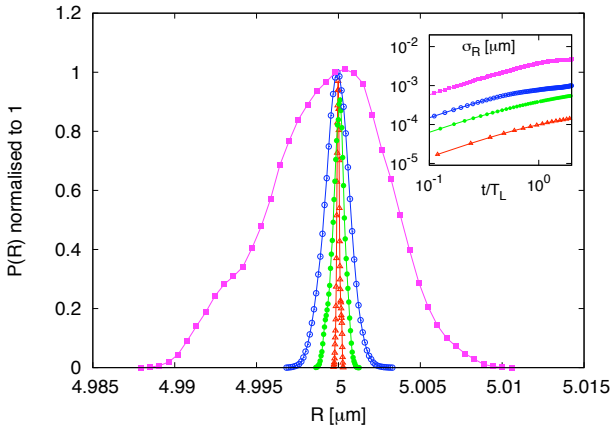

Figure 2: Droplet size distribution after one large-scale eddy turn over time, $t = T_L$, for the 4 DNS (a) (blue triangles), (b) (red dots), (c) (green circles) and (d) (black squares). In each run, droplets' initial distribution is $\delta(R - R_0)$, with $R_0 = 5\mu m$ (not shown). Each simulation presents a small degree of spreading, which increases with the Reynolds number. Inset: log-log plot of the time evolution of the standard deviation of the size distribution for the run (a)-(d). Color coding is the same of the main frame.

depend on the Reynolds number as a power law. A dimensional analysis of equation (4) leads to $\sigma_{R^2}(T_L) \sim A_3 \sigma_s T_L \sim Re_\lambda^\xi$. Remembering that in a turbulent flow $\sigma_s \sim Re_\lambda^{3/2}$ and $T_L \sim Re_\lambda$, we easily end up with $\xi = 5/2$. The dimensional scaling is shown in figure 3 for comparison. Of course this is a very simple estimate based on pure dimensional balance. Corrections are expected due to mechanisms excluded by the analysis. For instance, the supersaturation values undergo an initial transient due to vapor absorption on droplet surface. Additionally, according to [27], droplet trajectories correlate with vapor fluctuations.

The dimensional scaling with the Reynolds number of the flow can be extrapolated to draw the expectation for a real cloud. For a cloud of parameters $L = 100m$ and $Re_\lambda \approx 2500$, we obtain a square radius standard deviation $\sigma_{R^2}^{ext} \simeq (25. \pm 3.)\mu m^2$.

To further investigate the validity of these basic arguments and the role of turbulent large-scale fluctuations, we performed another numerical experiment, labeled run (e), resolving the large scales of the problem. The parameters in run (e) are $L \approx 100\,m$, $\eta \approx 30cm$, $v_{rms} \approx 0.6ms^{-1}$, $\sigma_s \approx 2\%$, $N_{drops} = 7. \times 10^6$, $T_L \approx 150\,s$ and numerical resolution $N^3 = 256^3$ grid points. Note that the level of vapor fluctuations are now appreciable and reasonable for typical warm cloud conditions. Space-time integration of the system has the same features described in Section 3. Note that with these parameters, we can not follow the evolution of $150\,cm^{-3}$ droplets, since their number would be too large. We put an amount of droplets that assures the significance of the statistics and account for the correct renormalization factor in the computation of the relaxation time τ_s in equation (2).

The phenomenology obtained is qualitatively similar to that described in [27]: there are

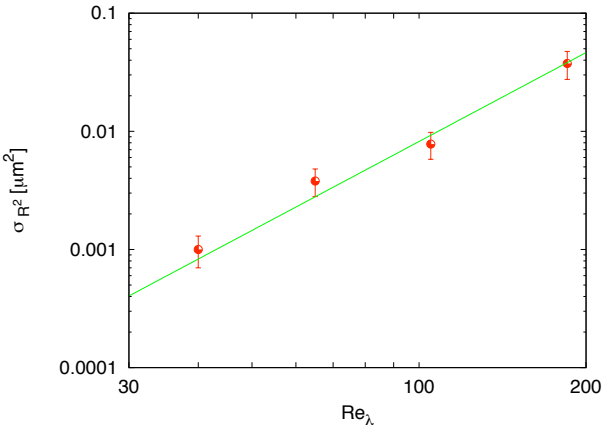

Figure 3: Log-log plot of the spreading of droplet size distribution $\sigma_{R^2}(T_L)$ for the square radius R^2, measured after one large-scale eddy turn over time T_L, as a function of the microscale Reynolds number $\Re_{lambda}$. The spreading is larger as the Reynolds number increases, since droplets evolve in conditions which are more and more differentiated. The dimensional prediction $\sigma_{R^2} \sim Re_\lambda^\xi$ with $\xi = 5/2$ is shown for comparison (see the text). The extrapolation of this law to the target cloud of parameters $L = 100m$, $\sigma_s \sim 2\%$ and $Re_\lambda \sim 2500$, gives a size spreading $\sigma_{R^2}^{ext} \sim 25\mu\, m^2$.

correlations between droplets and vapor due to the long-ranged correlations of the underlying turbulent velocity field. Droplets experience for a long time the same supersaturation fluctuation. If the supersaturation fluctuations are large enough, correlations become visible. Indeed they last longer than the time needed for droplets to completely evaporate so that droplets dwelling in dry regions disappear leaving these regions void of droplets (see figure 4). Conversely, droplets belonging to moist regions grow at different rates, according to the value of supersaturation they are correlated to. This provides a remarkable spreading of the size distribution, as shown in figure 5. The spreading of the size distribution can be quantified in terms of the standard deviation of the radius and of the square radius. After one large-scale eddy turn over time we obtain $\sigma_R(T_L) \simeq (1.7 \pm 0.5)\mu m$ and $\sigma_{R^2}(T_L) \simeq (18. \pm 5.)\mu m^2$, respectively. Note that of course simulation (e) does not resolve the whole range of spatial scales of realistic turbulence. However, by matching the parameter on the large scales of the problem, it reproduces the intensity of large scales fluctuations. The final spreading achieved is comparable to the expectation based on the extrapolation process described above. This points to the fact that the substantial contribution to droplet size spreading is given by the strong fluctuations of the vapor field, typical of the largest turbulent eddies. Hence the role of primary importance of the large scales.

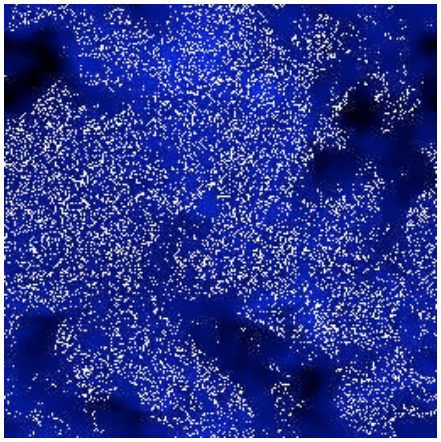

Figure 4: An instantaneous snapshot of spatial distribution of droplets (white points) and supersaturation field (light blue: supersaturated vapor $s > 0$, dark blue: undersaturated vapor $s < 0$) obtained by DNS (e) with $\sigma_s \approx 2\%$. Droplets are taken on a slice $L \times L \times 2\eta$ of the whole volume. Due to correlations, droplets are selectively concentrated in the moist portions of the cloud.

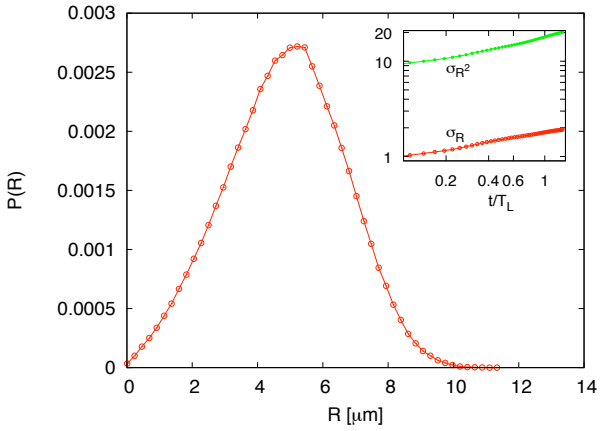

Figure 5: Droplet size distribution measured after one large scale eddy turn over time $T_L \sim 150s$ for the run (e), matching the large scale cloud parameters. In the inset, time evolution of the standard deviation of the radius distribution, $\sigma_R(t)$, and of the square radius distribution, $\sigma_{R^2}(t)$. At time $t = T_L$, we measure $\sigma_R(T_L) \simeq (1.7 \pm 0.5)\mu m$ and $\sigma_{R^2}(T_L) \simeq (18. \pm 5.)\mu m^2$.

5 Conclusion and Perspectives

In conclusion, turbulent fluctuations seem to play a relevant role for the broadening of the droplet size distribution in an idealized setting for condensation in warm cloud adiabatic cores. Our numerical simulations, up to a Reynolds number $Re_\lambda \sim 200$ and with millions of droplets, show that the size spectrum broadening increases as a power law of the Reynolds number. The observed behavior is consistent with the dimensional expectation. The extrapolation of the dimensional power law to large Reynolds numbers suggests a final broadening of the square size distribution of about $(25. \pm 3.)\,\mu m^2$ for a cloud core of size $L \approx 100\,m$ and $Re_\lambda \approx 2500$. This value is consistent with a further numerical experiment matching the large scales of the problem and resulting in a final spreading of $(18. \pm 5.)\,\mu m^2$. Although turbulence is active at any scale from η to L, this result hints to a crucial role of large scales. Therefore an LES analysis, parameterizing the effects of small scales on large scales, could capture the crucial features of the problem. Some aspects of the particle-turbulence interactions in atmospherical clouds were not discussed in this work. Buoyancy forces and the explicit dependence of the vapor field on the local temperature fluctuations were not accounted for. As well as the microscopic interactions of droplets on the turbulent flow. These ingredients may be relevant for a correct quantitative evaluation of droplet size evolution. Further research is needed in order to enlighten possible corrections to the presented results, coming from a complete account of the neglected aspects.

We acknowledge discussions with Antonio Celani and Andrea Mazzino, who have inspired and motivated this work. AS was partially supported by L'Oréal Italia - Unesco For Women in Science Fellowship, and by HPC-Europa Transnational Acces Program. AL acknowledges INFN, and CNR grant "Short-Term Mobility". Numerical simulations were performed at the supercomputing centre CINECA (Italy).

A Water-vapor interaction

The expression of the absorption time τ_s can be computed directly from the classical form of Twomey's model by identifying the terms:

$$\frac{s}{\tau_s} = A_2 \frac{d\rho_L}{dt} \qquad A_2 = \frac{R_a T}{\varepsilon e_s} + \frac{\varepsilon L^2}{p T c_{pa}} \tag{7}$$

where $\rho_L = m_w/V$ is the density of condensed water inside volume V, m_w being the mass of liquid water inside the volume; ε is the ratio between the molecular weight of water and dry air; L is the latent heat of water evaporation; R_a is the specific gas constant for dry air; T is the absolute temperature and c_{pa} is the specific heat of dry air at constant pressure p (see [1]). The evaluation of the constant A_2 in typical warm cloud conditions gives the reference value shown in table 1 and its variation with temperature is less then 1%, so that we assume it constant.
If we neglect entrainment (we focus on inner cloud cores), droplets inside the volume V

are the only responsible for the local change in vapor content:

$$\frac{d\rho_L}{dt} = \frac{1}{V}\frac{dm_w}{dt} = \frac{1}{V}\sum_{i=1}^{n} 4\pi\rho_w R_i^2 \frac{dR_i}{dt} = \frac{4\pi\rho_w A_3}{V}\sum_{i=1}^{n} R_i\, s \tag{8}$$

where R_i are the radii of the n droplets inside the volume V. The rate of variation of the radius is given by equation (4), where s is considered equal for each droplet inside the small volume V. This is because, in the numerical analysis, V is a cube of wedge η, similar to the vapor diffusive scale. The fluctuations of the scalar field are tiny under this scale, and all the droplets inside the volume V experience approximately the same value of s. In this sense, the Twomey's parcel, where no spatial fluctuations of the supersaturation field are accounted for, corresponds to our grid cell.
From equations (7) and (8) we end up with the expression (3) for the absorption time τ_s.

References

[1] H. R. Pruppacher and J. D. Klett, *Microphysics of Clouds and Precipitation*, Kluwer Academic Publishers, Boston, MA (1997).

[2] I. Y. Lee and H. R. Pruppacher, "A comparative study on the growth of cloud drops by condensation using an air parcel model with and without entrainment" *Pure and Appl. Geophys.* **115** 523-545 (1977)

[3] P. Squires, "The growth of cloud drops by condensation" *Aust. J. Sci. Res.* **5** 59-86 (1952)

[4] B. Stevens, "Atmospheric moist convection" *Annu. Rev. Earth Planet. Sci.* **33** 605-643 (2005)

[5] U. Frisch, *Turbulence*, Cambridge University Press, Cambridge, UK (1995).

[6] *Climate Change 2001: the scientific basis. Contribution of working group I to the third assessment report of the intergovernmental panel on climate change*, Cambridge University Press, Cambridge UK and New York, NY, USA (2001).

[7] T. B. Martonen (Editor), *Medical Applications of Computer Modelling: Cardiovascular and Ocular System*, WIT PRESS, UK (2000).

[8] F. Zhao, M. C. Lai and D. L. Harrington, "Automotive spark-ignited direct-injection gasoline engines", Prog. in Ener. and Comb. Sci.**25**, 437-562 (1999).

[9] P. G. Saffman and J. S. Turner, "On the collision of drops in turbulent cloud", J. Fluid Mech. **1**, 16-30 (1956).

[10] G. Falkovich, A. Fouxon, and M. G. Stepanov, "Acceleration of rain initiation by cloud turbulence", Nature, **419**, 151-4 (2002).

[11] S. Ghosh, J. Davila, J. C. R.Hunt, A. Srdic, H. J. S. Ferrando and P. R. Jonas, "How turbulence enhances coalescence of settling particles with applications for rain in clouds", Proc. Roy. Soc. A **461**, 3059-3088 (2005).

[12] M. Wilkinson, B. Mehlig, V. Bezuglyy, "Caustic Activation of Rain Showers", Phys. Rev. Lett. **97** 048501 (2006).

[13] S. Sundaram and L. R. Collins, "Collision statistics in an isotropic particle-laden turbulent suspension. Part I. Direct numerical simulations", J. Fluid. Mech. **335**, 75-109 (1997).

[14] R. A. Shaw, "Particle-turbulence interactions in atmospheric clouds", Annu. Rev. Fluid Mech. **35**, 183-227 (2003).

[15] J. Warner, "The microstructure of cumulus clouds. Part I. general features of the droplet spectrum", J. Atmos. Sci. **26**, 1049-1059 (1969).

[16] A. Blyth, "Entrainment in cumulus clouds", J. Appl. Meteorol. **32**, 626-641 (1993).

[17] J. L. Brenguier and L. Chaumat, "Droplet spectra broadening in cumulus clouds. Part I. Broadening in adiabatic cores", J. Atmos. Sci. **58**, 628-641 (2001).

[18] R. A. Shaw, W. C. Reade, L. R. Collins and J. Verlinde, "Preferential concentration of cloud droplets by turbulence: Effects on the early evolution of cumulus cloud droplet spectra", J. Atmos. Sci. **55**, 1965-1976 (1998).

[19] M. Andrejczuk, W. W. Grabowski, S. P. Malinowski and P. K. Smolarkiewicz, "Numerical simulations of cloud-clear air interfacial mixing", J. Atmos. Sci. **61**, 1726-1739 (2004).

[20] P. Korczyk, P. Malinowski and T. A. Kowalewski, "Mixing of cloud and clear air in centimeter scales observed in laboratory by means of particle image velocimetry", Atmos. Res. **82**, 173-182 (2006)

[21] S. P. Malinowski, I. Zawadzki and P. Banat, "Laboratory observations of cloud clear air mixing in small scales", J. Atmos. Ocean. Technol. **15**, 1060 (1998).

[22] D. B. Johnson, "The Role of Giant and Ultragiant Aerosol Particles in Warm Rain Initiation", J. Atmos. Sci. **39**, 448-460 (1982).

[23] A. V. Korolev, "The influence of supersaturation fluctuations on droplet size spectra formation", J. Atm. Sci. **52**, 3620-3634 (1995).

[24] I. P. Mazin, *The Stochastic Condensation and its Effects on the formation of cloud droplet size distribution*, Proc. Int. Conf. on Cloud Physics, Toronto, ON, Canada (1968).

[25] J. T. Bartlett and P. R. Jonas, "On the dispersion of the size of droplets growing by condensation in turbulent clouds", Quart. J. Roy. Meteor. Soc. **98**, 150 (1972).

[26] L. M. Levin and Y. S. Sedunov, "Stochastic condensation of drops and kinetics of cloud spectrum formation", J. Rech. Atmos. **2**, 425-432 (1966).

[27] A. Celani, G. Falkovich, A. Mazzino and A. Seminara, "Droplet Condensation in Turbulent Flows", Europhys. Lett. **70**(6) 775-782 (2005).

[28] A. Celani, A. Mazzino, A. Seminara and M. Tizzi, "Droplet condensation in convective turbulence", Journ. Turb. in press. (2007).

[29] P. A. Vaillancourt, M. K. Yau and W. W. Grabowski,"Microscopic approach to cloud droplet growth by condensation. Part I: Model description and results without turbulence", J. Atmos. Sci. **58** 1945-1964 (2001).

[30] P. A. Vaillancourt, M. K. Yau, P. Bartello and W. W. Grabowski, "Microscopic approach to cloud droplet growth by condensation. Part II: Turbulence, clustering and condensational growth", J. Atmos. Sci. **59**, 3421-3435 (2002).

[31] A. V. Korolev and I. P. Mazin, "Supersaturation of water vapor in clouds", J. Atmos. Sci. **60**, 2957-2974 (2003).

[32] A. V. Korolev and G. A. Isac, "Drop Growth Due to Hugh Supersaturation, Caused by Isobaric Mixing", Journ. Atmos. Sci. **57**, 1675-1685 (2000).

[33] P. A. Vaillancourt and M. K. Yau, "Review of particle-turbulence interactions and consequances for cloud physics", Bull. Am. Meteor. Soc. **81**(2), 285 (2000).

[34] S. Twomey, "The nuclei of natural cloud formation. Part II. The supersaturation in natural clouds and the variation of cloud droplet concentration", Geophys. Pure Appl. **43**, 243-249 (1959).

[35] L.-P. Wang, Y. Xue, O. Ayala, and W. W. Grabowski, "Effects of stochastic coalescence and air turbulence on the size distribution of cloud droplets", Atmospheric Research **82**, 416 (2006).

[36] M. R. Maxey and J. Riley, "Equation of motion of a small rigid sphere in a nonuniform flow", Phys. Fluids **26**, 883 (1983).

[37] J. Bec, L. Biferale, M. Cencini, A. Lanotte, S. Musacchio, and F. Toschi, "Time scales of particle clustering in turbulent flows", Phys. Rev. Lett. **98**, 084502 (2007).

[38] S. Chen, G. D. Doolen, R. H. Kraichnan, and Z. S. She, "On the statistical correlations between velocity increments and locally averaged dissipation in homogeneous turbulence", Phys. Fluids A **5**, 458-463 (1993).

[39] P. K. Yeung, and S. B. Pope, "An algorithm for tracking fluid particles in numerical simulations of homogeneous turbulence", J. Comput. Phys. **79**, 373 (1988).

[40] H. Tennekes, and J. L. Lumley, *A first course in turbulence*, MIT press, Cambridge, MA (1972).

[41] recupera ref dove dice che ci sono poche parcel che diventano soprasature per latent heat

Bibliography

[1] M. ANDREJCZUK, W. W. GRABOWSKI, S. P. MALINOWSKI and P. K. SMOLARKIEWICZ. Numerical simulationof cloud-clear air interfacial mixing. *Journ. Atmos. Sci.*, **61** 1726-1739, (2004).

[2] M. ANDREJCZUK, W. W. GRABOWSKI, S. P. MALINOWSKI and P. K. SMOLARKIEWICZ. Numerical simulationof cloud-clear air interfacial mixing: effects on cloud microphysics. *Journ. Atmos. Sci.*, **63** 3204-3225, (2006).

[3] I. BALASHAZY, W. HOFMANN and T. HEISTRACHER. Local particle deposition patterns may play a key role in the development of lung cancer. *J. Appl. Physiol.*, **94** 1719-1725, (2003).

[4] D. M. BRODAY and P. G. GEORGOPOULOS. Growth and deposition of hygroscopic particulate matter in the human lungs. *Aerosol Sci. Tec.*, **34** 144-159, (2001).

[5] M. E. CREWE. Meteorology and aerial navigation. *The Roy. Met. Soc.*, **4**, (2002).

[6] P. J. CRUTZEN. Albedo enhancement by stratospheric sulfur injections: a contribution to resolve a policy dilemma? *Clim. Change*, **77** 211-220, (2006).

[7] G. FALKOVICH, A. FOUXON and G. STEPANOV. Acceleration of rain initiation by cloud turbulence. *Nature*, **419** 151-154, (2002).

[8] G. FALKOVICH, M. G. STEPANOV and M. VUCELJA. Rain initiation time in turbulent warm clouds. *J. Appl. Met. and Climat*, **45** 591, (2006).

[9] U. FRISCH. *Turbulence. The legacy of A. N. Kolmogorov*. Cambridge University Press, Cambridge, (1995).

[10] S. GHOSH, J. DAVILA, J. C. R. HUNT, A. SRDIC, H. J. S. FERNANDO and P. R. JONAS. How turbulence enhances coalescence of settling particles with applications to rain in clouds. *Proc. Royal Soc.*, **461** 3059-3088, (2005).

[11] IPCC. *Climate Change 2001: the scientific basis. Contribution of working group I to the third assessment report of the intergovernmental panel on climate change*. Cambridge University Press, Cambridge UK and New York, NY USA, (2001).

[12] A. JACZEWSKI and S. P. MALINOWSKI. Spatial distribution of cloud droplets in a turbulent cloud chamber flow. *Quart. Journ. Roy. Met. Soc.*, **131** 2047-2062, (2005).

[13] D. B. JOHNSON. The role of giant and ultra giant aerosol particles in warm rain initiation. *J. Atmos. Sci.*, **39** 448-460, (1982).

[14] V. I. KHVOROSTYANOV and J. A. CURRY. A simple analytical model of aerosol properties with account for hygroscopic growth. *Jour. Geophys. Res.*, **104** 2163-2174, (1999).

[15] P. KORCZYK, S. P. MALINOWSKI and T. A. KOWALEWSKI. Mixing of cloud and clear air in centimeter scales observed in laboratory by means of particle image velocimetry. *Atmos. Res.*, **82** 173-182, (2006).

[16] K. LEHMANN, H. SIEBERT, M. WENDISCH and R. A. SHAW. Evidence for inertial droplet clustering in weakly turbulent clouds. *Tellus B*, **59 (1)** 57-65, (2007).

[17] T. B. MARTONEN. *Medical applications of computer modeling*. WIT Press, UK, (2001).

[18] H. R. PRUPPACHER and J. D. KLETT. *Microphysics of Clouds and Precipitation*. Kluwer Academic Publishers, Boston, (1997).

[19] A. L. ROTCH. The international meteorological conference at paris, september, 1896. *Mont. Weath. Rev.*, **24-10** 365-367, (1896).

[20] R. A. SHAW, W. C. READE, L. R. COLLINS and J. VERLINDE. Preferential concentration of cloud droplets by turbulence: effects in the early evolution of cumuluscloud droplet spectra. *Journ. Atmos. Sci.*, **55** 1965-1976, (1998).

[21] S. SUNDARAM and L. R. COLLINS. Collision statistics in an isotropic particle-laden turbulent suspension.part i: direct numerical simulations. *J. Fluid Mech.*, **335** 75-109, (1997).

[22] J. W. TELFORD. Clouds with turbulence; the role of entrainment. *Atmos. Res.*, **40** 261-282, (1996).

[23] S. TWOMEY. The nuclei of natural cloud formation part ii: the supersaturation in natural clouds and the variation of cloud droplet concentration. *Pure Appl. Geophys.*, **43** 243-249, (1959).

[24] P. A. VAILLANCOURT and M. K. YAU. Review on particle-turbulence interactions and consequences for cloud physics. *Bull. Amer. Met. Soc.*, **81** 285-298, (2000).

[25] P. A. VAILLANCOURT, M. K. YAU and W. W. GRABOWSKI. Microscopic approach to cloud droplet growth by condensation. part i: model description and results without turbulence. *Journ. Atmos. Sci.*, **58** 1945-1964, (2001).

[26] P. A. VAILLANCOURT, M. K. YAU, W. W. GRABOWSKI and P. BARTELLO. Microscopic approach to cloud droplet growth by condensation. part ii: turbulence, clustering and condensational growth. *Journ. Atmos. Sci.*, **59** 3421-3435, (2002).

[27] M. WILKINSON, B. MEHLIG and V. BEZUGLYY. Caustic activation of rain showers. *Phys. Rev. Lett.*, **97** 048501, (2006).

[28] Z. ZHANG, C. KLEINSTREUER and C. S. KIM. Water vapor transport and its effects on the deposition of hygroscopic droplets in a human upper airway model. *Aerosol Sci. Tec.*, **40** 1-16, (2006).

[29] Z. ZHANG, C. KLEINSTREUER, C. S. KIM and Y. S. CHENG. Vaporizing microdroplet inhalation, transport and deposition in a human upper airway model. *Aerosol Sci. Tec.*, **38** 36-49, (2004).

[30] F. ZHAO, M. C. LAI and D. L. HARRINGTON. Automotive spark-ignited direct-injection gasoline engines. *Prog. in Ener. and Comb. Sci.*, **25** 437-562, (1999).